Impact of drops upon surfaces with complex morphology

Matthew Andrew
Wadham College
University of Oxford

A thesis submitted for the degree of
Doctor of Philosophy

Trinity Term 2016
Supervised by Prof. Julia M. Yeomans FRS

Impact of drops upon surfaces with complex morphology

Matthew Andrew

Wadham College
University of Oxford

A thesis submitted for the degree of
Doctor of Philosophy

Trinity Term 2016
Supervised by Prof. Julia M. Yeomans FRS

Abstract

Drop impacts are ubiquitous in nature forming a vital pathway for the transport of liquids, primarily water, and any dissolved substances. The axisymmetric impact of drops has been heavily studied but less work has been done on droplet impacts in which axial symmetry is broken. To analyse such impacts we used a two phase lattice Boltzmann code capable of simulating high density differences.

We studied the impact of droplets on cylindrical surfaces, with radius of curvature similar to that of the drop. We found that the symmetry breaking nature of these surfaces leads to droplets bouncing faster and in elongated shapes. The origin of this effect is a positive feedback mechanism through which the momentum asymmetry resulting from the impact grows during retraction.

We next looked at how varying the size of the cylinder affected this phenomenon. We found that smaller cylinders increased the contact time reduction, as long as they were still bigger than the droplet, but that below this limit the drop contacted the flat surface and entered a new regime.

The work was expanded to look at other types of bouncing asymmetry, using a simple, exactly solvable Lagrangian model. We found that contact time reduction can result from an asymmetric droplet shape, an initially asymmetric velocity or if the surface has an asymmetric drag.

A study of the impact of liquid drops containing embedded air bubbles was also undertaken. This was found to lead to jet formation from the bottom of the bubble. We showed how the jet velocity depended on the physical parameters of the drop and impact. In particular the jet formation was very sensitive to the position of the air bubble inside the drop.

Publications Related to this Thesis

This thesis has used material from the following publications:

Chapter 3 uses material from Liu Y., Andrew M., Li J., Yeomans J. M. and Wang Z., Symmetry breaking in drop bouncing on curved surfaces. *Nature Communications*, **6**, 2015.

Chapter 5 uses material from Andrew M., Yeomans J. M. and Pushkin D., A model of axisymmetric and non-axisymmetric droplet bouncing. *Submitted to Soft Matter*

Acknowledgements

I would first and foremost like to thank my supervisor Julia Yeomans for the invaluable aid provided throughout my doctorate. From the initial discussions when I first arrived, to the feedback on the final thesis. I greatly appreciated all the time and experience that was put into helping me.

The work would also not have been possible without my collaborators. Most notably Yahua Liu and Zuankai Wang who provided brilliant experimental data, and Mitya Pushkin who's discussions and mathematical knowledge were invaluable.

Special thanks go to my office mates Arnold Mathijssen, Andrew Balin, Rachel Bennett, Anatolij Gelimson and Luuk Metselaar. Having people to bounce ideas off when things hit a brick wall was invaluable as was to an equal extent people to talk to about banalities during the day. Arnold in particular was there from day one until the end sharing a supervisor and invaluable, at least to me, discussions.

Amin Doostmohammadi and Tyler Shendruk provided valuable experience from people one step up the ladder and were always willing to help when asked. Whilst Alfonso Castrejon-Pita provided valuable experimental motivations, encouragement and discussion with hopefully more yet to come. I would also like to thank Michelle Bosher for making sure things ran smoothly in innumerable ways and being so friendly and welcoming.

Moving away from the scientific side of things I would like to thank my family who have always provided great support. My parents, Mike and Magda, for always being the rock I could rely on and a source of great comfort when it was needed and my siblings, Ben, Luke, Amelia, Tim and Dom, for enriching my life in numerous ways. The same can also be said of all the friends I made in Oxford over my time here with special mention going to the members of OURPGS who between them provided innumerable hours of fun and my flatmate Lucia who at three years and counting has managed to put up with living with me for longer than anyone before.

Contents

CHAPTER 1

Introduction

The impact of liquid droplets upon surfaces has been a problem of interest for many years since it was first observed in detail by Worthington(1). The impact of these drops is important in numerous applications for example anti-icing(2), inkjet printing(3), plant spraying(4), spray cooling(5) and water harvesting(6). All of these applications require an understanding of the different possible results of a droplet impact upon a surface, as well as how conditions can be controlled to promote some particular behaviour over others.

When a drop hits a solid surface the most common outcomes are that it can spread, splash or rebound(7). In this context spread means that the liquid spreads across the surface eventually forming an equilibrium shape and stays there until some other external factor dislodges it. Splash refers to the phenomena whereby the drop breaks up during impact into numerous smaller droplets and rebound refers to the case in which the drop bounces off the surface. These three cases are not of course discrete and two or all three are often seen.

The way in which a drop bounces depends on properties of both the impacting drop and the surface. For the drop the relevant parameters are its size, the impact velocity, the surface tension, the density and the viscosity. The properties of the surface which can have an effect meanwhile are the contact angle, contact angle hysteresis, surface roughness, temperature and most importantly for this work the

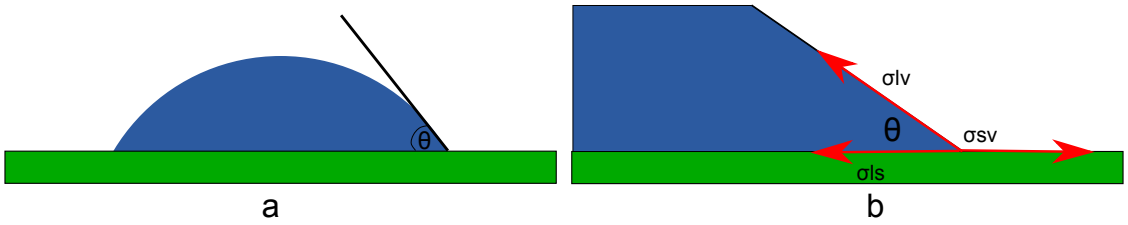

Figure 1.1: Diagrams demonstrating (a) the contact angle and (b) the forces at the three phase contact line.

large scale topology of the surface.

1.1 Contact angle

When placed upon a homogeneous flat substrate a liquid will either spread out into a film or adopt a hemispherical shape. The contact angle the liquid makes with the surface is used to characterise these states, for clarity this angle is shown in fig. 1.1a. Its value depends on the surface chemistry of the liquid and substrate in question. This phenomena was first noted by Young(8) and can be explained by looking at the surface tension forces at the three phase contact line where the liquid air interface contacts the surface. This interface point and the three forces are shown in fig. 1.1b. Assuming that the free interface is at an angle θ to the surface the force tangential to the surface when normalised to unit length is

$$F_{tan} = \sigma_{sl} - \sigma_{sv} + \sigma_{lv}\cos\theta = 0, \tag{1.1}$$

where σ_{sl} is the substrate liquid surface tension, σ_{sv} is the substrate air surface tension and σ_{lv} is the liquid air surface tension. At equilibrium this force is equal to zero leading to the Young's equation

$$\cos\theta = \frac{\sigma_{sv} - \sigma_{sl}}{\sigma_{lv}}. \tag{1.2}$$

The contact angle is a useful parameter to define different surfaces from a thermodynamic perspective. Surfaces which have a low contact angle with water, generally $\theta < 90°$, are called hydrophilic or wetting surfaces. The most extreme

case is a contact angle of zero degrees in which case the water will spread out into a thin film. Surfaces with a high contact angle, generally $\theta > 90°$, are known as hydrophobic surfaces. The highest contact angles which can be achieved on flat surfaces using chemical coatings is $\theta \approx 120°$(9; 10).

So far in this discussion the effect that gravity has on the shape the drop forms has been neglected. The extent to which this effect is important depends on the relative size of the surface tension energy and gravitational energy(11). The surface tension energy scales as σR^2, in which σ is the surface tension, as the total energy is proportional to the area of the interface times the surface tension. The gravitational energy meanwhile scales as $\rho g R^3 R$. Gravitational effects will therefore be negligible if $\sigma R^2 \gg \rho g R^4$. This can be rewritten as

$$R \ll \lambda_c = \sqrt{\frac{\sigma}{\rho g}}. \tag{1.3}$$

λ_c is known as the capillary length. For water λ_c is of the order of 3mm. For $R \ll \lambda_c$ liquids form a cap of constant curvature on the surface as described previously. For lengthscales greater than λ_c gravity begins to have an effect on the shape of the drop forming flatter free interfaces of non constant curvature.

1.1.1 Superhydrophobic surfaces

Very high contact angles, up to almost 180 degrees, can be achieved on surfaces with significant amounts of surface topology or roughness(12). These surfaces also tend to exhibit very low resistance to the movement of water across them(13; 14; 15; 16). Surfaces which exhibit very high contact angles and high water mobility are known as superhydrophobic surfaces. These sorts of surfaces are ubiquitous in nature the most famous example is the lotus leaf(17; 18; 19), but they also appear on numerous other plants and animals(20).

Roughness leads to superhydrophobicity because the roughness often traps an air layer in between the liquid and the bulk substrate(10). There are two different states which the drop can form with the surface, a suspended state called the Cassie-Baxter state(21) shown in fig. 1.2a and the Wenzel state(22) in which the

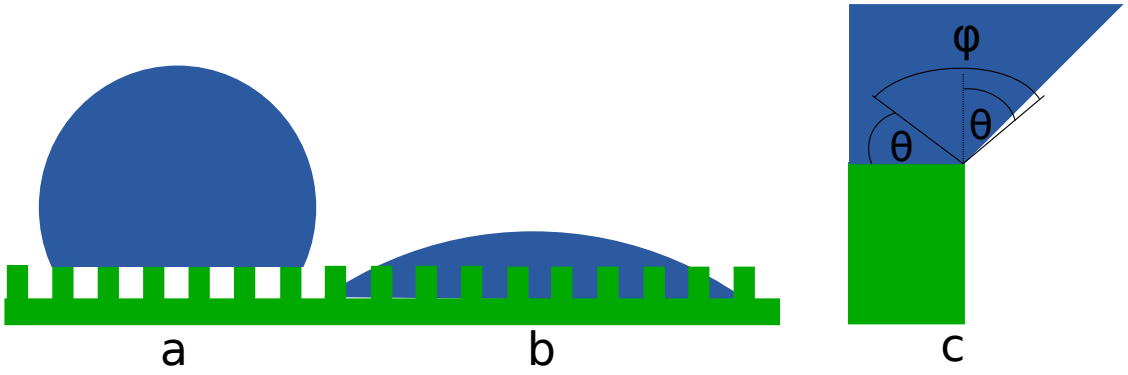

Figure 1.2: (a)-(b) Representations of the Cassie and the Wenzel state respectively. (c) A demonstration of pinning at a corner in which θ is the contact angle and φ is the angle through which the drop can deform before it penetrates the surface.

drop has penetrated the surface roughness as shown in fig. 1.2b. The Cassie state leads to a substantially increased contact angle compared to that seen on a flat surface of the same substrate.

In the collapsed Wenzel state the contact angle with the surface is modified slightly compared to a flat surface because the change in the contact area between the substrate and the liquid as the contact line moves is affected by the surface roughness. On the assumption that the drop is much larger than the surface roughness this effect can be captured by a roughness factor, r, the ratio between the true surface area of the rough surface and the projected one. This factor modifies both the forces associated with the substrate in eq. 1.1 leading to a relationship between the flat surface contact angle θ and the Wenzel contact angle

$$\cos\theta_w = r\cos\theta. \tag{1.4}$$

In the suspended Cassie-Baxter state a small change δx in the position of a unit length of the contact line leads to a change in the liquid substrate contact area of $fr_w\delta x$ in which f is the fraction of the substrate in contact with the liquid and r_w is the proportion of the substrate in contact with the liquid when compared to the same contact area of smooth surface. For a smooth flat topped topology such as that shown in fig. 1.2a $r_w = 1$. There is also an increase in the liquid-air contact area due to the air pockets beneath the drop. Combining all of these results gives a

contact angle

$$\cos\theta_{CB} = r_w f \cos\theta_\gamma - (1 - f). \tag{1.5}$$

This can lead to greatly increased contact angles on such surfaces when compared to flat substrates with similar surface chemistry.

Which of the two states, Cassie or Wenzel, is stable depends on the exact details of surface topography but circumstances can exist in which both are thermodynamically stable separated by a free energy barrier(23; 24; 25). Numerous ways have been found to transition such systems over this free energy barrier including drop impact(26; 27; 28), applied external forces(29), vibration(30; 31) or the shrinking during drop evaporation(32).

1.1.2 Contact angle hysteresis

One further complication which can affect the contact angle is contact angle hysteresis. On an ideal substrate a sliding drop will maintain a constant shape and contact angle as it moves along. However in real world applications the drop often deforms slightly before it starts moving(33; 34). The leading contact line only starts moving once a certain angle, which is greater than the equilibrium contact angle, is reached. This angle is known as the advancing contact angle. Similarly the trailing contact line at the back of the drop often has to reach an angle less than the equilibrium contact angle known as the receding contact angle. The contact angle hysteresis of a surface is the difference between these two angles.

This effect can be attributed to Gibbs' pinning on the surface roughness(35). Gibbs' pinning is the phenomena whereby convex roughness can pin the contact line not allowing it to move until the free surface is sufficiently deformed. An extreme case of this is demonstrated in fig. 1.2c; here advancing liquid is pinned on a corner and has reached an angle much greater than the equilibrium contact angle. This is because to move on down the vertical surface the free surface must first rotate to the stage where it forms an angle of θ, the equilibrium angle, with the vertical. This leads to a range of angles φ over which the interface can be stable. A similar

effect is also seen at the receding contact line.

In particularly severe cases Gibbs' pinning can lead to drops caught in states which are not their thermodynamic equilibrium and require some form of excitation in order to reach the global thermodynamic equilibrium of the free energy. Indeed the Cassie and Wenzel states can be viewed as states enabled by the Gibb's pinning on surface topography one of which is metastable and the other the global minimum.

1.2 Dimensionless numbers

In order to quantify which regime any given simulation or experiment is in it is useful to use dimensionless numbers which can be easily compared. The dimensionless numbers of most relevance here are the Weber number

$$We = \frac{\rho u^2 L}{\sigma}, \tag{1.6}$$

where ρ is the density, u is the velocity, L is the length scale of the problem and σ is the surface tension. The Weber number measures the relative importance of the inertial forces in the numerator against the surface tension forces in the denominator. The Ohnesorge number meanwhile,

$$Oh = \frac{\mu}{\sqrt{\rho\sigma L}} = \frac{\sqrt{We}}{Re}, \tag{1.7}$$

where μ is the dynamic viscosity measures the relative importance of the viscosity and the combined effects of inertia and surface tension. Another commonly used dimensionless number is the Reynolds number defined as

$$Re = \frac{\rho u L}{\mu}. \tag{1.8}$$

However as this can be written in terms of the Weber number and the Ohnesorge number it does not provide any new information and in general in this work the *We*

and Oh are used. The capillary number

$$Ca = \frac{\mu v}{\sigma}, \tag{1.9}$$

measures the relative importance of viscous forces and surface tension. If gravity is of importance in the problem the Bond number can be used:

$$Bo = \frac{\delta \rho g L^2}{\sigma} \tag{1.10}$$

where $\delta\rho$ is the density difference between the two phases in the system and g is the gravitational constant.

In order to match a simulation to an experiment there are in general eight parameters which must be matched. These are the surface tension, liquid viscosity, gas viscosity, drop volume, liquid density, gas density, gravitational constant and velocity. Of these three can be matched by picking appropriate mass, length and time scalings between the simulation and the experiment. The gas density and viscosity can be fixed by setting the ratio of the viscosities and densities appropriately. This leaves three degrees of freedom to be determined which necessitates the use of three dimensionless numbers. In this work the three numbers used are the Weber number, Ohnesorge number and Bond number. In cases in which gravity is neglected there is one less parameter and only We and Oh are considered.

1.3 Liquid impacts

1.3.1 Impact phases

It is helpful when discussing the dynamics of an impacting drop to split the impact into several distinct phases(36). The first of these, known as the kinematic or crush phase, occurs during the initial impact. This is then followed by a spreading phase, then a retraction or relaxation phase and finally an equilibrium or rebound phase.

The crush phase is characterised by the dominance of the inertial forces and the compressibility of the drop. When a drop first impacts a surface the portion

of its energy initially tied up in the kinetic energy perpendicular to the surface is redistributed. In the simplest case on a flat surface this leads to the formation of a spreading rim.

The reason for this behaviour is the normal reaction force exerted by the surface. Considering a liquid layer close to the surface there are two major forces at work, one is the normal force exerted by the surface and the other is a pressure force exerted by the rest of the liquid. These two opposing forces lead to a spike in the pressure which then forces the liquid in the layer outwards. The pressure spike makes the exact details of this region of the impact hard to study as the assumption of incompressibility which normally makes such problems much simpler is void.

Fortunately this compressible phase is short lived so many studies have made progress with analytical models of drop impact by considering just the conservation of momentum and energy during this phase(37). This then allows the state of the system at the end of the crush phase to be found, at which point the assumption of incompressibility is once again valid, allowing an analysis of the later stages of the collision to be undertaken without worrying about the exact details in the crush phase.

For the purposes of this work the most important aspect of the crush phase is just the simple understanding that during this very early phase of the collision the kinetic energy perpendicular to the surface is redistributed into kinetic energy tangential to the surface during a very short time.

After the initial crush phase of the impact the newly formed rim begins to spread across the surface. In this regime the drop can initially be considered as a spherical cap above a spreading rim. As the spreading continues, and as long the Weber number is high enough, the spherical cap gradually decreases in height and eventually the drop forms a rim-film system. At this stage of the expansion most of the drop's volume is in an outer rim with a thin central film in the middle of the drop. For normal impacts onto a flat surface at the end of this spreading phase the drop has no kinetic energy left and all of the free energy of the drop is tied up in the surface tension associated with the highly deformed surface.

During the relaxation phase the drop begins to relax away from this highly deformed state towards equilibrium. The force driving the retraction is the surface tension. If the drop has spread beyond its equilibrium shape, as is normally the case for high Weber number impacts, the outer edge begins to retract. If this retraction is violent enough it can lead to rebound and the drop lifting off the surface. Otherwise the drop will eventually reach its equilibrium shape upon the surface.

In the case of rebound, at the end of this retraction when the rim meets itself a pressure spike very similar to that seen during the initial collision is observed. The key difference is that there is no downwards force so the reaction force from the substrate drives the drop off the surface.

A simple but useful model of retraction is to treat the rim as a mass which is pulled inwards by a force exerted by the film(38). This was first proposed by Taylor(39) and Culick(40) This force is of the form

$$F = 2\pi r\sigma(1 - \cos\theta) = \frac{du}{dt}m + \frac{dm}{dt}u \tag{1.11}$$

where r is the radius of the film, m is the mass of the rim, u is the rim velocity and θ is the contact angle. This equation can be derived by considering the change in the film's area as the radius is changed. The area of the top and bottom surfaces of the film is $A = \pi r^2$. The rate of change of this area multiplied by the appropriate surface tension, σ for the top and $-\sigma\cos\theta$ for the bottom, then gives the force. This force is then assumed to act upon the rim as though it were just a simple mass. Experimentally the retraction time is close to constant(38) so the first term on the right hand side of eq. 1.11 is taken to be zero. The mass of the rim changes as it absorbs the film, assuming that it is moving inwards at a constant rate this change can be estimated as

$$\frac{dm}{dt} = 2\pi rhu\rho \tag{1.12}$$

where h is the height of the film. Combining this with eq. 1.11 leads to an estimate

of the retraction velocity of

$$u = \sqrt{\frac{(1 - \cos\theta)\sigma}{h\rho}}. \tag{1.13}$$

This simple equation shows that the retraction velocity is increased for high contact angles, low densities and thin central films. It is included here as a useful reference as an adapted line of reasoning is used extensively in chapter 3.

1.3.2 Contact time and inertial capillary time

One of the variables of key interest in cases of droplet rebound is the contact time, the time which a drop spends in contact with the surface during an impact. This is a key factor in all processes which rely on transfer between the drop and substrate. Of particular interest are the transfer of heat as a shortened contact time is hypothesised as being of use in anti-icing(41) and the transfer of biological contaminants(17; 42; 43) as researchers attempt to design surfaces to reduce the degree of biofouling.

It is most useful to express the contact time in terms of a timescale relevant to the problem. In the case of a droplet collision in which viscous effects are neglected there is only one possible time scale known as the inertial capillary time

$$\tau = \sqrt{\frac{\rho R^3}{\sigma}}. \tag{1.14}$$

This time scale is the natural time scale of the system if dissipation can be neglected. Richard *et al.*(44) found that for sufficiently large impact velocities the contact time on a flat surface did not depend on the impact velocity and was proportional to τ, thus implying that dissipation was not significant in the system. This was due to the way the potential energy in the drop scales as it is deformed. If the drop is deformed by a small amount δx the area scales as $(\delta x)^2$. Since the potential energy of the problem scales quadratically the system acts like a simple harmonic oscillator and hence has an oscillation time independent of the magnitude of the oscillations.

Assuming that the drop acts as a harmonic oscillator puts a theoretical lower

limit on the contact time of 2.2τ(45). Several non flat surfaces have been found which reduce the contact time below this limit, for example the ridges introduced by Richard et. al.(45) or the cylindrical surface used by Liu et. al.(46).

1.3.3 Changing the impact surface

So far we have mostly discussed the normal impact of drops onto flat dry surfaces. However numerous cases exist which do not fit into this narrow group.

One well known case is the impact of droplets onto the superhydrophobic surfaces discussed earlier in section 1.1.1. This situation has been extensively studied(47; 48; 49; 50; 51) and it has been found that these surfaces greatly promote droplet rebound, as their high contact angle leads to a greater retraction force and the low contact angle hysteresis means there is little resistance to contact line motion.

Recently there has also been significant work on the effect that macrotextures on the surface have upon the impact process. Bird *et al.*(45) looked at the result of putting ridges on the surface and found that an enhanced retraction along the ridge led to a significantly reduced contact time. Guathier *et al.*(52) took this work further and found that the reduction in contact time depended on how many sub-droplets were formed during the impact. These works have led to an interest in the bouncing of drops off surfaces which are not axially symmetric with respect to the drops direction. For example Liu et. al.(46) looked at the impact of drops onto cylindrical structures and Robson studied the effect of having an asymmetry in the micropillar array used to form a superhydrophobic surface(53).

Another interesting recent work is due to de Ruiter et. al.(54) who found that for an extremely smooth surface the air layer between the drop and the surface never ruptured. This leads to bouncing that is independent of surface wettability as the drop never truly contacts the surface.

1.4 Cavity jets

Liquid jets are a phenomena of great interest. The foremost reason for this is that they provide the most common way to form liquid droplets(55). Liquid jets break up into droplets due to the Rayleigh-Plateau(56) instability; small perturbations in the jet's radius grow until eventually a pinch off of point is reached and droplets formed. This phenomena is near universal, but the perturbation growth is damped by viscosity leading to highly viscous fluids such as honey being capable of forming long filaments without breakup(57).

Jets, which then form into droplets, are normally produced by forcing fluid through a nozzle. Another way to produce jets however is by creating a pressure wave which impinges upon a curved density interface. In this case as the, initially planar, pressure wave approaches the curved interface the requirement for the pressure to be constant at the interface causes the pressure isolines to deform. This leads to a greater pressure gradient at the lowest point on the air-water interface, the lowest point here is defined as the point on the interface which is closest to the solid surface. A jet then forms from this centre of curvature. This phenomena has been observed in the simple case of dropping a test tube of liquid onto a surface(58) but can also be used to create supersonic jets if laser excitation is used(59; 60). It is important to note here that the jet formation is almost entirely inertially driven. The only significant role that surface tension plays is in ensuring than the initial interface is curved. One advantage of producing jets from interfaces is that the jets created are smaller in size than the containing structure. This allows the creation of smaller droplets which allows for greater finesse in, for example, inkjet printing(61).

The formation of jets from cavities can also occur in more stationary cases. Jets can be formed from the bursting of a bubble at the interface without any form of external excitation(62; 63), or by the relaxation of the hollow created by an impact on a free surface(64). In these cases the jet is driven by the relaxation of the free surface from an initially highly deformed state.

1.5 Overview of thesis

We first, in chapter 2, describe the lattice Boltzmann code used in much of our work. This code is heavily based on the papers of Lee *et al.*(65; 66). Its main advantage over many other lattice Boltzmann methods is that it can simulate a two phase system in which the two phases have a high density ratio. As the density ratio of air and water is of the order of one thousand this property is vital to study situations in which inertia is important. This is the case for all but the smallest drops, and when considering droplet impacts.

In chapter 3 the collision of drops on superhydrophobic cylindrical surfaces is studied. The inherent asymmetry of this situation causes the drop to lift-off after a shortened contact time in an elongated tubular shape(46). This phenomena is explained as being due to an asymmetry which forms very early on during the impact, in the crush phase. This leads to one axis of the drop starting to retract before the second axis. As a result the asymmetry grows until the drop lifts off in an elongated shape.

In chapter 4 the work on the collision of drops onto a cylinder is expanded as the effect of changing the cylinder size is looked at more closely. We find that, as the size of the cylinder is decreased, the contact time decreases until the radii of the drop and the cylinder are similar. Further reductions in the size of the cylinder cause the contact time to increase again. This occurs when the drop impacts not only the cylinder but also the flat surface on which it rests. This geometry is similar to that considered by Bird et. al.(45), and we relate our results to their work.

In chapter 5 a simple analytical model of drop impact is developed. This model uses a Lagrangian approach and assumes the drop is in an ellipsoidal shape. The validity of the model is checked in the linear limit against the work of Rayleigh(56) and is found to agree quantitatively. It is also found to qualitatively agree with experiments outside the linear deformation limit. The model is then used to explain the effect of introducing three kinds of asymmetry into droplet bouncing, namely initial momentum asymmetry, shape asymmetry and drag asymmetry. The effects of

these on the contact time and the forces within the drop are studied and discussed.

In chapter 6 the impact of drops containing an air bubble is considered. Similarly to the cases discussed in sec. 1.4 this leads to a jet. This jet leaves the surface even when the bulk of the drop spreads, retracts and remains on the substrate. The effect on the jet's velocity of varying the bubble's position, size and shape is studied. We find that the most important factor in determining the behaviour of the jet is the position of the bubble relative to both the top and bottom interface of the drop.

Finally, in chapter 7, we summarise our research and suggest directions for future work.

CHAPTER 2

Model

2.1 Introduction

The lattice Boltzmann approach(67; 68) is a simulation method developed and used to study fluid flows at a mesoscopic length scale(69). Mesoscopic here refers to length scales between the continuum length scale, at which the Navier-Stokes equation operates, and particle length scales, at which particle dynamic simulations would be appropriate. Its advantages are that it can capture surface effects more easily than a continuum Navier-Stokes solver but is not as computationally intensive as particle dynamics simulations.

The lattice Boltzmann method works by solving a discretised version of the classical Boltzmann equation. The Boltzmann equation describes a system out of thermodynamic equilibrium by tracking the evolution of a particle density function in a six dimensional space made up of the particles' positions and momenta(70). When the particle density function is known the values of various macroscopic quantities of interest can be found by taking moments of its distribution.

The specific lattice Boltzmann model used is based on the method developed by Lee (65; 66) to study the impact of drops upon complex surfaces. The advantage of this method is that it can model the density difference between air and water, allowing impacts to be studied with much greater realism than previously.

2.2 The Model

2.2.1 Binary Fluid

The binary fluid model simulates a two-phase fluid by coupling two different lattice Boltzmann equations. One solves for the density and momentum of both fluids and recovers the Navier-Stokes equation. The other tracks an order parameter which differentiates between the two phases by solving the Cahn-Hilliard equation.

2.2.2 The Cahn Hilliard Model

In order to allow the lattice Boltzmann model to track multiple species at once and to model contact line motion it is coupled to a diffusion equation known as the Cahn Hilliard model. This describes a two phase fluid. Its dynamics are described by the Cahn Hilliard equation(71)

$$\frac{\partial C}{\partial t} + \nabla.(\mathbf{u}C) = M\nabla^2\mu, \tag{2.1}$$

where the composition C is an order parameter which distinguishes between the two phases, M is the mobility of the system and μ is the chemical potential. From eq. 2.1 it can be seen that the evolution of C is driven by gradients in μ.

The chemical potential can be found by minimising the free energy of the system which is given by

$$E_b + E_s = \int_V (E_0(C) + \frac{\kappa}{2}[\nabla C]^2)dV + \int_S (\phi_0 - \phi_1 C_s + \phi_2 C_s^2 - \phi_3 C_s^3 + ...)dS, \tag{2.2}$$

where $E_0 = \beta C^2(1-C)^2$, C_s is the value of the composition on the solid surface and β, κ and ϕ_{1-3} are constants. V and S denote integrating over the volume and the solid surface respectively. E_0 has two minima at $C = 0$ and $C = 1$ leading to the two stable phases.

The first integral on the left hand side of eq. 2.2 corresponds to the free energy of the bulk and the second integral corresponds to the free energy of any solid

surfaces present. Initially ignoring the surface terms, and concentrating on just the bulk and interface terms, an Euler Lagrange minimisation leads to

$$\mu = \frac{\partial E_0}{\partial C} - \kappa \nabla^2 C = const. \tag{2.3}$$

Fixing the boundary conditions to ensure two bulk phases in the system gives an equilibrium profile for C of

$$C(z) = \frac{1}{2} + \frac{1}{2}\tanh(\frac{2z}{\epsilon}), \tag{2.4}$$

where $\epsilon = 2\sqrt{\frac{2\kappa}{\beta}}$ is the interface width. By integrating over the interface the surface tension between the two phases, σ_{12}, can be found:

$$\sigma_{12} = \int_0^1 \sqrt{2\kappa E_0(C)} dC = \frac{\sqrt{2\kappa\beta}}{6}, \tag{2.5}$$

where $\kappa = \beta\epsilon^2/8$.

2.2.3 Surface free energy

To model surfaces the appropriate boundary conditions have to be satisfied. Those relevant to the concentration are the wetting or contact line boundary conditions. These conditions are that there must be no mass flux into the surface and that, at equilibrium, the contact line must make the correct contact angle with the surface. They can be satisfied by applying appropriate boundary conditions to C and μ. The first of these is on μ and takes the form $\mathbf{n}.\nabla\mu_s = 0$ where $\mathbf{n}$ is the surface normal. The boundary condition on C is derived from eq. 2.2 by minimising the total free energy with the surface terms included. This leads to the condition (72)

$$n.\nabla C_s = -\cos(\theta)\sqrt{\frac{2\beta}{\kappa}}(C_s - C_s^2), \tag{2.6}$$

where θ is the equilibrium contact angle of the surface. Applying this condition to obtain the derivatives of C then sets the contact angle on the surface.

2.2.4 Navier Stokes equation

Applying conservation of momentum to a Newtonian fluid leads to the Navier-Stokes equation

$$\rho(\frac{\partial \mathbf{u}}{\partial t}+\mathbf{u}.\nabla\mathbf{u}) = -\nabla p - C\nabla\mu + \nabla\left[\eta(\nabla\mathbf{u}+(\nabla\mathbf{u})^T)\right] + \nabla\left(-\frac{2\eta}{3}\nabla.\mathbf{u}\right)+\rho\mathbf{w}, \quad (2.7)$$

where $\mathbf{u}$ is the velocity, p is the pressure, ρ is the density, η is the dynamic viscosity and $\mathbf{w}$ is the value of any external body forces acting on the system. Under the assumption of incompressibility this simplifies to

$$\rho(\frac{\partial \mathbf{u}}{\partial t}+\mathbf{u}.\nabla\mathbf{u}) = -\nabla p + \eta\nabla^2\mathbf{u} - C\nabla\mu + \rho\mathbf{w}. \quad (2.8)$$

At solid boundaries there are two hydrodynamic boundary conditions which must be satisfied. These are the no slip condition which requires that the velocity tangential to the surface is zero, and the no penetration condition which requires that the velocity perpendicular to the surface and any gradients perpendicular to the surface are zero.

2.3 The discrete Boltzmann scheme

We now describe the numerical approach which we will use to solve eqs. 2.1 and 2.7. Rather than directly solve the Navier-Stokes equations, we consider a Boltzmann equation which reduces to the Navier-Stokes equation in the continuum limit.

2.3.1 Discretisation along characteristics

In order to numerically solve the Boltzmann equation the velocity space has to be discretised. There are several schemes which can be employed which are characterised by the dimension of the system and the number of neighbouring nodes with which information is exchanged. For example the two schemes used in this work are D2Q9, a two dimensional scheme in which information is exchanged with the eight points most closely surrounding any node and D3Q19 a three dimensional scheme

in which information is exchanged with the 18 points surrounding each node(73). The microscopic velocities along these characteristics are written as $\mathbf{e}_\alpha$, where α counts the velocities. They are defined such that in a single timestep a particle moving along one of the velocity directions will have moved from one node to its neighbouring node.

In order to maintain isotropy in these schemes the different directions are given different weightings listed below in table 2.1. t_0, t_1, t_2 represent the weighting of the node itself and the weighting of the nearest neighbour and next nearest neighbour respectively.

	D2Q9	D3Q19
t_0	$\frac{4}{9}$	$\frac{1}{3}$
t_1	$\frac{1}{9}$	$\frac{1}{18}$
t_2	$\frac{1}{36}$	$\frac{1}{36}$

Table 2.1: Directional weighting to ensure isotropy.

2.3.2 Discrete Boltzmann equation

The discrete Boltzmann equation for the transport of density and momentum of an incompressible binary fluid is(65)

$$\frac{Df_\alpha}{Dt} = (\frac{\partial}{\partial t} + \mathbf{e}_\alpha.\nabla)f_\alpha = -\frac{1}{\lambda}(f_\alpha - f_\alpha^{eq}) + \frac{1}{c_s^2}(\mathbf{e}_\alpha - \mathbf{u}).\mathbf{F}\Gamma_\alpha. \tag{2.9}$$

where f is the particle density function, $c_s = \sqrt{1/3}$ is the speed of sound, λ is the relaxation constant, $\mathbf{F}$ is the external force and $\Gamma_\alpha = f_\alpha^{eq}/\rho$. The equilibrium function of f is derived as a leading order expansion of the Maxwell-Boltzmann distribution

$$f_\alpha^{eq} = t_\alpha\rho[1 + \frac{\mathbf{e}_\alpha.\mathbf{u}}{c_s^2} + \frac{(\mathbf{e}_\alpha.\mathbf{u})^2}{2c_s^4} - \frac{(\mathbf{u}.\mathbf{u})}{2c_s^2}]. \tag{2.10}$$

The effective external force is used to account for intermolecular forces which would otherwise be absent from the model. It takes the form

$$\mathbf{F} = \nabla \rho c_s^2 - (\nabla p + C \nabla \mu), \tag{2.11}$$

where the first term is due to the excluded volume, the second is the contribution due to thermodynamic pressure and the third is the pressure contribution due to the presence of interfaces within the system.

The instabilities in lattice Boltzmann codes at a high density ratio generally come about due to the inclusion of a density gradient term in the external force which can get very large in the region of the interface. To counter this effect the particle distribution function, f, which tracks mass and momentum, is reformulated into a pressure and momentum evolution equation by transforming the density function to(65)

$$g_\alpha = f_\alpha c_s^2 + (p - \rho c_s^2)\Gamma_\alpha(0), \tag{2.12}$$

where $\Gamma_\alpha(0) = t_\alpha$. Taking the total derivative of this new function gives the expression

$$\frac{\partial g_\alpha}{\partial t} + \mathbf{e}_\alpha . \nabla g_\alpha = -\frac{1}{\lambda}(g_\alpha - g_\alpha^{eq}) + (\mathbf{e}_\alpha - \mathbf{u}) . \left[\nabla \rho c_s^2 \left(\Gamma_\alpha - \Gamma_\alpha(0)\right) - C \nabla \mu \Gamma_\alpha\right]. \tag{2.13}$$

In this new expression the important thing is that the density gradient is now preceded by a small factor $(\Gamma_\alpha - \Gamma_\alpha(0))$ which offsets its large size.

The information about the concentration is kept track of by a distribution function defined as $h_\alpha = (C/\rho) f_\alpha$. The evolution equation for this distribution function is

$$\frac{\partial h_\alpha}{\partial t} + \mathbf{e}_\alpha . \nabla h_\alpha = -\frac{1}{\lambda}(h_\alpha - h_\alpha^{eq}) + (\mathbf{e}_\alpha - \mathbf{u}) . \left[\nabla C - \frac{C}{\rho c_s^2}\left(\nabla p + C \nabla \mu\right)\right] \Gamma_\alpha. \tag{2.14}$$

Eq. 2.13 and eq. 2.14 define the system which is to be solved.

2.3.3 Recovery of Macroscopic quantities

Macroscopic quantities are recovered from the probability density distributions by taking moments.

$$C = \sum_{\alpha} h_{\alpha}, \tag{2.15}$$

$$p = \sum_{\alpha} g_{\alpha}, \tag{2.16}$$

$$\rho \mathbf{u} = \frac{1}{c_s^2} \sum_{\alpha} \mathbf{e}_{\alpha} g_{\alpha}. \tag{2.17}$$

The continuum equations can be recovered via a Chapman-Enskog expansion of eq. 2.13 yielding

$$\frac{\partial p}{\partial t} + \rho c_s^2 \nabla . \mathbf{u} = 0, \tag{2.18}$$

$$\rho(\frac{\partial \mathbf{u}}{\partial t} + \mathbf{u}.\nabla \mathbf{u}) = -\nabla p - C\nabla \mu + \nabla \left[\rho c_s^2 \lambda . (\nabla \mathbf{u} + (\nabla \mathbf{u})^T)\right]. \tag{2.19}$$

These are the pressure evolution equation and the Navier-Stokes equation with a chemical potential gradient, eq. 2.8 with $\eta = \rho c_s^2 \lambda$ and the external force $\mathbf{w} = 0$. A Chapman-Enskog expansion of eq. 2.14 recovers the Cahn-Hilliard equation eq. 2.1

$$\frac{\partial C}{\partial t} + \nabla . (\mathbf{u} C) = M \nabla^2 \mu. \tag{2.20}$$

2.4 Details of numerical implementation

2.4.1 Spatial differentials

Spatial differentials need to be taken in a way which preserves the rotational symmetry of the problem. To do this the differentials are first taken along each velocity characteristic α and then combined with the appropriate weightings t_{α}. If

ϕ is a generic field the central difference can be defined as

$$\delta t \mathbf{e}_\alpha \cdot \nabla^{CD} \phi|_{\mathbf{x}} = \frac{1}{2}[\phi(\mathbf{x} + \mathbf{e}_\alpha \delta t) - \phi(\mathbf{x} - \mathbf{e}_\alpha \delta t)], \tag{2.21}$$

and the biased difference is

$$\delta t \mathbf{e}_\alpha \cdot \nabla^{BD} \phi|_{\mathbf{x}-\mathbf{e}_\alpha \delta t} \approx \delta t \mathbf{e}_\alpha \cdot \nabla^{CD} \phi|_{\mathbf{x}} - (\delta t \mathbf{e}_\alpha \cdot \nabla)^2 \phi|_{\mathbf{x}} = \frac{1}{2}[-\phi(\mathbf{x}+\mathbf{e}_\alpha \delta t) + 4\phi(\mathbf{x}) - 3\phi(\mathbf{x}-\mathbf{e}_\alpha \delta t)]. \tag{2.22}$$

The second order derivatives can be defined as

$$(\delta t \mathbf{e}_\alpha \cdot \nabla)^2 \phi|_{\mathbf{x}} = \phi(\mathbf{x} + \mathbf{e}_\alpha \delta t) - 2\phi(\mathbf{x}) - \phi(\mathbf{x} + \mathbf{e}_\alpha \delta t) \tag{2.23}$$

The derivatives along the principal directions, which are used when a dot product with the macroscopic velocity is required, can then be found with the following summations:

$$\nabla^{BD} \phi|_{\mathbf{x}} = \frac{1}{c_s^2 \delta t} \sum_{\alpha \neq 0} t_\alpha \mathbf{e}_\alpha (\delta t \mathbf{e}_\alpha \cdot \nabla^{BD}) \phi|_{\mathbf{x}}, \tag{2.24}$$

$$\nabla^{CD} \phi|_{\mathbf{x}} = \frac{1}{c_s^2 \delta t} \sum_{\alpha \neq 0} t_\alpha \mathbf{e}_\alpha (\delta t \mathbf{e}_\alpha \cdot \nabla^{CD}) \phi|_{\mathbf{x}}, \tag{2.25}$$

$$\nabla^2 \phi|_{\mathbf{x}} = \frac{1}{c_s^2 \delta t^2} \sum_{\alpha \neq 0} t_\alpha (\delta t \mathbf{e}_\alpha \cdot \nabla)^2 \phi|_{\mathbf{x}}. \tag{2.26}$$

The mixed difference is given by

$$\nabla^{MD} \phi|_{\mathbf{x}} = \frac{1}{2}(\nabla^{BD} \phi|_{\mathbf{x}} + \nabla^{CD} \phi|_{\mathbf{x}}). \tag{2.27}$$

One thing to note about these derivatives is that such finite difference equations tend to be a major source of instability in the code. Therefore attempting to minimise the number of calculation steps can lead to to increased stability. With this in mind it is preferable to use eqs (2.22-2.23 rather than eqs. 2.24-2.26 if possible as the former contains less numerical steps. When taking $\nabla^2(C)$ it is also preferable

to rearrange eq. 2.3 giving

$$\nabla^2 C = \mu - \frac{\partial E_0}{\partial C}. \tag{2.28}$$

2.4.2 Lattice Boltzmann equations

Eq. 2.13 and eq. 2.14 need to be discretised in time and space. In order to keep second order accuracy this is done using a trapezoid rule along characteristics. The relaxation time is defined as $\lambda/\delta t$ This leads to implicit equations that can be handled by making the following redefinitions of g and h

$$\bar{g}_\alpha = g_\alpha + \frac{1}{2\tau}\left(g_\alpha - g_\alpha^{eq}\right) - \frac{\delta t}{2}(\mathbf{e}_\alpha - \mathbf{u})\left[\nabla^{CD}\rho c_s^2\left(\Gamma_\alpha - \Gamma_\alpha\left(0\right)\right) - C\nabla^{CD}\mu\Gamma_\alpha\right], \tag{2.29}$$

$$\bar{g}_\alpha^{eq} = g_\alpha^{eq} - \frac{\delta t}{2}(\mathbf{e}_\alpha - \mathbf{u})\left[\nabla^{CD}\rho c_s^2\left(\Gamma_\alpha - \Gamma_\alpha\left(0\right)\right) - C\nabla^{CD}\mu\Gamma_\alpha\right], \tag{2.30}$$

$$\bar{h}_\alpha = h_\alpha + \frac{1}{2\tau}\left(h_\alpha - h_\alpha^{eq}\right) - \frac{\delta t}{2}(\mathbf{e}_\alpha - \mathbf{u})\left[\nabla^{CD}C - \frac{C}{\rho c_s^2}\left(\nabla^{CD}p + C\nabla^{CD}\mu\right)\Gamma_\alpha\right], \tag{2.31}$$

$$\bar{h}_\alpha^{eq} = h_\alpha^{eq} - \frac{\delta t}{2}(\mathbf{e}_\alpha - \mathbf{u})\left[\nabla^{CD}C - \frac{C}{\rho c_s^2}\left(\nabla^{CD}p + C\nabla^{CD}\mu\right)\Gamma_\alpha\right], \tag{2.32}$$

where δt is the simulation time step. The dynamical equations then take the form

$$\begin{aligned}\bar{h}_\alpha\left(\mathbf{x},t\right) =& h_\alpha\left(\mathbf{x} - \mathbf{e}_\alpha\delta t, t - \delta t\right) + \frac{1}{2\tau}\left(h_\alpha - h_\alpha^{eq}\right)\Big|_{(\mathbf{x}-\mathbf{e}_\alpha\delta t, t-\delta t)} + \frac{\delta t}{2}M\nabla^2\mu\Gamma_\alpha\Big|_{(\mathbf{x}-\mathbf{e}_\alpha\delta t, t-\delta t)} \\ &+ \frac{\delta t}{2}M\nabla^2\mu\Gamma_\alpha\Big|_{(\mathbf{x},t-\delta t)} - \frac{\delta t}{2}(\mathbf{e}_\alpha - \mathbf{u})\left[\nabla^{MD}C - \frac{C}{\rho c_s^2}\left(\nabla^{MD}p + C\nabla^{MD}\mu\right)\Gamma_\alpha\right]\end{aligned} \tag{2.33}$$

$$\begin{aligned}\bar{g}_\alpha(\mathbf{x},t) =& g_\alpha(\mathbf{x}-\mathbf{e}_\alpha\delta t, t-\delta t) + \frac{1}{2\tau}\left(g_\alpha - g_\alpha^{eq}\right)\big|_{(\mathbf{x}-\mathbf{e}_\alpha\delta t, t-\delta t)} \\ & -\frac{\delta t}{2}(\mathbf{e}_\alpha - \mathbf{u})\left[\nabla^{MD}\rho c_s^2\left(\Gamma_\alpha - \Gamma_\alpha(0)\right) - C\nabla^{MD}\mu\Gamma_\alpha\right]\end{aligned} \tag{2.34}$$

The two equations 2.33 and 2.34 are now in a form which can be conveniently solved on a computer. In the equations the upstream and central gradients are to account for the fact that some gradients are taken after streaming and some are taken before streaming.

2.4.3 Solid surface boundary conditions

At the solid boundary the derivatives perpendicular to the boundary are required to be zero. This can be achieved by assuming that the nodes within the solid surface mirror the nodes outside it. At the surface this leads to the following derivatives in the outgoing direction:

$$\begin{aligned}\delta\mathbf{e}_\alpha.\nabla^{CD}\phi|_{\mathbf{x}} &= 0, \\ \delta\mathbf{e}_\alpha.\nabla^{BD}\phi|_{\mathbf{x}} &= \frac{1}{2}(-\phi(\mathbf{x}_s - 2\mathbf{e}_\alpha\delta t) + 4\phi(\mathbf{x}_s - \mathbf{e}_\alpha\delta t) - 3\phi(\mathbf{x}_s)), \\ \delta\mathbf{e}_\alpha.\nabla^{BD}\phi|_{\mathbf{x}-\mathbf{e}_\alpha\delta t} &= \frac{1}{2}(4\phi(\mathbf{x}_s) - 4\phi(\mathbf{x}_s - \mathbf{e}_\alpha\delta t)).\end{aligned} \tag{2.35}$$

The directional derivatives in the incoming direction are:

$$\begin{aligned}\delta\mathbf{e}_\alpha.\nabla^{CD}\phi|_{\mathbf{x}} &= 0, \\ \delta\mathbf{e}_\alpha.\nabla^{BD}\phi|_{\mathbf{x}} &= \frac{1}{2}(-\phi(\mathbf{x}_s + 2\mathbf{e}_\alpha\delta t) + 4\phi(\mathbf{x}_s + \mathbf{e}_\alpha\delta t) - 3\phi(\mathbf{x}_s)).\end{aligned} \tag{2.36}$$

The second order derivative is then

$$(\delta\mathbf{e}_\alpha.\nabla)^2\phi|_{\mathbf{x}_s} = -(2\phi(\mathbf{x}_s) - 2\phi(\mathbf{x}_s - \mathbf{e}_\alpha\delta t)) \tag{2.37}$$

The exception to this is the wetting boundary condition eq. 2.6 which is used to compute the derivatives of C at the solid surface in order to set the contact time.

At solid boundaries there is an additional problem that the information streaming out of the solid surface is unknown. This can be solved by applying the bounce back scheme, whereby density functions streaming into the wall reverse direction

upon reaching a wall node and stream back out. This also has the advantage of ensuring that the no slip and no penetration condition hold.

2.4.4 Convex and concave corners

Corners on the surface introduce additional complications as they result in additional surface nodes as well as points on the surface at which a surface normal is ill defined. This requires more care when detecting where the surface is, as well as some special considerations depending on the type of corner.

For convex corners the main issue is that for the node at the corner the surface normal is not obvious and this normal is needed to define the derivatives at the surface. The normal is therefore defined in a direction which bisects the corner.

Concave corners have the same problem which is resolved in the same way. They also have the additional complication that for the directional derivative perpendicular to the surface normal all of the relevant nodes are within the surface and the mirror scheme cannot be used to fill in the missing information. This is resolved by assuming that this directional derivative is zero. For a more detailed discussion of corners and how they are handled see the work by Connington et. al.(66).

CHAPTER 3

Bouncing on Curved surfaces

3.1 Introduction

Drops hitting superhydrophobic surfaces can bounce off quickly because of the low friction between the drop and the substrate, either at the end of retraction(44; 18) or at their maximum extension in a pancake shape(74; 75; 76). Normally the drop retains a circular symmetry during the bouncing and the contact time is bounded below by the Rayleigh limit(56). This is the theoretical lower limit on the bouncing time which is set by considering the Rayleigh oscillation time. However Bird *et al.*(45) showed that drops impacting on surfaces where asymmetry is introduced, with ridges an order of magnitude smaller than the drop, leave the surface with shortened contact time. Moreover, the contact time of drops bouncing on a superhydrophobic macrotexture can take discrete values depending on the drop impact point relative to the texture and its impact velocity(52). The left-right symmetry can be also broken by imposing a surface gradient to induce a directional movement(77; 78; 79; 80; 81) or by considering impacts on a moving surface(82; 83). In these studies, the surfaces reported are still macroscopically flat, with the feature size at the scale of microns or nanometres.

In this chapter, we consider asymmetric surfaces with macrotextures comparable to the drop size. We demonstrate that a drop impacting on such surfaces displays

asymmetric bouncing with a $\sim 40\%$ contact time reduction compared to that on the equivalent flat substrate. Experimental visualization shows that the impacting drop undergoes a preferential spreading in one direction and leaves the surface due to fast retraction in the perpendicular direction. Evidence from lattice Boltzmann simulations and analytical analysis reveals that the drop hydrodynamics is due to the anisotropic architecture which engenders an asymmetric momentum distribution and flow coupling.

3.1.1 Simulation approach

The simulations in this chapter were undertaken using the lattice Boltzmann code described in chapter 2. The substrate in the system was a hemispherical cylinder resting on a flat surface. The diameter of this cylinder was used to characterise it and is given in terms of the ratio D/D_0 where D is the diameter of the cylinder and D_0 is the diameter of the liquid drop. The curved cylindrical surface was approximated by a stepped surface, the interface width of the system was then taken to be significantly larger than these steps.

The simulation box was $200\times150\times150$ nodes in size and, as the simulations have two planes of mirror symmetry, reflection boundary conditions were used at the edge of the box. The parameters used in the simulation are given in table 3.1.

The drop is started with an initial velocity just before contact with the surface is made.

3.2 Experimental Results

3.2.1 Asymmetric bouncing on natural surfaces.

The experimentalists first considered the impact of drops on a natural *Echevaria* surface(46). Fig. 3.1a-c show the optical and scanning electron microscopic (SEM) images of the surface. The *Echevaria* leaves approximate cylinders with a diameter of curvature (D) a few millimetres. The surface of the leaves is covered by waxy nanofibers(84) yielding an apparent contact angle over 160°.

Quantity	Value (simulation units)
Surface tension	0.0075
Liquid dynamic viscosity	0.0042
Gas dynamic viscosity	0.000082
Liquid density	1
Gas density	0.0012
Interface width	9
Contact angle	160
Initial velocity	0.04
Drop radius	50
Mobility	0.94
Gravitational constant	0
Weber number, *We*	10.6
Ohnesorge number, *Oh*	0.0068
Bond number, *Bo*	0

Table 3.1: Parameters used in the simulations, and the corresponding dimensionless variables.

The experimental results for the bouncing are very different from those conventionally reported on a flat superhydrophobic surface(85; 86). Fig. (3.1)d presents selected snapshots of a drop of diameter $D_0 = 2.9$ mm impinging on the convex surface of an *Echeveria* leaf with a radius of curvature of ~ 4.1 mm. The impact velocity is $0.63\,\mathrm{m\,s^{-1}}$, corresponding to $We = 7.9$ and Oh=0.0028. The impacting drop initially spreads isotropically, but the drop spreading becomes increasingly anisotropic as the drop starts to retract. Interestingly, when the liquid in the axial (straight) direction has started to retract at ~ 3.8 ms, the liquid in the azimuthal (curved) direction continues to spread, with a sustained fluid transfer from the axial direction. Fig. 3.2 shows a schematic representation of these two directions. Once the fluid in the axial direction has fully contracted at 11.8 ms ($= 1.73\sqrt{\rho r_0^3/\gamma}$), the drop leaves the surface maintaining an elongated shape along the azimuthal direction, indicating that the asymmetric bouncing can be driven by preferential retraction along just one axis. The contact time, t_0, is $\sim 30\%$ faster than that on the equivalent flat substrate(44; 87; 54).

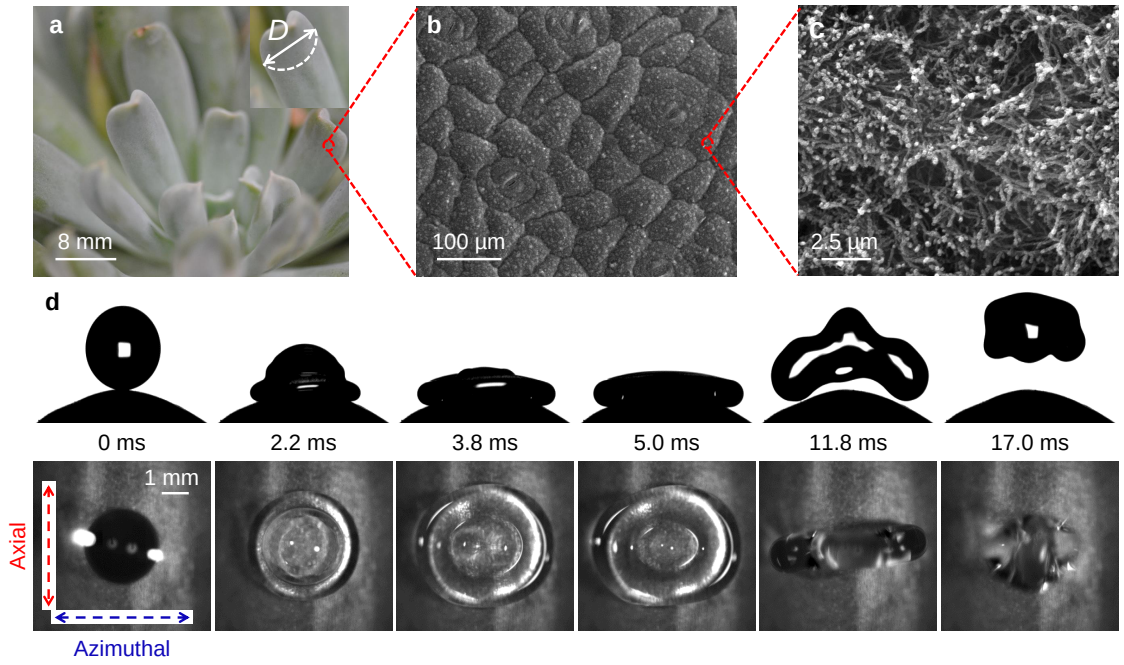

Figure 3.1: **a**, Optical image of *Echeveria* showing the curvature of individual leaves. **b**, Low-resolution scanning electron microscope (SEM) image of an *Echeveria* surface showing protuberances on the scale of 100 microns. **c**, Magnified SEM image of a single protuberance consisting of countless nanofibers. **d**, Selected snapshots showing a drop ($D_0 = 2.9$ mm) impacting on an *Echeveria* leaf at $We = 7.9$. The first row is a cross section parallel to the azimuthal direction and the second is a plan view from above the drop.

3.2.2 Symmetry-breaking in droplet bouncing on synthetic surfaces.

To explore this further, the experimentalists fabricated curved surfaces with varying diameters of curvature D between 4 mm and 20 mm. The surfaces are coated with hydrophobic rosettes of diameter ~ 5 μm to give an intrinsic contact angle of $\sim 160°$.

Drop impact on the fabricated surfaces reveals similar bouncing dynamics to that on the natural surface. Figure 3.3a shows the time-evolution of the spreading diameters in the axial and azimuthal directions on the curved surface with $D = 8$ mm at $We = 7.9$.

To quantify the spreading asymmetry k is defined as the ratio of the maximum values of the drop spreading diameters in the azimuthal and axial directions taken

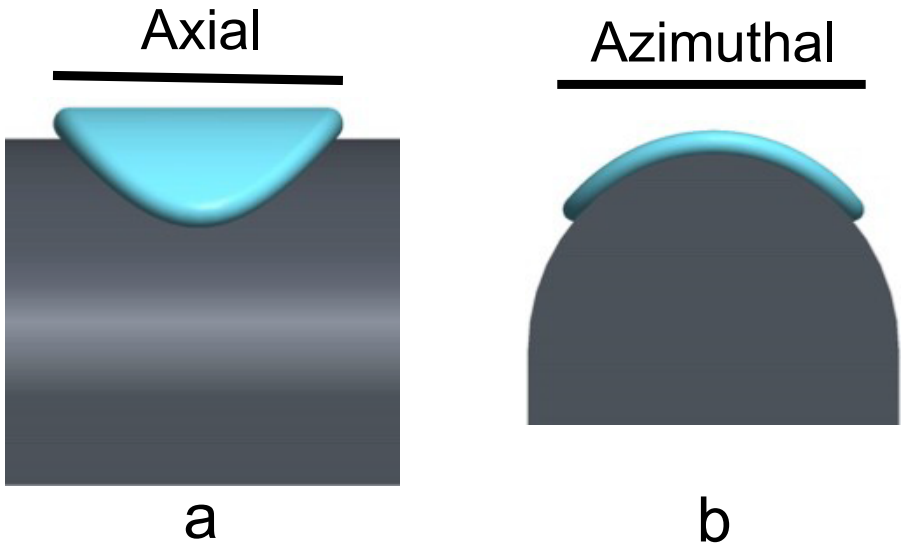

Figure 3.2: A schematic representation of the two directions on the cylinder, **a** the axial direction a and **b** the azimuthal direction.

at different times. Figure 3.3b plots the variation of k as a function of the diameter of curvature normalized by the initial drop diameter (D/D_0). It is apparent that an increase in the structural anisotropy gives rise to a larger k. Figure 3.3c plots the variation of the contact time as a function of normalized diameter of curvature for different *We*. The contact time is also significantly affected by the anisotropy: at a constant *We*, the symmetry-breaking surfaces with smaller diameters of curvature correspond to smaller contact times.

To better elucidate the dependence of the contact time on the surface structure, we decompose the contact time into the spreading time t_1 and retraction time t_2 along the axial direction in fig. 3.3d. It is apparent that the spreading time is almost independent of surface curvature, primarily due to the fact that the spreading is mainly dominated by the inertia. However the retraction time shows a strong decrease with decreasing D: for $D = 6$ mm the total decrease in contact time compared to a flat substrate is $\sim$ 40% for $We \sim 15$. These results, in conjunction with the spreading dynamics shown in fig. 3.3a and b, indicate that the asymmetric bouncing is indeed modulated by the asymmetric curvature whose size is comparable to that of the impacting drop. This argument is also confirmed by a control experiment on the spherical surface where the bouncing is symmetric and the contact time is the same as that on a flat surface shown in fig. 3.4.

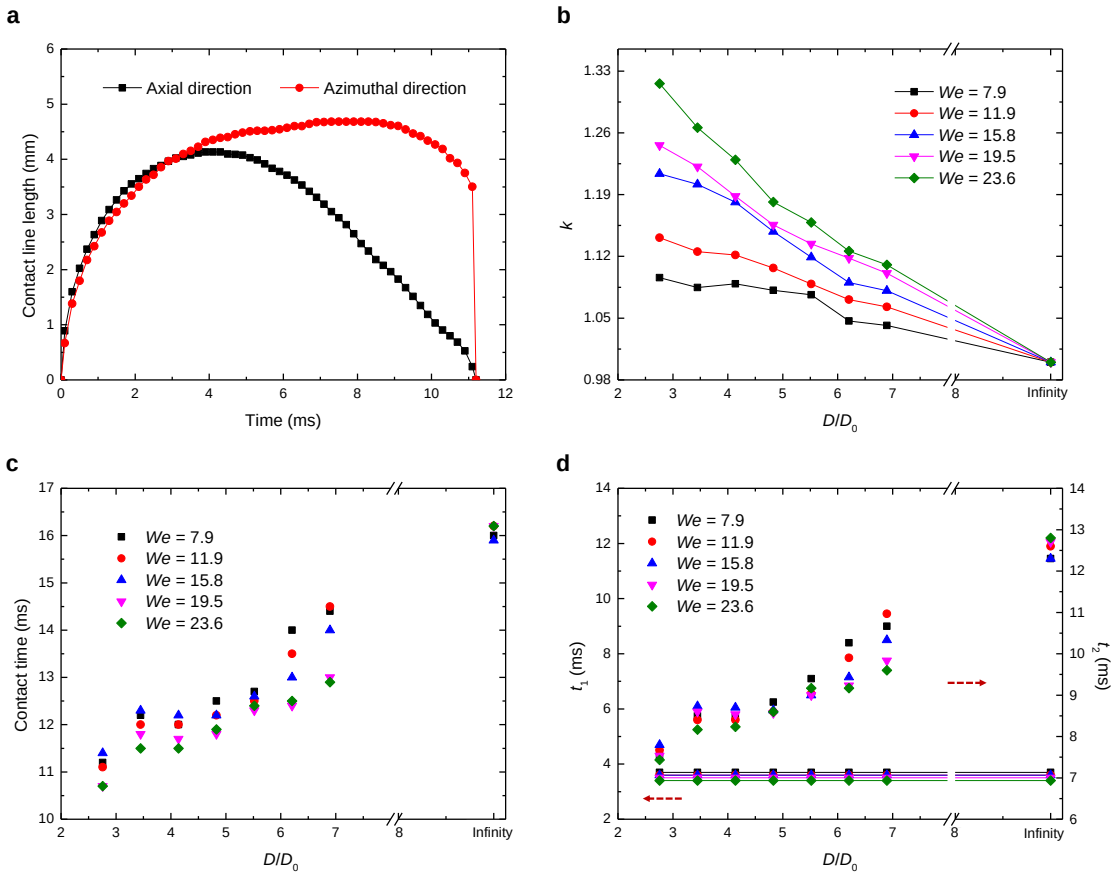

Figure 3.3: **a**, The variations of contact line length in the axial and azimuthal directions as a function of time. **b**, **c** and **d**, The variation of the k (defined as the ratio of the maximum spreading diameters in the azimuthal and axial directions), the contact time, the axial spreading time t_1 (left) and axial retraction time t_2 (right) as a function of surface curvature D (normalised by drop diameter D_0) under different We.

3.3 Simulation Results

To test this interpretation, we modelled the drop impact, using the lattice Boltzmann algorithm described in chapter 2. Figure 3.5 shows how the contact time varies as the cylinder diameter is varied. For the parameter regime looked at in this chapter the contact time is found to decrease as the cylinder diameter is decreased. The region $D/D_0 < 1$ is discussed in greater detail in chapter 4.

Figure 3.6a shows snapshots of the time evolution of a drop impacting on the asymmetric surface obtained from the numerics. The evolution of the drop shape is qualitatively the same as the experiments during the rebound, with the axial

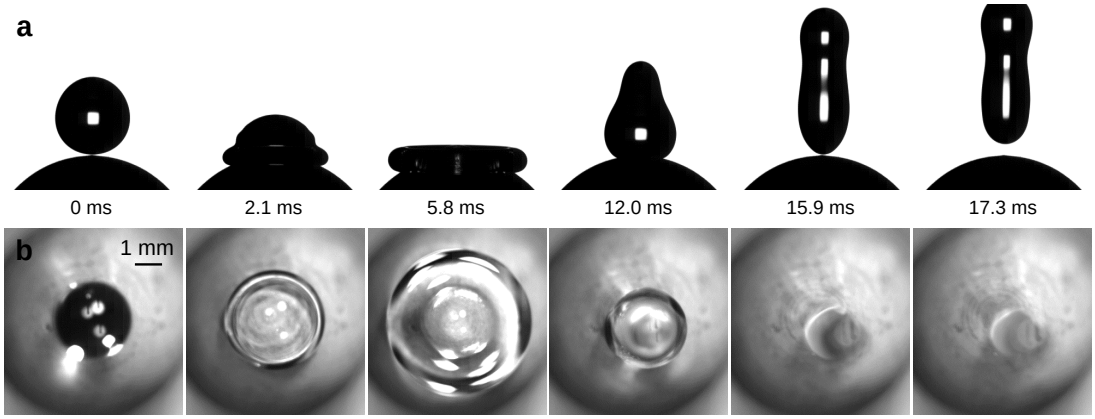

Figure 3.4: Selected snapshots of a drop hitting the top of a spherical (symmetric) superhydrophobic surface. The diameter of the sphere is 8 mm. **a**, High-speed images captured from the side reveal that the contact time is 15.9 ms ($= 2.45\sqrt{\rho r_0^3/\gamma}$ with drop radius $r_0 = D_0/2 = 1.45\,\mathrm{mm}$ and impact velocity $v_0 = 0.63\,\mathrm{m\,s^{-1}}$). This time is close to that on the flat surface, as expected for any impact where the flows have circular symmetry. **b**, Simultaneous plan-view images show that the drop retains a circular symmetry during the entire impact process.

direction starting to retract first.

The colour shading represents the relative heights of the fluid at each time, red high to blue low. Note that in particular (the 3^{rd} image) a large rim develops in the azimuthal direction. The arrows in the figure show the local fluid velocity field.

The simulations allow us to understand how the asymmetric surface topography affects the drop bouncing. Fig. 3.6b displays the variation of the momentum in the horizontal direction relative to the initial impact momentum as a function of time during the impact on the surface with $D/D_0 = 1.2$. In the figure, a positive momentum corresponds to drop spreading whilst a negative momentum corresponds to drop retraction. From the graph, it can be clearly seen that the momentum in the azimuthal direction is always larger than that in the axial direction. When the momentum in the axial direction starts to reverse its direction, the azimuthal momentum remains positive and indeed increases slightly. This is consistent with the experimental observations that the drop sustains a spreading state without retracting in the azimuthal direction, demonstrating the positive feedback from the axial direction that enables this to occur.

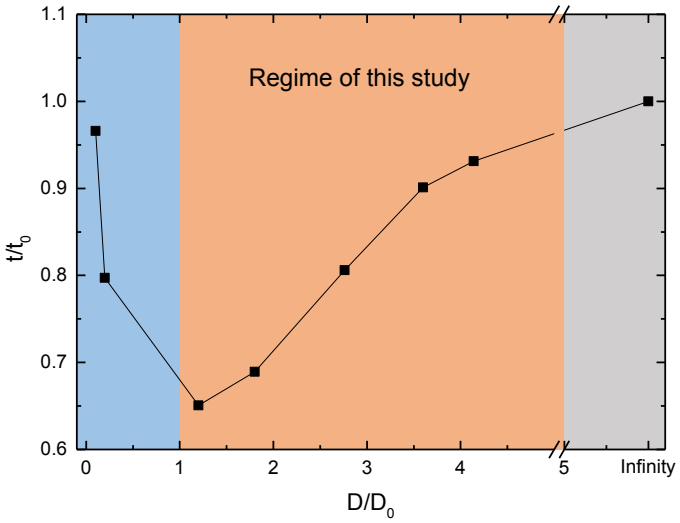

Figure 3.5: Simulations of the variation of the contact time relative to that for a flat superhydrophobic surface, at $We = 10.6$ and $Oh = 0.0068$, against D/D_0, the ratio of the diameter of the drop to the diameter of the cylinder.

As a comparison, we also plotted the variation of momentum on a flat surface (blue curve in fig. 3.6b), which shows that the momentum along any given direction for a flat substrate lies between the two curves for the asymmetric surface.

In order to quantify how the momentum anisotropy is dictated by the surface topography, we calculated the ratio between the maximum momentum in the azimuthal direction and that in the axial direction. As shown in fig. 3.6c, the momentum anisotropy decreases with increasing diameter of curvature.

3.3.1 Applied momentum asymmetry

To further validate that the momentum asymmetry is responsible for the asymmetric bouncing, we simulated drop impact on a flat surface by introducing a momentum asymmetry into the simulation manually immediately after the initial collision. To do this a simulation of an impact onto a flat surface was run up to one thousand time steps. The momentum along one axis tangential to the surface was then increased by a variable factor and the momentum along the perpendicular axis was decreased by the same factor.

Fig. 3.7a and b show snapshots of such a simulation. The top row shows a cut through the centre of the drop with the direction shown being that with the

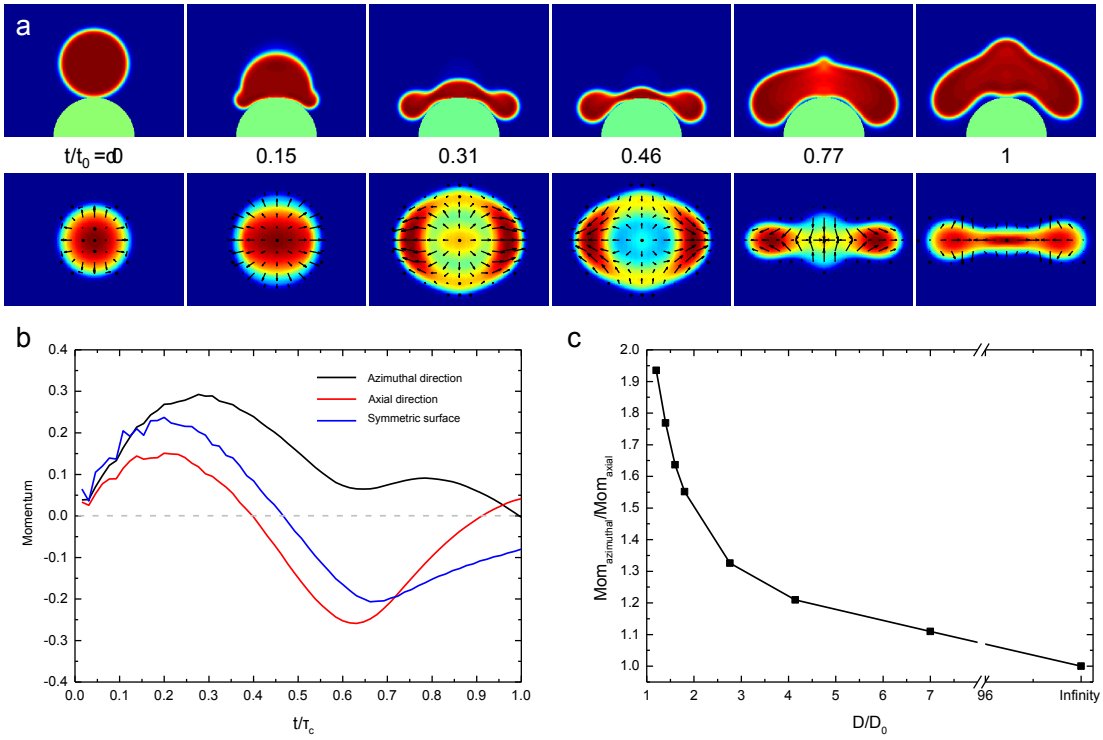

Figure 3.6: **a**, Selected snapshots obtained using the lattice Boltzmann simulation showing the time evolution of a drop bouncing on an asymmetric surface for We =10.6 and Oh = 0.0068. The top panel corresponds to the cross-section view parallel to the azimuthal direction, and the bottom panel is the plan view from above the drop. The colours in the plan view are indicative of the relative height, with respect to the diameter of the drop, of the liquid at each time and arrows indicate the velocity flux. **b**, The time evolution of the momentum normalised by the total initial momentum along the axial (red) and azimuthal (black) directions on the curved surface (D/D_0 =1.2), and for any direction on a flat surface (blue), under the same We =10.6 and Oh = 0.0068. The positive values correspond to the spreading stage whilst the negative values correspond to drop retraction. **c**, The ratio between the maximum momentum transferred into the azimuthal direction and the axial direction as a function of normalized surface curvature D/D_0.

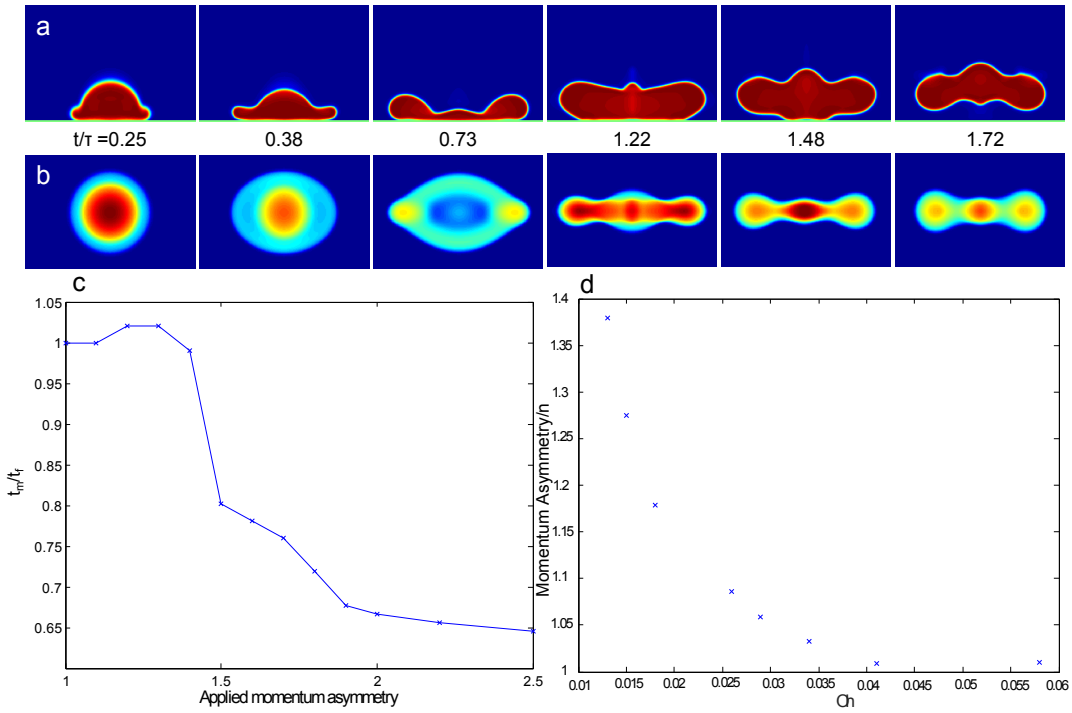

Figure 3.7: **a**, Side view images of a collision with a manually applied momentum asymmetry of 2 at $We = 10.6$ and $Oh = 0.0068$. The times are given below as fractions of the inertial capillary time τ. **b**, Top view images of a collision with an manually applied momentum asymmetry. Colours indicate height of the liquid red high to blue low. **c**, Variation in contact time with variation in applied asymmetry, note that the y axis is normalised by the contact time with no applied asymmetry. **d**, Measured momentum asymmetry against Ohnesorge number for the collision of an ellipsoid shaped drop at $We = 6.36$. The y axis is normalised by the aspect ratio of the ellipsoid n=major axis/minor axis.

increased momentum the 'fast' direction. The bottom row shows a top down image of the collision with the vertical axis being the slow direction and the horizontal axis being the fast direction. The colours, as before, show the height of the liquid at each point, red high to blue low.

The first image is the moment at which the momentum asymmetry is applied. During the spreading the drop then begins to gradually form an ellipsoidal shape in the top down images as shown in the second column. The third column shows the point at which the slow axis (with the lesser original momentum) starts retracting whilst the fast axis is still expanding. The last three images then show the drop lifting off the surface in an elongated shape after the slow axis has retracted. It is

also notable that, like the bouncing on a curved surface, the centre of the drop is the last part to lift off. This is qualitatively the same bouncing pathway as that in fig. 3.6a.

Fig. 3.7d shows how the contact time changes as the applied momentum asymmetry is varied. The time-axis is normalised by the contact time without any applied asymmetry. Initially the contact time actually increases, this is becuase in this case, whilst one axis retracts first, it does not do so with enough force to lift the drop from the surface. Rebound eventually happens after the slow axis contracts. As the slow axis has spread further this retraction occurs at a later time leading to a longer contact time.

As the momentum asymmetry is then further increased the contact time does drop below that seen on a flat surface. We do not yet understand the irregular shape of the curve, but it is probably a result of the unphysical nature of the toy simulations.

3.3.2 Impact of ellipsoidal drops

There are two reasons that the curved surface can induce a momentum asymmetry during the collision. The first of these is that as the force applied to the drop is normal to the surface the curbed surface pushes the liquid outwards, the second is that the impact footprint which the drop forms with a curved surface is asymmetric. The first of these can obviously lead to a momentum asymmetry but so, less obviously, can the second.

This is due to how the momentum is redistributed during the early phases of the collision. A very high pressure region is formed next to the surface. This pressure then pushes outwards on the edges of the drop. The edge which is closer to the centre of the drop along the shorter ellipsoidal axis will therefore be pushed out more as the high pressure central region is closer to the edge of the drop leading to a greater pressure gradient and therefore a greater force. The increased length of the drop edge perpendicular to this axis could also lead to an increased momentum along the axis as there is a greater length of edge for the pressure to push upon.

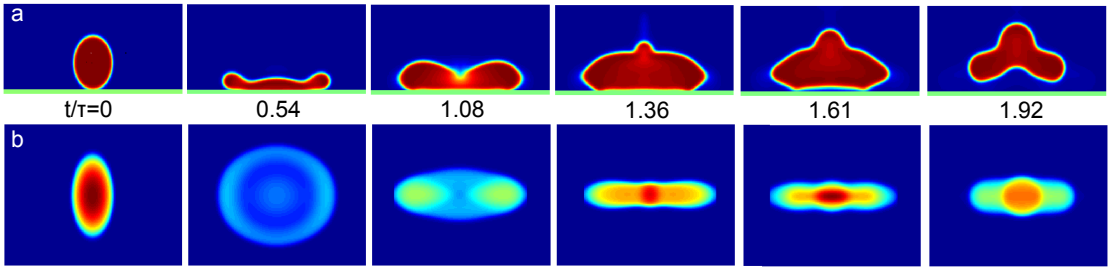

Figure 3.8: **a**, Side view images of a collision with an initially ellipsoidal shape and aspect ratio of 1.4 at $We = 19.5$ and $Oh = 0.0088$. **b**, Top view images of a collision with an initially ellipsoidal shape. Colours indicate height of the liquid red high to blue low. The times are given as fractions of the inertial capillary time τ.

To study this effect further, we simulated an initially elliptical drop impacting a flat substrate. This can shed some light upon the issue as an ellipsoidal drop will have an ellipse shaped footprint with the surface. According to the reasoning above we expect that the momentum along the, initially shorter, minor axis would be greater. There is however a complicating factor in the form of the surface tension which will attempt to return the ellipsoidal drop towards a spherical shape. Hence decreasing the momentum along the long axis and increasing it along the short axis.

To try to discern the degree to which surface tension affects the impact we looked at a series of collisions in which the surface tension was varied and measured the momentum asymmetry. Fig. 3.7d shows the results of these simulations. The y axis shows the momentum asymmetry normalised by the aspect ratio of the ellipsoid whilst the x axis shows the Oh number, used here as a dimensionless measure of the surface tension. For high Oh, which corresponds to low surface tension, the momentum asymmetry tends towards being equal to the initial aspect ratio of the drop. As the surface tension is increased the momentum asymmetry increases. This shows that even when surface tension is reduced to the level that it has no discernible effect the ellipsoidal shaped drop still produces a momentum asymmetry merely due to its geometry as it collides with the surface. Figure 3.8 shows a collision of an ellipsoidal drop at an aspect ratio of 1.4, confirming that the initially shorter axis spreads further and leads to a lift-off in an elongated shape.

Simulations of physical drops, ellipsoidal drops and drops with an imposed

momentum asymmetry have shown that an initial momentum is responsible for the asymmetric bouncing. The next question of course is how the initial momentum asymmetry goes on to effect the overall collision of the drop, and its contact time.

3.4 Models of retraction

We perform a simple hydrodynamic analysis to explain the contact time reduction associated with the asymmetric bouncing. Since the drop spreading is mainly governed by the inertia, we consider the drop retraction process here. The drop retraction is primarily driven by the decrease in surface energy of the thinner central film which leads to a force pulling the rim of the drop inwards. For conventional bouncing as discussed in section 1.3.1, the drop retraction is symmetric and the surface energy of a central film of radius r is $E_s \approx \pi r^2 \gamma(1-\cos\theta)$, where θ is the apparent contact angle, giving a retraction force(38), $F_s = \frac{\partial E_s}{\partial r} \approx 2\pi r\gamma(1-\cos\theta)$. This leads to a constant velocity of retraction because as r decreases the force decreases and the mass of the incoming rim increases.

Due to the preferential spreading on the curved surface, the central film can be approximated by an ellipse with a major axis b (in the azimuthal direction) and minor axis a (in the axial direction). Thus, the surface energy of the central film is $E_a \approx \pi ab\gamma(1-\cos\theta)$. As the asymmetric retraction proceeds the length of the major axis b remains constant while there is a continuous reduction in a. Hence the retraction force is now $F_a \approx \pi b\gamma(1-\cos\theta)$, and the ratio of the force acting on the rim on the curved surface to that on the flat surface is $b/2r$. Experimentally, the drop diameter $2r$ on the symmetric surface continually decreases whilst the azimuthal diameter b on the curved surface remains unchanged. Moreover the mass of the incoming rim in this case remains roughly constant as can be seen from fig. 3.9b. This is due to the liquid flows around the rim during retraction which can be seen in fig. 3.6b. These two facts lead to a constant acceleration retraction with an acceleration of

$$a = \frac{\pi b\gamma(1-\cos\theta)}{m} \tag{3.1}$$

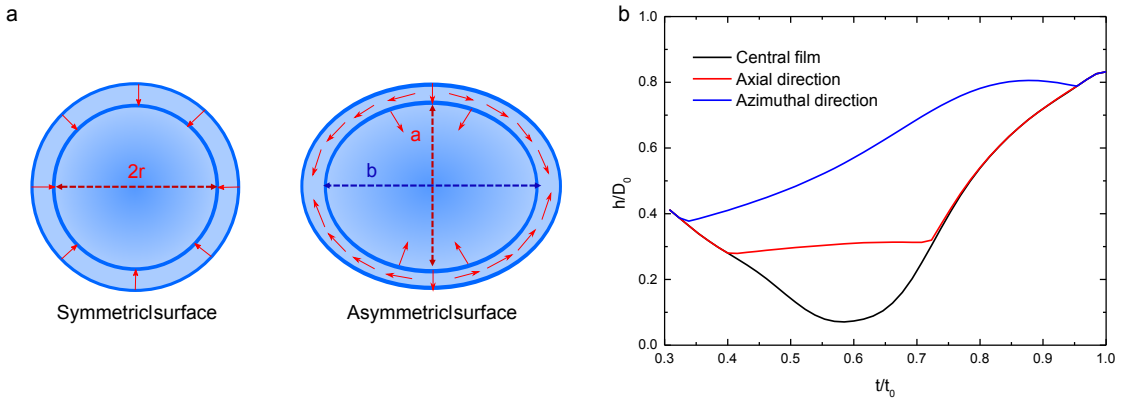

Figure 3.9: **a**, Schematic drawings of the rim and central film on the symmetric and asymmetric surfaces, respectively. On the symmetric surface, the rim retracts uniformly inwards towards the central film. On the asymmetric surface, the central film is an ellipse with major axis b (in the azimuthal direction) and minor axis a (in the axial direction) and retraction is primarily along the axial direction. **b**, Comparison of the time evolution of the normalized rim heights in the axial and azimuthal directions, for the same case as fig. 3.5 based on simulations. The height is scaled by the drop diameter D_0 and time by the contact time t_0. During the retraction stage the axial rim height stays roughly constant whilst the azimuthal rim height increases greatly due to the preferential flow and mass transfer. The reduced mass of the axial rim rendered by the symmetry-breaking flows results in a remarkably efficient pathway for fast drop retraction.

which is significantly faster. A key point here is that the spreading of the larger axis, b, is enhanced by the retraction of the small axis a. As the retraction force on a is proportional to b this leads to a positive feedback causing the asymmetry to grow throughout the retraction. This feedback leads to the initially small asymmetry growing throughout the retraction.

3.5 Discussion

In this chapter we found that drops impacting onto cylindrical shaped structures lift off in an elongated shape after a shortened time. This is due to the fact that early on during the impact a momentum asymmetry was formed. This asymmetry by itself did not have a large effect upon the impact other than to cause one axis to start retracting before the other. Once the retraction started however the asymmetry

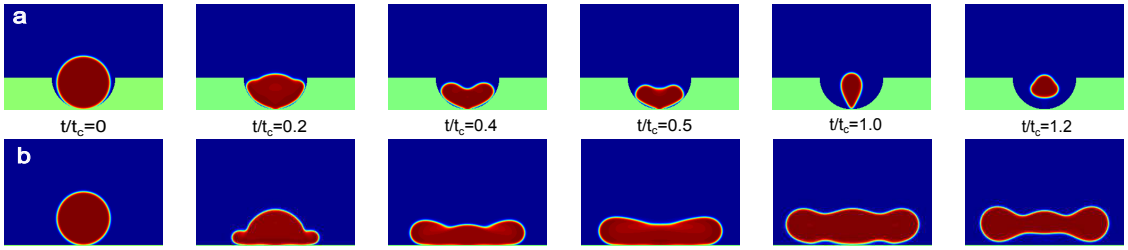

Figure 3.10: **a**, View down axial direction for a collision with a concave surface for We =10.6 and Oh = 0.0028. Time is given as a fraction of the contact time t_c. **b**, Slice cut view along the axial direction of a collision with a concave surface.

grew. There were two reasons for this, firstly that as one axis was still large whilst the other was retracting the retraction force was increased and secondly that there was significant flow of mass around the rim keeping the mass of the incoming rim roughly constant.

From a broad perspective, we expect that rapid bouncing driven by an asymmetric momentum transfer occurs on many surfaces that have asymmetric structure on the order of the drop size. The most obvious extension is to a surface which is concave in one direction and flat in the perpendicular direction. Fig. 3.10 shows snapshots of a simulation of bouncing on such a surface. This can be seen to have a very similar effect to the cylindrical surfaces with the exception that the faster retraction is along the curved direction rather than along the axial direction. Indeed the contact time reduction is even more pronounced than that on the convex surface, suggesting that corrugated surfaces may be candidates for enhanced water repellency and other applications. There will be difficulties however. For example between the concave and convex parts of a corrugated surface there is a region that most closely resembles a sloped flat surface from which no reduction in contact time would be expected. Morever the effect of the size of the impacting drop relative to the corrugation would be a key factor that would need to be understood.

It is interesting to look more closely at the effects of varying the impact velocity and to expand the regime of the study down to smaller cylinder radii. These questions are both addressed in the next chapter.

CHAPTER 4

Bouncing on obstacles of varying size

4.1 Introduction

In chapter 3 we studied the impact of drops upon cylindrical structures larger than the drop. We found an anisotropic bouncing pathway that leads to a reduction in the contact time. This reduction occurs because the asymmetric surface leads to one of the drop axes starting to retract whilst the other is still large. Flows around the rim of the drop then keep the mass of the incoming rim low, leading to its faster retraction and hence a faster lift-off.

The work by Bird *et al.*(45), which looked at the impacts of drops on very small ridges, provides insight into what happens when a drop bounces on an obstacle smaller than its diameter. In this work it was shown that the retraction along the ridge is enhanced and leads to a pinch-off which splits the drop in two. These two separate droplets then retract separately and leave the surface after a shortened time. Bird *et al.* noted that this contact time reduction was greatest when the drop hit the ridge centrally and decreased when the drop was off-centre.

The enhanced retraction along the ridge was explained as being due to the smaller height of the film on the ridge. This is expected to increase the retraction velocity of the rim in a way described by eq. 1.13. If r_{max} is the total spreading radius, v is the retraction velocity and v_p is the retraction velocity along the ridge,

the total retraction time is then denoted $T = T_1 + T_2$ where $T_1 = r_{max}/V_p$ is the ridge dewetting time and $T_2 = (r_{max} - vT_1)/(2v)$ is the time to bounce after the ridge retraction.

The most pertinent work about the effect that the impact velocity has on the impact is that by Gauthier *et al.*(52) who consider bouncing on small ridges. They showed that the contact time on such small obstacles changes with impact velocity in a step like pattern. For low velocity impacts the contact time was reduced relative to a flat surface and roughly constant as the velocity was increased, then at a certain critical impact velocity the contact time was reduced further to a lower plateau.

This was explained with a scaling argument based upon the number of lobes the drop formed as it bounced. Recall that the time scale for the bouncing is $\tau = \sqrt{\rho R^3/\sigma}$. For slower impacts the drop effectively retracts as 2 separate lobes leading to an expected drop in retraction time of $t_0/\sqrt{2}$ where t_0 is the flat surface contact time. For faster retractions however the drop was seen to form four separate lobes leading a contact time of $t_0/2$. These simple scaling predictions were found to fit the data well.

In this chapter we look at simulations varying the size of the ridge below $D/D_0 \approx 1$ and the velocity of the impact.

4.2 Results

4.2.1 Simulation approach

The simulations in this chapter were undertaken using the lattice Boltzmann code described in chapter 2. The substrate in the system was a hemispherical cylinder resting on a flat surface. The diameter is D, and we measure it in terms of the ratio D/D_0 where D_0 is the diameter of the liquid drop.

The simulation box was $200 \times 200 \times 200$ nodes in size and as the simulations have two planes of mirror symmetry reflection boundary conditions were used at the edge of the box. The parameters used in the simulation are given in table 4.1.

Quantity	Value (lattice units)
Surface tension	0.0083
Liquid dynamic viscosity	0.0084
Gas dynamic viscosity	0.00019
Liquid density	1
Gas density	0.0012
Interface width	5
Contact angle	160
Initial velocity	0.04-0.08
Drop radius	50
Cylinder radius	10-120
Mobility	0.94
Gravitational constant	0
Weber number, *We*	19-77
Ohnesorge number, *Oh*	0.013
Bond number, *Bo*	0

Table 4.1: Parameters used in the simulations, and the corresponding dimensionless variables.

The simulation is initialised with the drop just above the surface and with an initial velocity which is varied to provide a range of Weber numbers.

4.2.2 Varying ridge size

Fig. 4.1 shows the variation in the contact time for several different Weber numbers as the ratio between the ridge size and the drop size is varied. The time on the y axis is non-dimensionalised by the inertial capillary time $\tau = \sqrt{\frac{\rho R^3}{\sigma}}$. The x axis is the ratio of the diameter of the cylindrical ridge to the diameter of the liquid drop. For $D/D_0 > 1$ the contact time decreases as the size of the ridge is reduced, a trend which is seen for the entire range of Weber numbers. This is because as the size of the ridge is reduced its curvature increases and, as explained in section 3.4, the increased asymmetry leads to a decrease in the retraction time.

Fig. 4.2 shows snapshots of a collision at We=42 and $D/D_0 = 1.8$ which falls within this regime. The top row shows a slice through the centre of the drop whilst the bottom row shows a top down view of the drop. The drop hits the surface and spreads into a slightly anisotropic shape during the spreading stage. During retraction the asymmetry is increased as the drop begins to retract along the cylinder's axis first. The drop then lifts off once this retraction is complete with

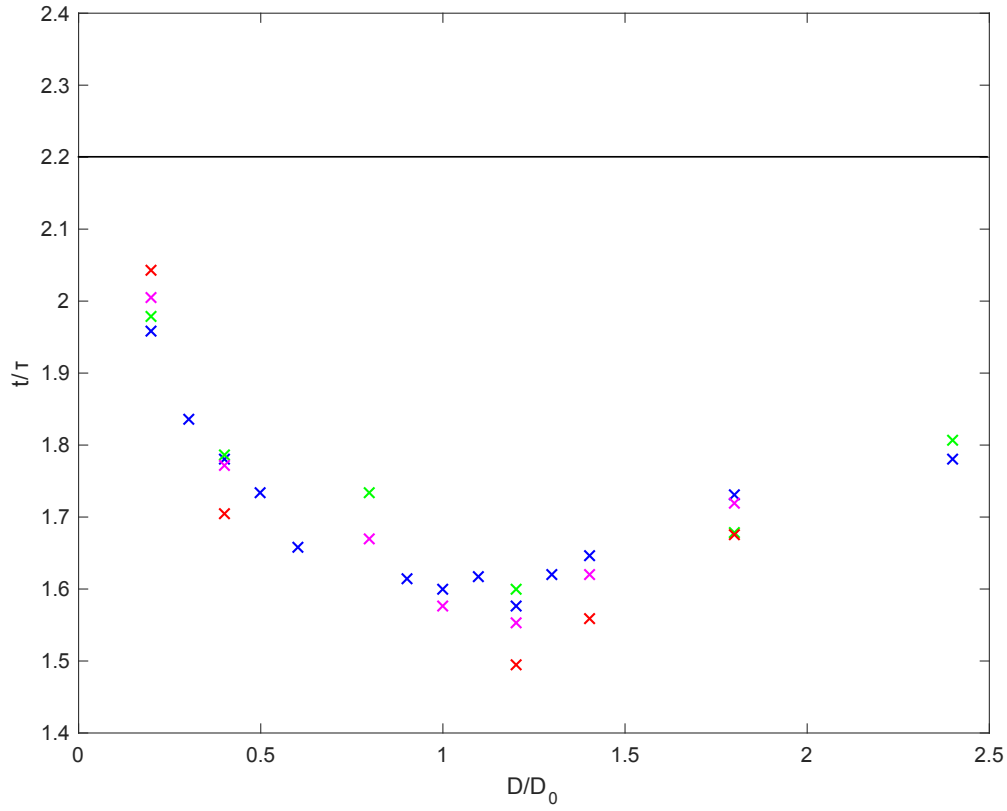

Figure 4.1: Contact time normalised by the inertial capillary time against the ratio of cylinder diameter D to drop radius D_0, for We=19 green, We=43 blue, We=59 magenta and We=77 red. The black horizontal line shows the theoretical minimum contact time on a flat surface.

the central portion of the drop being the last to lift off.

At $D/D_0 \approx 1$ the contact time reaches a minimum and, as the ridge continues to decrease in diameter, the contact time begins to increase with a gradient far greater than the reduction seen for larger ridges. Eventually, for very small ridge sizes, the contact time begins to approach the minimum value predicted for a flat surface, 2.2τ. This is unsurprising as a very small ridge becomes indistinguishable from a flat surface. In the simulations it becomes non-physical to resolve the obstacle when it becomes similar in size to the interface width. This sets a limit on the size of features which can be distinguished.

Fig. 4.3 shows a collision at We=43, $D/D_0 = 0.4$ in which the drop contacts the flat surface as well as the cylindrical ridge. As for $D/D_0 > 1$ there is a slight asymmetry during the spreading stage. The fluid which has spread along the cylinder once again starts retracting first. However in this case only a part of the

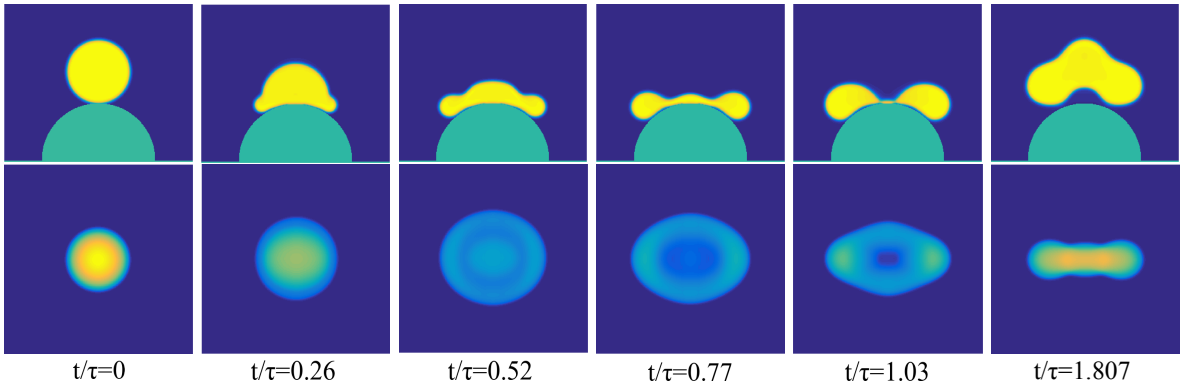

Figure 4.2: Snapshots of a collision at We=43, D/D_0=1.8. The top row shows cuts through the centre of the drop whilst the bottom row shows a top down view of the drop where the colour corresponds to the height of the drop at each point yellow high to blue low.

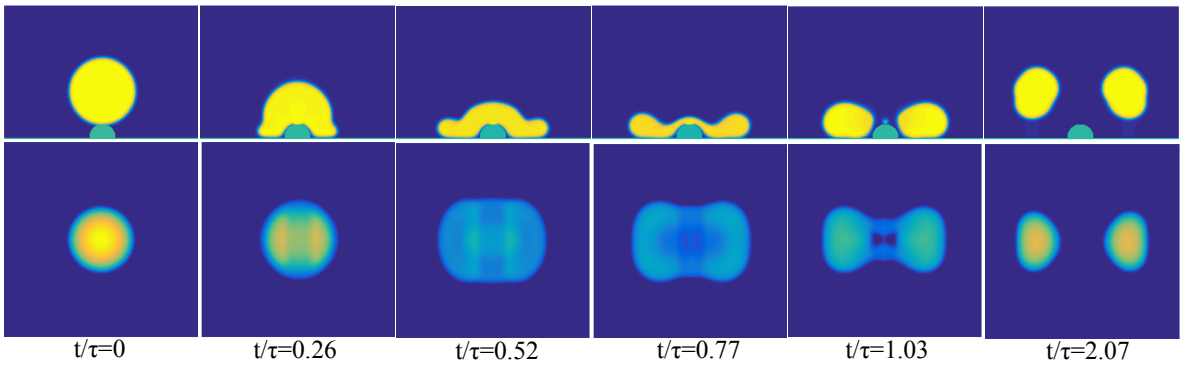

Figure 4.3: Snapshots of a collision at We=43, D/D_0=0.4. The top row shows cuts through the centre of the drop whilst the bottom row shows a top down view of the drop where the colour corresponds to the height of the drop at each point yellow high to blue low.

drop is on the cylinder so there is a localised retraction along a central strip of the drop whilst the rest of the drop contracts normally. This leads to a central pinch-off splitting the drop in two midway through the impact. From this time onwards the drop retracts as two separate droplets, both from the original outer edges of the drops and from the inner edges near the ridge. When the two edges of each droplet meet they lift off.

A point worth noting is that the time for the central portion of the drop to retract along the ridge continues to decrease as the ridge size is decreased even in the $D/D_0 < 1$ regime. However in this regime this retraction does not lead immediately to lift-off but rather to a drop splitting and the beginning of a second retraction stage.

The minimum in fig. 4.1 can therefore be explained by a change in the bouncing pathway which happens for $D/D_0 \approx 1$. For cylinders larger than the drop size the drop does not contact the flat surface to a significant degree and the whole drop retracts with an enhanced speed along the cylinder axis leading to an early lift-off as described in section 3.4. For smaller cylinders however, the flat surface plays a significant role in the collision. The retraction along a central strip corresponding to the cylinder is enhanced leading to a pinch-off and the drop splitting partway through the collision. After this split the two new droplets retract both from the original outer edge of the drop and from the ridge. This is the mechanism seen and described by Bird et. al.(45).

We now consider larger impact velocities and hence larger *We*. We first consider $D/D_0 > 1$. Fig. 4.4 shows a collision at $We = 77$, $D/D_0 = 1.8$, which should be compared with fig. 4.2 for $We = 42$ at the same D/D_0. This faster collision upon a large cylinder produces some interesting variations in the bouncing dynamics. The drop almost splits during the spreading step and the effect of this on the distribution of fluid affects the subsequent bouncing. The asymmetry produced during the spreading is also enhanced, which is to be expected as this initial asymmetry is inertially driven. During the retraction the asymmetry further increases as the drop retracts primarily along the axial direction before lifting off when this retraction

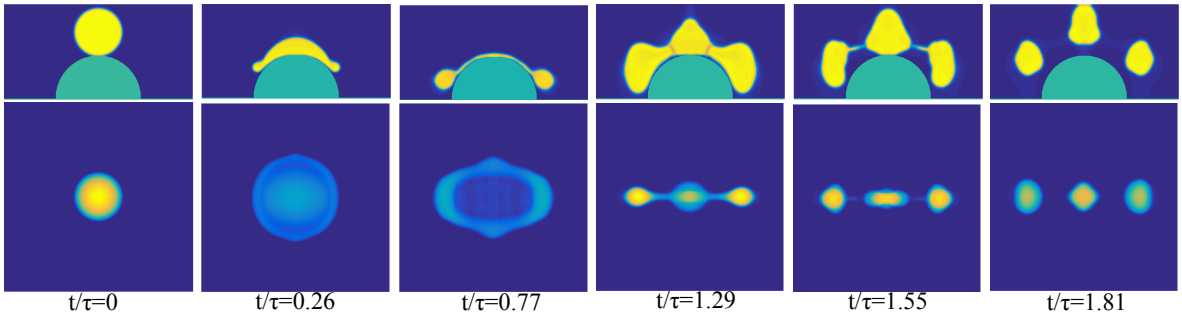

Figure 4.4: Snapshots of a collision at $We = 77$, D/D_0=1.8. The top row shows cuts through the centre of the drop whilst the bottom row shows a top down view of the drop where the colour corresponds to the height of the drop at each point yellow high to blue low.

has completed.

An easily noticeable difference between $We = 77$ and $We = 42$ however is that, as the drop lifts-off, it is split into three droplets. From looking at the top down images in fig. 4.4 the origin of the splitting is apparent by $t/\tau = 0.77$ as already most of the fluid is gathered in either the central region or at the edges of the drop. As the retraction progresses the lack of fluid in the intervening regions eventually leads to the drop splitting up. This splitting, unlike that seen in the case with smaller cylinders, does not have much of an effect upon the contact time as the drop still lifts off after the axial direction has retracted with the split occurring close to the time of lift-off.

Consider now the effect of higher We for smaller cylindrical obstacles. Fig. 4.5 shows a collision at $We = 77$ and $D/D_0 = 0.4$. This is similar to the collision at $We = 42$ on this size of cylinder shown in fig. 4.2 except that the shape of the two droplets to either side of the ridge changes significantly. In particular, as can be seen at times $t/\tau = 0.52$ and $t/\tau = 0.77$ in fig. 4.5, a butterfly wing configuration is formed. This agrees with experiments following the fast impact of drops upon ridges(52). In this paper it was found that similar changes in the shape of the split droplets led to a further reduction in contact time. The contact time scaling acted as if the drop had split into four drops rather than two, a conclusion which was motivated by the appearance of four distinct sub-regions in the experiments. We do not see the step-down in retraction time which was reported in(52). However a brief lift-off is seen at times before the measured contact time. (As the drop

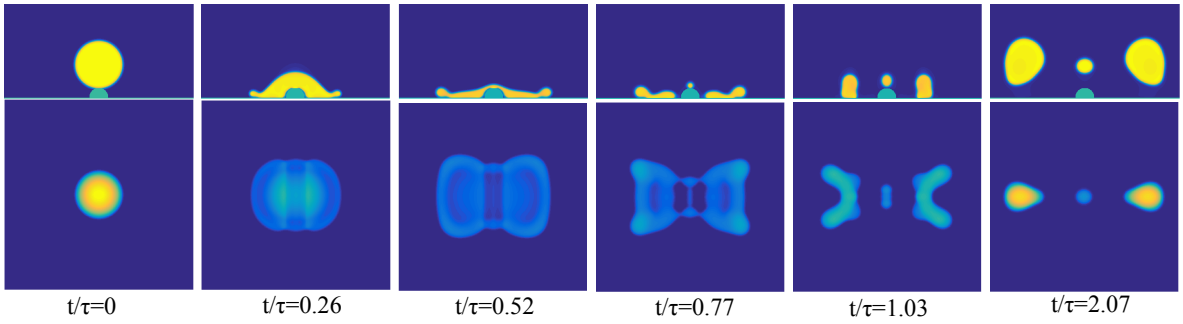

Figure 4.5: Snapshots of a collision at We=77, D/D_0=0.4. The top row shows cuts through the centre of the drop whilst the bottom row shows a top down view of the drop where the colour corresponds to the height of the drop at each point: yellow high to blue low.

quickly re-contacted this time was not taken as the actual contact time.) It may therefore be that the simulations cannot reach a high enough Weber number to unambiguously identify 4 lobe bouncing, but that we are seeing early signs of its emergence.

4.2.3 Discussion

The ways in which drops bounce upon cylindrical ridges has been shown to vary substantially as the size of the ridge is varied. In particular there are two distinct regions in which varying the size of the ridge has opposite effects upon the contact time. The key distinguishing factor between these two regions is the extent to which the drop interacts with the flat surface on which the ridge is placed. For larger ridges the drop never contacts the flat surface and the anisotropic curvature of the surface is responsible for the contact time reduction. As the curvature increased the contact time reduction is enhanced.

As the ridge becomes smaller than the drop however, the drop will inevitably begin to contact the flat surface leading to a change in the dynamics. There is also a reduction in contact time, but now due to a different mechanism. This is that seen by Bird et. al.(45) whereby the retraction of the drop in the central region corresponding to the cylinder is enhanced. This retraction then creates a pinch-off point which leaves two drops on the surface rather than one. These two droplets are smaller than the original drop and thus leave the surface after a shorter time as the time scale of the system $\tau = \sqrt{\frac{\rho R^3}{\sigma}}$ scales with the size of the drops. This contact

time whilst reduced from that seen on the flat surface, is generally larger than that seen in the $D/D_0 > 1$ regime. This is because in the $D/D_0 > 1$ regime the drop lifts off after the retraction along the cylinder. By comparison in the $D/D_0 < 1$ regime the retraction along the cylinder does not immediately lead to drop lift off.

There is more work to be done to look at the effect that the shape of the obstacle has upon the impact. It is expected that the exact details of the shape, for example whether it it a cylinder or a square ridge, matters little in the $D/D_0 < 1$ regime. However the effect may be much higher in the $D/D_0 > 1$ regime. Moreover the lack of curvature for the square ridge could be of import.

CHAPTER 5

A simple model of droplet bouncing

5.1 Introduction

The interaction of water droplets with solid surfaces is of importance to a wide range of applications including ink-jet printing(3), spray cooling(5), ice accumulation(41; 88) and soil erosion by rainfall(89). The impact process can be complex: Depending on their size, impact velocity, and the nature of the surface, drops can be deposited on the surface, break-up and splash, or bounce(90; 7; 91).

When a drop lands on a solid surface inertial forces mediated by the contact with the surface cause the drop to spread out laterally. As it does so, its kinetic energy is transformed into surface energy. The fluid comes to rest and the stored surface energy causes the drop to retract towards its original spherical shape. If it does so with enough energy it will rebound from the surface. The timescale associated with the bouncing follows from a scaling argument balancing inertia and surface tension as $\tau \sim (\rho R^3/\sigma)^{\frac{1}{2}}$ where ρ is the density, R is the radius and σ is the surface tension of the drop.

Superhydrophobic surfaces are characterised by high contact angles and low contact angle hysteresis (12; 19; 92; 28; 50). Richard *et al.*(44) performed experiments showing that the contact time of a bouncing drop on a superhydrophobic surface is 2.6τ for high enough impact speeds, and that viscosity is not important in some

regimes of droplet bouncing. Almost elastic collisions can also be achieved on a Leidenfrost surface or if a trapped air layer is preserved below the drop(93; 94).

One theoretical approach to describing drop bouncing is in terms of the normal modes of vibration. In a classic paper Rayleigh(56) calculated the period of small oscillations in the shape of a drop about the spherical equilibrium as 2.2τ, a more recent treatment can be found by Landau(95). Courty *et al.*(96)extended this work to drops at a surface. They found that introducing a surface increased the oscillation period compared to free oscillations and, assuming that the contact time can be viewed as half an oscillation period of the lowest frequency harmonic, predicted a contact time of 2.3τ.

More recently several authors have described droplet bouncing on surfaces that lack isotropic symmetry. Examples, discussed extensively in chapters 3 and 4, include micro-scale ridges on a flat surface(45), superhydrophobic stripes(97), cylindrical substrates(46), and wires laid upon surfaces(52). These experiments and simulations showed that inducing asymmetric bouncing modes reduces the contact time of a drop on a surface below that found for axially symmetric collisions.

In sec. 5.2 we introduce a simple model of drop bouncing. Our model has the advantage over the Rayleigh approach in that it does not assume small deformations of the drop so can go beyond linearity. In sec. 5.3 we present our results. We consider the axisymmetric and asymmetric motion of a free drop, showing that the drop oscillates chaotically in the asymmetric case. We then calculate the contact time of an axisymmetric bouncing drop, which decreases to a constant value with increasing Weber number, in qualitative agreement with experiments. Next asymmetries in velocity, initial droplet shape, or drag are introduced. We show that the model reproduces the reduced contact time and lift-off in an elongated shape that results from asymmetry, and we explain why this is the case.

5.2 The droplet model

5.2.1 The free drop

We introduce a simple model which reproduces many of the features of droplet bouncing. Our first assumption is to work in the zero viscosity limit of an ideal fluid and assume zero friction with the surface. This means that the system is conservative and hence can be described by a Lagrangian. Secondly, we assume that the drop always takes an ellipsoidal shape which can be characterised by its three axes, of lengths a, b, c along x, y and z respectively. Hence its volume, which is a conserved quantity, is $V_0 = 4\pi abc/3$. A convenient choice of velocity which allows the problem to be recast in terms of the evolution of the lengths of the ellipse axes, is

$$\mathbf{u} = \left(x\frac{\dot{a}}{a},\ y\frac{\dot{b}}{b}\ , z\frac{\dot{c}}{c} \right). \tag{5.1}$$

There are two contributions to the Lagrangian describing the drop, the kinetic energy and the potential energy. The kinetic energy, T, follows by integrating over the volume of the ellipse. The choice of origin for this integration determines the centre of mass motion of the drop; here we take the origin to be the centre of the ellipse, corresponding to no centre of mass motion, and giving

$$T = \int \frac{\rho}{2}\{u_x^2 + u_y^2 + u_z^2\}dV = \frac{\rho V_0}{10}\{\dot{a}^2 + \dot{b}^2 + \dot{c}^2\} \tag{5.2}$$

where ρ is the density of the bouncing fluid.

We consider drops smaller than the capillary length and neglect gravity. Therefore the only contribution to the potential energy of the drop arises from the surface tension, σ, and is proportional to the surface area of the ellipsoid. As the surface area is in general given by elliptical integrals an approximation is useful(98)

$$U = 4\pi\sigma\{\frac{(ab)^{1.6} + (bc)^{1.6} + (ac)^{1.6}}{3}\}^{\frac{1}{1.6}}. \tag{5.3}$$

This formula gives a relative error of less that 1.42% for all ellipse shapes.

The Lagrangian of the system is

$$\mathcal{L} = T - U + p(\frac{4\pi abc}{3} - V_0) \tag{5.4}$$

where the final term is a Lagrange multiplier added to enforce the incompressibility constraint. The resulting Euler-Lagrange equations are

$$\begin{aligned}
\frac{\rho V_0}{5}\ddot{a} &= -\partial_a U + p\frac{4\pi bc}{3}, && (5.5)\\
\frac{\rho V_0}{5}\ddot{b} &= -\partial_b U + p\frac{4\pi ac}{3}, && (5.6)\\
\frac{\rho V_0}{5}\ddot{c} &= -\partial_c U + p\frac{4\pi ab}{3}, && (5.7)\\
\frac{4\pi abc}{3} &= V_0. && (5.8)
\end{aligned}$$

This system of equations describing the bouncing drop may be re-written using the system of units with length measured in units of the drop radius R and time measured in units of $\tau_s = (\rho R^3/\sigma)$ as

$$\begin{aligned}
I\ddot{\tilde{a}} &= -\partial_{\tilde{a}}\tilde{U} + \tilde{p}\tilde{b}\tilde{c}, && (5.9)\\
I\ddot{\tilde{b}} &= -\partial_{\tilde{b}}\tilde{U} + \tilde{p}\tilde{a}\tilde{c}, && (5.10)\\
I\ddot{\tilde{c}} &= -\partial_{\tilde{c}}\tilde{U} + \tilde{p}\tilde{a}\tilde{b}, && (5.11)\\
\tilde{a}\tilde{b}\tilde{c} &= 1, && (5.12)
\end{aligned}$$

where $I = 1/5$, $\tilde{a} = a/R$ and $\tilde{p} = pR/\sigma$. Denoting $(\tilde{a}, \tilde{b}, \tilde{c}) = \tilde{\mathbf{a}}$, the Lagrangian of the system can be rewritten as

$$\tilde{\mathcal{L}} = \tilde{T}(\dot{\tilde{a}}) - \tilde{U}(\tilde{\mathbf{a}}) + \tilde{p}(\tilde{a}\tilde{b}\tilde{c} - 1), \tag{5.13}$$

where

$$\tilde{T}(\dot{\tilde{a}}) = \tilde{T}(\dot{\tilde{a}}, \tilde{b}, \dot{\tilde{c}}) = \frac{1}{2}(I\dot{\tilde{a}}^2 + I\dot{\tilde{b}}^2 + I\dot{\tilde{c}}^2) \tag{5.14}$$

is a quadratic form of $\dot{\mathbf{a}}$ and

$$\tilde{U}(\tilde{\mathbf{a}}) \approx 3^{1-1/\alpha}((\tilde{a}\tilde{b})^{\alpha} + (\tilde{b}\tilde{c})^{\alpha} + (\tilde{c}\tilde{a})^{\alpha})^{1/\alpha}, \tag{5.15}$$

where $\alpha \approx 1.6$. $U(\tilde{\mathbf{a}})$ is a homogeneous function of degree 2. Notice also that since the system conserves energy,

$$\tilde{T}(\dot{\tilde{\mathbf{a}}}) + \tilde{U}(\tilde{\mathbf{a}}) = \tilde{E}, \tag{5.16}$$

where $\tilde{E}$ is constant on any trajectory. In the current system of units $\tilde{E} = We/2 + 3$.

5.2.2 The bouncing drop

The formalism can be extended to describe a drop hitting a flat surface at $z = -c$ by choosing a velocity field

$$\mathbf{u} = \left(x\frac{\dot{a}}{a},\ y\frac{\dot{b}}{b}\ , (z+c)\frac{\dot{c}}{c} \right). \tag{5.17}$$

For a drop that initially lies above the surface this is equivalent to enforcing a no-penetration condition because the vertical component of velocity changes sign at $z = -c$. The model represents slip boundary conditions, and a contact angle of 180^o as there is only ever a single point of contact between the drop and the surface. The free drop kinetic energy, Eq. (5.14), is replaced by

$$T(\dot{\mathbf{a}}) = T(\dot{a}, \dot{b}, \dot{c}) = \frac{1}{2}(I\dot{a}^2 + I\dot{b}^2 + (I+\delta)\dot{c}^2) \tag{5.18}$$

where the additional term in the kinetic energy is the energy associated with the motion of the droplet centre of mass, which now moves as c varies. $\delta = 0$ and $\delta = 1$ for a free and bouncing drop respectivly. For small amplitudes the drop oscillates without lifting off the surface. At higher amplitudes oscillations do not occur, but instead the drop leaves the surface after a given contact time. It is assumed that for the time prior to the drop lifting off the surface $\ddot{c} > 0$ as the surface exerts a positive force on the drop. Therefore we identify the time of lift-off by $\ddot{c} = 0$ and

$\dot{c} > 0$.

Contact line drag can be modelled by adding forcing terms of the form $F_a = -k_a \dot{a} b$ and $F_b = -k_b \dot{b} a$ to eq. 5.5 and eq. 5.6 respectively. This form is chosen so that the drag force is proportional to both the velocity in a given direction and to the length of the drop interface perpendicular to that direction.

5.2.3 Initial Conditions

The relevant variables in the model are (a, b, c), describing the drop shape and $(\dot{a}, \dot{b}, \dot{c})$, describing its velocity. The drop is initially chosen to be a sphere by setting $a_0 = b_0 = c_0 = 1$. To define the initial velocities we choose an initial kinetic energy T_0 corresponding to a Weber number

$$We = \frac{2T_0 a_0}{V_0 \sigma} \tag{5.19}$$

and a value for $\gamma = \dot{b}_0/\dot{a}_0$, the initial degree of lateral asymmetry in the velocities of the drop. The third initial velocity follows automatically from the constraint that the drop is incompressible at t=0.

If a surface is present the drop is assumed to be just touching the surface at $t = 0$ and eq. 5.18 is used for the kinetic energy contribution to the Lagrangian. Note that the constraint on incompressibility leads to an initial velocity that already has components in the transverse directions. Physically this models times after the initial crush phase of impact, which is a short but highly compressible regime, when incompressibility again becomes a good approximation(37).

5.3 Results

5.3.1 Free drop oscillations

We first consider the oscillations of a free drop. The drop can be initialised in an axisymmetric mode by choosing $\gamma = 1$. It then oscillates between an oblate and a prolate spheroid, as shown in fig. 5.1. For small amplitudes the model captures the

Rayleigh result for the period of oscillation, as expected. However, as the Weber number is increased, the drop no longer oscillates harmonically: in particular it oscillates far more quickly out of the oblate ellipsoid shape that it does from the prolate ellipsoid. Moreover, the period increases by approximately an order of magnitude. (It should be noted that the extreme prolate shapes here are unphysical as drop breakup would occur.)

To initialise the drop in the non-axisymmetric mode we choose $\gamma = -1$, this will set the two axis off completely out of phase. In line with the Rayleigh predictions for small amplitudes this mode has the same oscillation time as the symmetric mode. At higher amplitudes a pressure-mediated coupling between modes becomes important and the drop quickly starts to oscillate in a mixed mode shown in fig. 5.2. Fig. 5.3 shows a Poincaré section of this mixed mode case. From this it can be seen that the motion in this mixed mode is chaotic in nature.

5.3.2 Symmetric bouncing

We next consider a drop hitting a surface, choosing $\gamma = 1$ so that the drop preserves circular symmetry during spreading and retraction. Fig. 5.4a shows how the time that the drop is in contact with the surface changes with Weber number and fig. 5.4b indicates the variation of the axis lengths a,b and c with time during the oscillation for two different values of the Weber number. The contact time initially decreases with increasing We, but by $We \sim 10$ it has become virtually independent of the impact velocity. A qualitatively similar behaviour has been observed in experiments(44). However the results are not a quantitative match as the measured contact time is $t = 2.6\tau_e$ whereas the plateau for the model occurs at $t = 1.24\tau_s$ where τ_e and τ_s are the values of $(\rho R^3/\sigma)^{\frac{1}{2}}$ for the experiment and simulation respectively. This is not unexpected because the model neglects many factors present in experiment, for example a surface that is not perfectly hydrophobic, surface drag and that the drop does not remain ellipsoidal but develops a rim.

For our model the magnitude of the plateau in the contact time can be well predicted by considering the high Weber number limit. Assuming that $c/a \ll 1$,

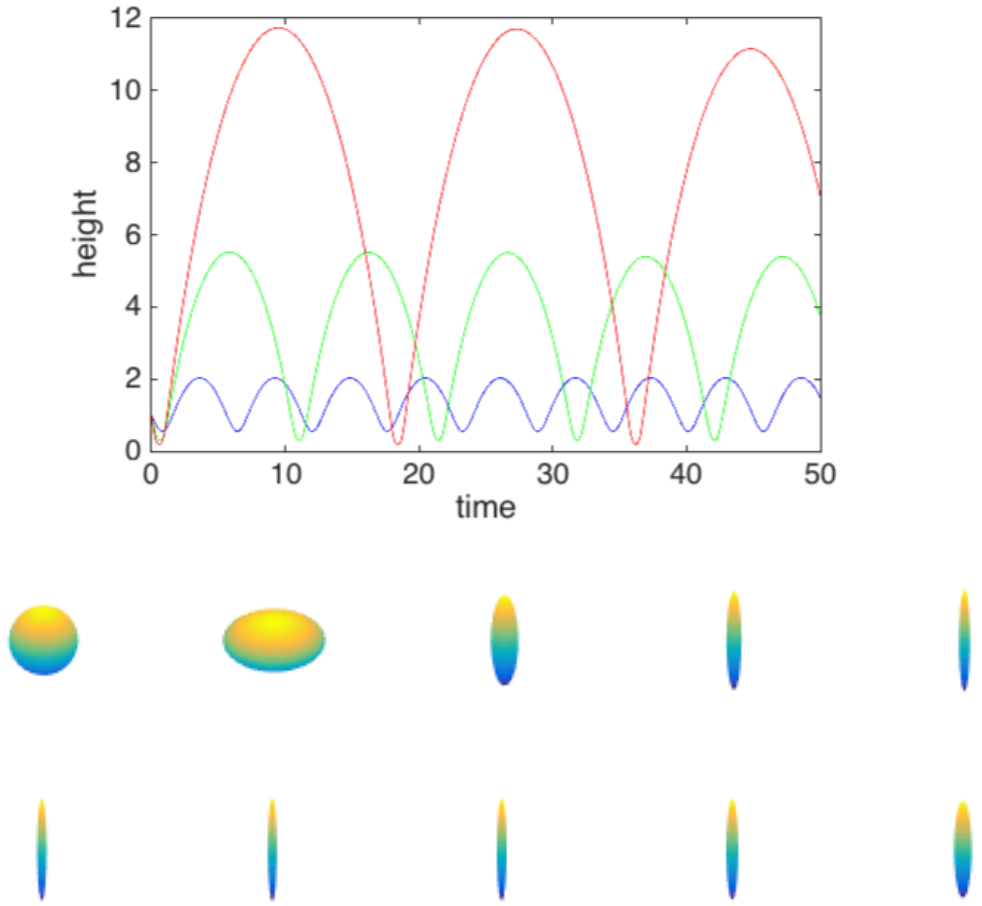

Figure 5.1: Time evolution of the vertical axis c of a free drop oscillating axisymmetrically, about a direction normal to the surface, at $We = 1$ (blue), $We = 5$ (green) and $We = 10$ (red). Snapshots of the drop shape at t=0,1,2 ... for $We = 5$ are shown beneath the graph.

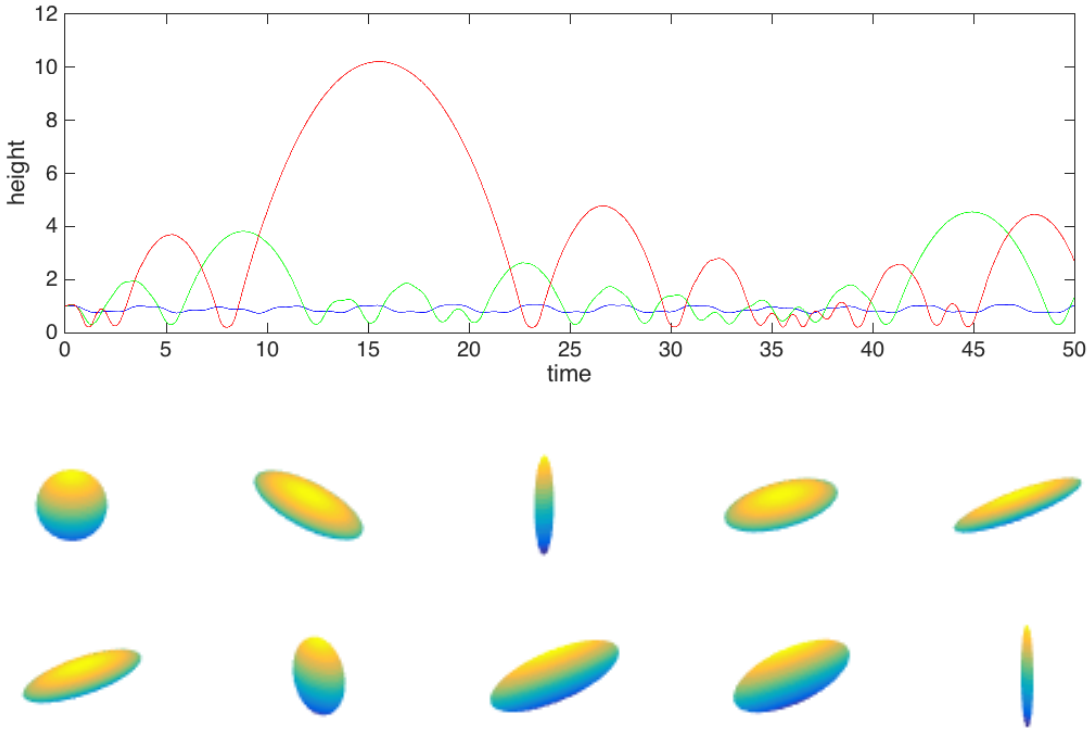

Figure 5.2: Time evolution of the vertical axis c of a free drop oscillating asymmetrically ($\dot{a} \neq \dot{b}$) at $We = 1$ (blue), $We = 5$ (green) and $We = 10$ (red). Snapshots of the drop shape at $t = 0, 5, 10...$ for $We = 5$ are shown beneath the graph.

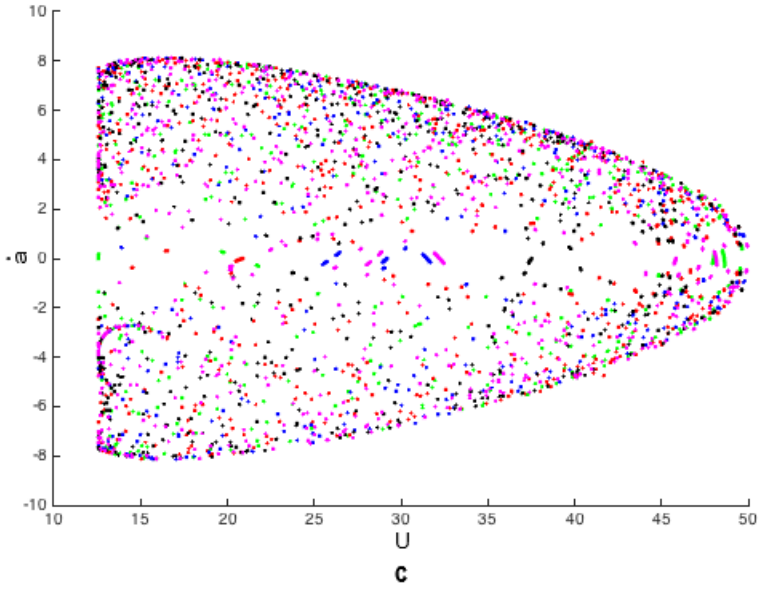

Figure 5.3: Poincaré section for the asymmetric case in the $a = 1$ plane showing $\dot{a}$ against the potential energy U. The colours denote different starting points in the phase space.

eq. 5.5 reduces to

$$\ddot{a} = -\frac{10\pi\sigma a}{\rho V_0}, \tag{5.20}$$

a simple harmonic oscillator with period $2.29\tau_s$. Assuming that the drop is in contact with the surface for half an oscillation, this gives a contact time of $1.15\tau_s$, lower than the measured simulation value, $1.24\tau_s$. The discrepancy is primarily due to lift-off occurring slightly after half an oscillation. Indeed measuring the time to complete half an oscillation, defined as the time taken for the axis a to return to its initial value, gives $1.13\tau_s$, in much better agreement with the simple harmonic motion result.

This argument assumes $c \ll a$ for the majority of the oscillation, which is a reasonable assumption only for very high Weber numbers. Therefore it is surprising that the contact time is already approaching its asymptotic value for $We \sim 5$. To understand this further we use the assumptions of incompressibility and symmetry to rewrite the Lagrangian (5.4) in terms of a and $\dot{a}$:

$$\mathcal{L} = \frac{\rho V_0 \dot{a}^2}{5}\left(1 + \frac{12}{a^6}\right) - 2a^2\sigma\left(1 + \frac{2}{a^{4.8}}\right)^{\frac{1}{1.6}}. \tag{5.21}$$

Guided by this formula, we model the expansion as comprising an initial stage defined by $a < a_c$, of duration t_1, which is dominated by inertial-driven spreading, followed by a second stage, $a > a_c$ of duration t_2, where surface tension provides the forcing and the simple harmonic equation of motion (5.20) holds. A convenient choice for a_c after which the surface tension is dominant is $a_c = 2$ as by this point the second term in each bracket is small compared to unity. Recall that, as the expansion and retraction are symmetric in time, we may just consider spreading to the maximum drop extension and then double the result to give the time for half an oscillation.

Assuming that the spreading is inertially dominated and that the surface tension

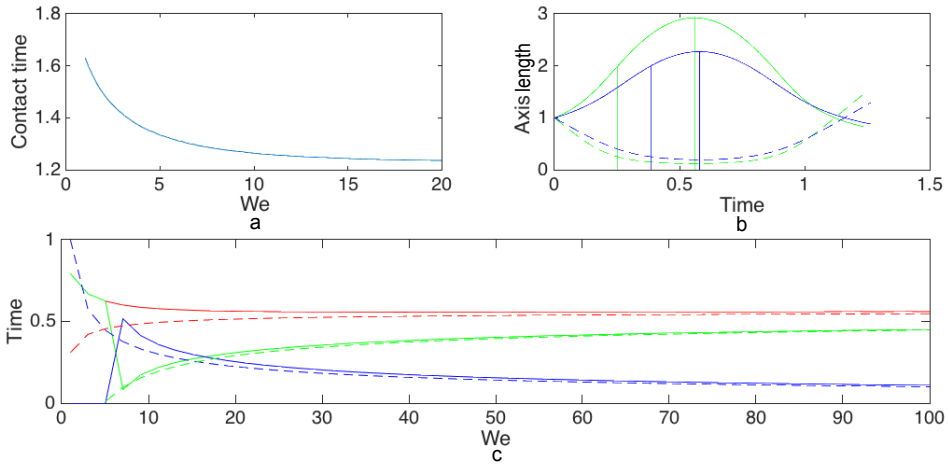

Figure 5.4: **a** Variation of the contact time with Weber number for axisymmetric impacts. **b** Axis lengths, c: dotted, $a = b$ full lines, against time for $We = 10$ (blue) and $We = 20$ (green). The vertical lines show t_1 and t_2 for each We. **c** A comparison of t_1 and t_2 for the numerical (solid lines) and analytical (dashed lines) results against Weber number with t_1 (blue), t_2 (green), $t_1 + t_2$ (red).

is negligible gives

$$t_1 = \frac{a_c - a_0}{u_0} = \left(\frac{\rho a_0}{2\sigma We}\right)^{\frac{1}{2}} \tag{5.22}$$

where $u_0 = (\sigma We/\rho a_0)^{\frac{1}{2}}$ is the characteristic velocity of the system at early times. From eq. 5.20

$$t_2 = \frac{1}{\omega}\left(\frac{\pi}{2} - \frac{a_c}{a_m}\right) = \frac{\pi}{2\omega} - 2\left(\frac{\rho a_0}{5\sigma We}\right)^{\frac{1}{2}} \tag{5.23}$$

where ω is the angular frequency of the oscillator and $a_m \approx (T_0/2\pi\sigma)^{\frac{1}{2}}$ is the maximum extension of the drop. The sum $t_1 + t_2$ is only weakly influenced by the initial kinetic energy as the two terms dependent on the Weber number in eqs. 5.22 and 5.23 almost cancel justifying why the plateau in contact time is reached quickly with increasing We. Fig. 5.4c shows how the approximations for t_1 and t_2 compare to the times measured in the simulations.

The effect on the contact time of adding a contact line drag, $F_a = F_b = F$ is shown in fig. 5.5a. In fig. 5.5b we plot the variation of the axes lengths with time for different Weber numbers, showing that the damping tends to decrease the spreading time and increase the retraction time. The interplay of these two effects can either

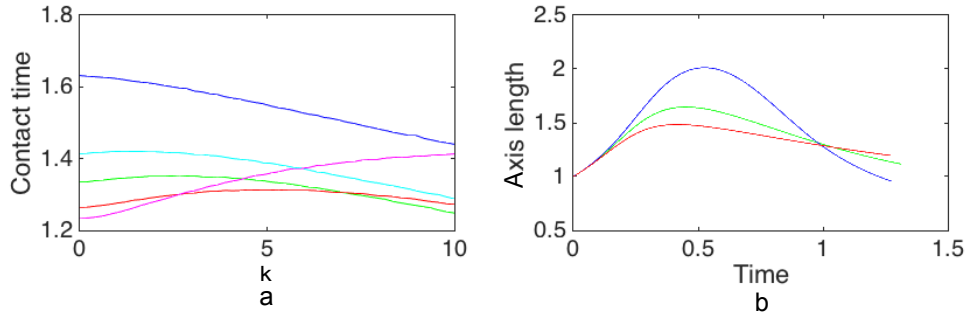

Figure 5.5: **a** Variation of the contact time with drag, k, for different Weber numbers for $We = 1$ (blue), $We = 3$ (cyan), $We = 5$ (green), $We = 10$ (red) and $We = 20$ (magenta). **b** Axis length variation with time at $We = 10$ for $k = 1$ (blue), $k = 5$ (green) and $k = 10$ (red).

increase or decrease the contact time.

5.3.3 Asymmetric bouncing

Several authors have recently shown that the drop-substrate contact time is reduced if the bouncing is not axisymmetric(45; 97; 46; 52). There are several ways of introducing a lateral asymmetry into our model; different initial velocities along x and y, an asymmetric initial drop shape $a_0 \neq b_0$, and anisotropic surface drag.

5.3.3.1 Anisotropic momentum

We impose an initial lateral asymmetry in momentum by taking γ greater than unity, corresponding to $\dot{b}_0 > \dot{a}_0$. This is a similar situation to the lattice-Boltzmann simulations shown in sec. 3.3.1. Fig. 5.6a shows that the contact time decreases with increasing asymmetry, and that the effect is more pronounced at larger We. For very low We the contact time does not decrease this is due to the fact that the drop does not have enough energy to bounce.

The decrease in contact time occurs because the initial anisotropy in velocity means that b expands faster than a (Fig. 5.6b). This leads to a surface tension force on a that is larger than on b, because a small change in a has a larger effect on the total area of the drop (Fig. 5.6c). Thus a reaches a maximum, and then starts to retract while b is still growing. Once a starts to retract the incompressibility condition leads to a positive feedback which tends to slow down the oscillation of b. This is most clearly seen in Fig. 5.6b. The continued anisotropy of the drop

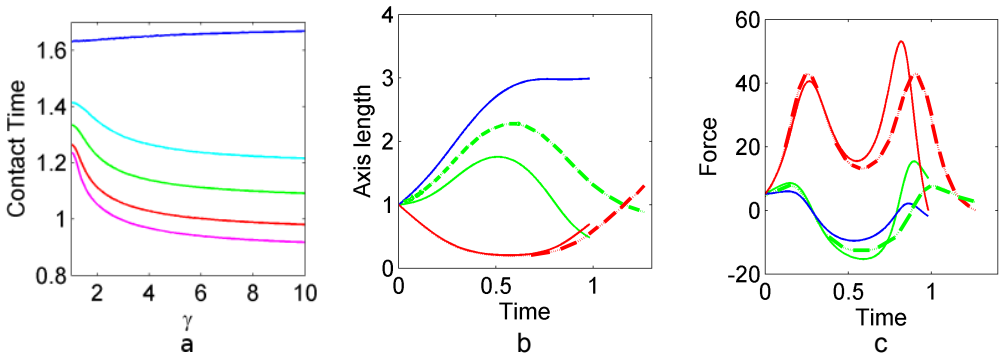

Figure 5.6: **a** Effect of varying γ on the contact time for $We = 1$ (blue), $We = 3$ (cyan), $We = 5$ (green), $We = 10$ (red) and $We = 20$ (magenta). **b** Variation in axis length a(green), b(blue) and c(red) with time for $We = 10$, solid lines are the asymmetric case, $\gamma = 10$, with dotted lines the symmetric case for comparison. **c** Variation in the force upon axes a(green), b(blue) and c(red) with time for $We = 10$, solid lines are the asymmetric case, $\gamma = 10$, with dotted lines the symmetric case for comparison.

keeps the force on a large compared to that on b. Hence a retracts more quickly and drives the bouncing at a later time as the b-axis retracts. As the asymmetry is increased further however the rate of decrease does drop.

There are two forces acting on each axis as can be seen from eq. 5.5 and fig. 5.6c. The first of these is a pressure force which comes directly from the incompressibility condition and can basically be understood to be maintaining the volume of the drop as a constant. The second is a surface tension force which acts when the drop begins to deform away from a spherical shape. The force upon axis a in fig. 5.6c is initially pressure dominated and pushes the axis outwards to compensate for the incoming c axis. In the middle section of the collision the surface tension force dominates and the force upon axis a becomes negative and crucially of a greater magnitude than in the symmetric case. This greater retraction force is due to the increased size of the b axis during the retraction.

Fig. 5.6a indicates that for $We = 1$ there is a small increase in contact time. This occurs because there is not sufficient energy for lift-off upon the initial retraction of the the a-axis. The drop bounces at a later time as the b-axis retracts.

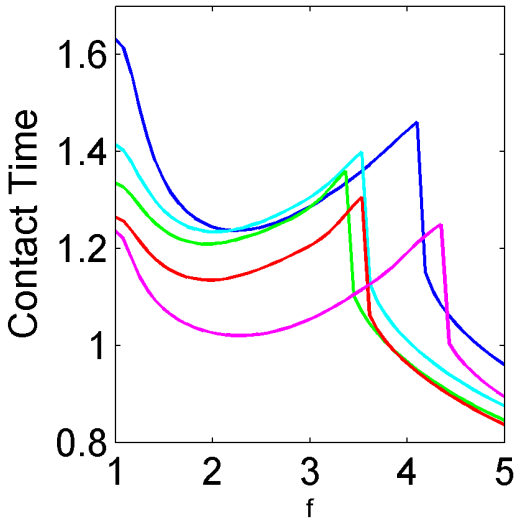

Figure 5.7: Effect of varying f on the contact time for $We = 1$ (blue), $We = 3$ (cyan), $We = 5$ (green), $We = 10$ (red) and $We = 20$ (magenta). **b** Variation in axis length a(green), b(blue) and c(red) with time for $We = 10$, solid lines are the asymmetric case, $f = 2$, with dotted lines the symmetric case for comparison.

5.3.3.2 Anisotropic shape

The impact of drops with asymmetric initial shapes also leads to changes in contact time. The drops were initialised with a fixed initial volume $V_0 = 4\pi/3$ and $c_0 = 1$, and the asymmetry was controlled by $f = b_0/a_0$.

Fig. 5.7a shows that there is a non-monotonic variation of the contact time with f. For $f <\sim 4$, to the left of the cusp, the b (initially larger) axis drives the lift-off, whereas for higher f the a-axis retraction is responsible for the bouncing. For the larger anisotropies the bouncing mechanism is similar to that for the case where the velocities are initially anisotropic. The surface tension force on a is larger and therefore it oscillates more quickly. Once it is retracting the incompressibility condition leads to a coupling which further slows the oscillation of the b axis and in turn promotes anisotropy and fast a-retraction leading to quicker bouncing.

For smaller anisotropy the two directions are more balanced. a still tends to oscillate more quickly, but also extends further before retracting. Hence the b axis has time to contracts first and drives the bouncing. The shape anisotropy upon lift-off, and hence the reduction in contact time, is small.

These two regimes are compared in fig. 5.8 and fig. 5.9. Fig. 5.8 shows the axes evolution and the forces upon the axes for $f = 2$, $We = 10$. In this regime the

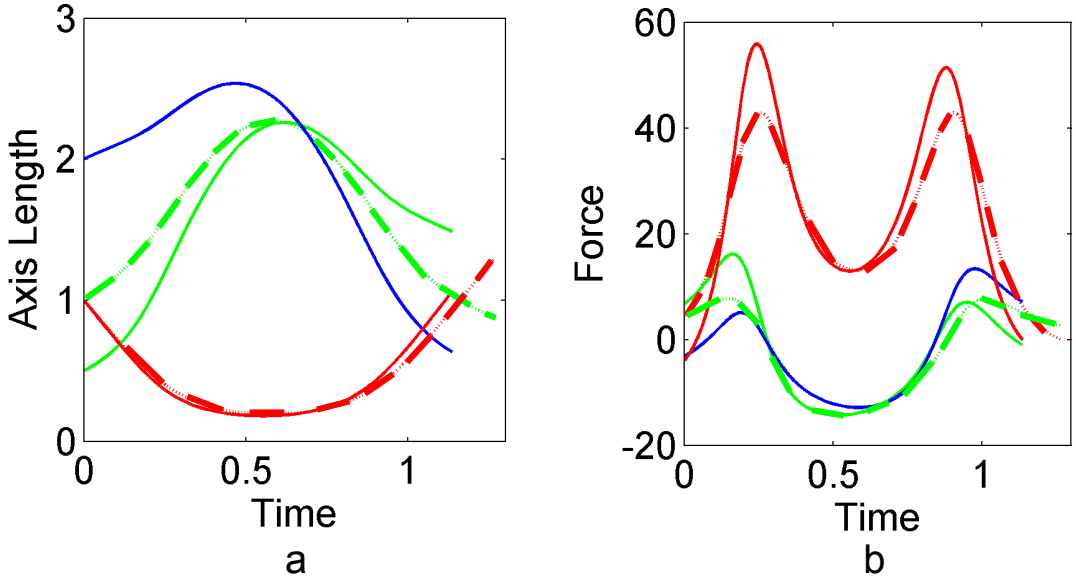

Figure 5.8: **a** Variation in the axis length a(green), b(blue) and c(red) with time for $We = 10$, solid lines are the asymmetric case, $f = 2$, with dotted lines the symmetric case for comparison. **b** Variation in the force upon axes a(green), b(blue) and c(red) with time for $We = 10$, solid lines are the asymmetric case, $f = 2$, with dotted lines the symmetric case for comparison.

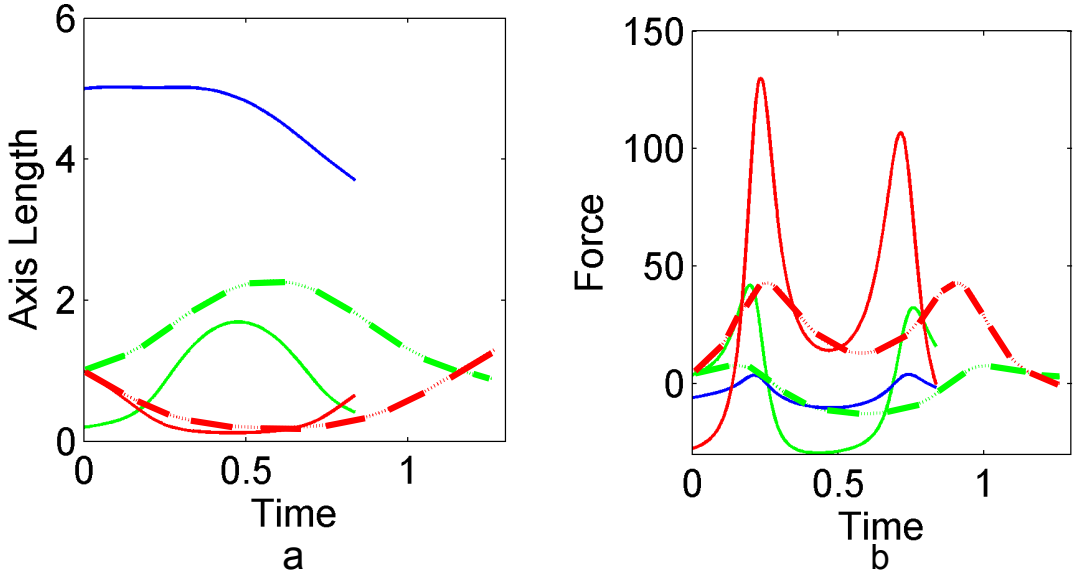

Figure 5.9: **a** Variation in the axis length a(green), b(blue) and c(red) with time for $We = 10$, solid lines are the asymmetric case, $f = 5$, with dotted lines the symmetric case for comparison. **b**Variation in the force upon axes a(green), b(blue) and c(red) with time for $We = 10$, solid lines are the asymmetric case, $f = 5$, with dotted lines the symmetric case for comparison.

lift-off is driven by the initially larger axis b. This can be seen clearly in fig. 5.8a in which the b axis, after a slight increase, quickly begins to retract. The minimum in the contact time in this first regime can be explained by noting that initially the increasing asymmetry leads to the b axis starting to retract sooner. Beyond the minima however, as the size of b is further increased, the greater distance the b axis has to retract begins to cause an increase in the contact time.

By contrast for $f \gtrsim 3$ the lift-off is driven by the retraction of the initially smaller a axis, causing the sudden change in the contact time. Fig. 5.9 shows how the axes and the forces upon the axes change for $f = 5$, $We = 10$. From looking at fig. 5.9a it can clearly be seen that now the b axis remains large throughout the impact leading to a very quick expansion and retraction of axis a and thus a low contact time. This can also be seen by examining the forces in fig. 5.9b in which the retraction force upon axis a can be seen to be large throughout.

5.3.3.3 Anisotropic surface drag

Finally we consider the effect of anisotropic contact line drag, F_a, with $F_b = 0$. Fig. 5.10 shows that here too there is a non-monotonic variation of contact time with We. For low k_a the bouncing mechanism is similar to that already described for anisotropic velocities, with the additional complication that for higher drag the slowing of the retraction due to the damping starts to have an effect. For higher k_a there is a different regime in which the contact time is greater than for zero drag. This occurs when the damped a-axis retracts with insufficient energy to drive lift-off.

5.4 Summary

We have defined a simple Lagrangian model which is able to reproduce many of the features of the impact of drops on solid surfaces. The model extends the classic normal mode analysis of Rayleigh beyond the linear regime. Our model qualitatively matches experiments on drop impact in that it shows a contact time that decreases to a plateau with increasing We. The plateau occurs because the retraction is

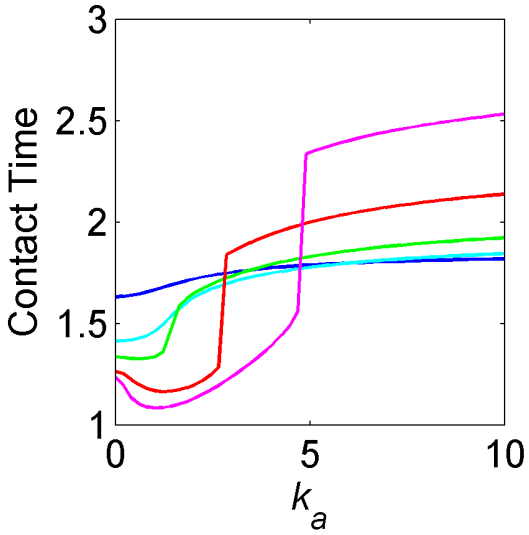

Figure 5.10: Effect of varying k_a on the contact time for $We = 1$ (blue), $We = 3$ (cyan), $We = 5$ (green), $We = 10$ (red) and $We = 20$ (magenta).

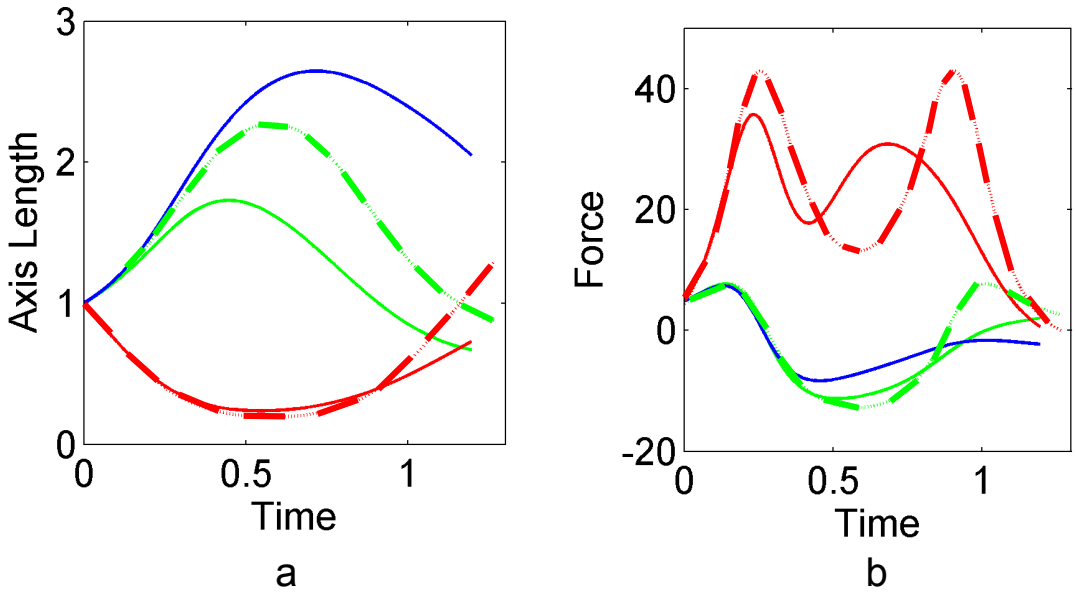

Figure 5.11: **a** Variation in axis length a(green), b(blue) and c(red) with time for $We = 10$, solid lines are the asymmetric case, $k_a = 2$ with dotted lines the symmetric case for comparison.**b** Variation in the force upon axes a(green), b(blue) and c(red) with time for $We = 10$, solid lines are the asymmetric case, $k_a = 2$, with dotted lines the symmetric case for comparison.

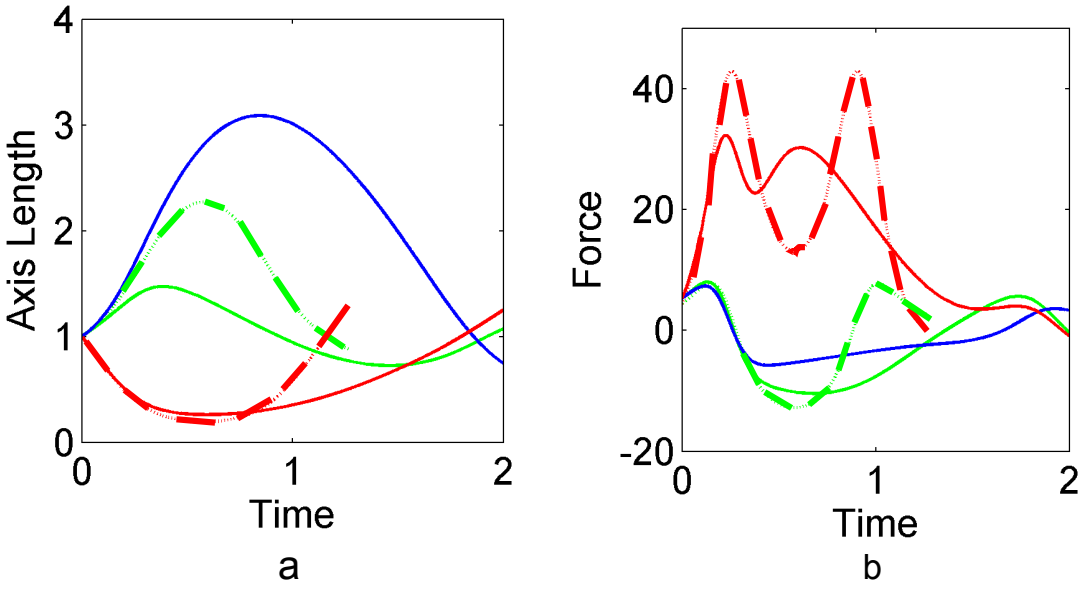

Figure 5.12: **a** Variation in axis length a(green), b(blue) and c(red) with time for $We = 10$, solid lines are the asymmetric case, $k_a = 5$, with dotted lines the symmetric case for comparison. **b**Variation in the force upon axes a(green), b(blue) and c(red) with time for $We = 10$, solid lines are the asymmetric case, $k_a = 5$, with dotted lines the symmetric case for comparison.

predominantly a simple harmonic motion, driven by surface tension. Quantitative difference between experiment and model are to be expected, because physical drops develop a rim upon bouncing, and because of viscous losses.

We use the model to describe asymmetric bouncing, due to an asymmetric initial velocity, initial shape or contact line drag. The usual effect of anisotropy is to cause a reduction in contact time. This occurs because once the drop has an elliptical footprint the surface tension force acting on the longer sides (or, equivalently, the direction perpendicular to the smaller initial velocity) is greater. Therefore the shorter axis retracts faster and, due to the incompressibility constraints, pumps fluid along the more extended droplet axis. This leads to a positive feedback, allowing the drop to jump in an elongated configuration, and more quickly.

CHAPTER 6

Bouncing of composite drops

6.1 Introduction

In this thesis so far we have concentrated on the impact of drops upon complex surfaces. We shall now consider the impact of composite drops, made up of a liquid drop and an embedded air bubble, onto flat surfaces. One of the key points about this system is that the presence of the air bubble within the drop creates a density interface, at the bottom of the bubble, which is both of the opposite curvature to the top of the drop and closer to the solid surface at the point of impact.

Antkowiak *et al.*(99; 58) looked at what happened when a test tube containing liquid impacts upon a solid surface. They found that the impact creates a pressure wave which travels up the test tube before reaching the air liquid interface. From this point they found that the form of the liquid air interface had a large effect upon the subsequent dynamics. If the sides of the test tube had a contact angle of 90 degrees, producing a flat interface, then the interface was found to move upwards slightly as a whole when the pressure wave arrived. If, however, the sides of the test tube are hydrophilic the interface is not flat but curved upwards in a concave shape. When the pressure wave reached this curved meniscus the requirement that the pressure is constant on the water surface leads to a bunching of the pressure isolines and therefore a greater pressure gradient.

Further work which has been done to explore the same phenomenon is by Tagawa *et al.*(59) and Peters *et al.*(60). In these studies a laser is used to evaporate a small volume from within the liquid bulk. This creates a high energy pressure pulse which then travels towards a curved density interface as in the earlier studies. In this case the curved interface concentrates the energy from the high energy laser pulse which leads to supersonic jets being formed.

Previous studies have also looked at the effect that entrenched air bubbles have in the context of cavity collapse under the influence of pressure waves(100; 101). This work found that shock waves caused cavities within the bulk to collapse often producing micro-jets as they did so. These studies were motivated by pressure driven explosion initiation. In this case the pressure concentrating effects of the cavities were found to lead to such initiations at lower pressures than theoretically predicted for bulk quantity of the pure substance.

There have also been studies of bubbles on a free surface bursting in the absence of a pressure wave. An example is the work of Duchemin *et al.*(62) who found that bubbles bursting on the surface of a liquid can lead to jet formation even in the absence of any impact or excitation.

In this chapter we look at simulations of the impact of liquid drops which have air bubbles captured within them. This set-up is similar to that in the test tube experiments(99) as the impact creates a pressure wave which travels through the liquid drop eventually reaching the air bubble which provides a curved interface. Our results are compared to a set of experiments, carried out by Professor Castrejon-Pita (Oxford Engineering) which are used to show the validity of the simulations.

We first look at how the simulations compare to some example experiments and at how the pressure varies early in the simulation. We then vary the bubble size, position and shape and the impact velocity of the drop and look at how these effect the maximum jet velocity. With the exception of impact velocity, which is found to have a simple linear effect, the position of the bubble is found to be the most important variable. Both changing the distance between the bubble and the top of the drop and the distance between the bubble and the bottom of the drop are

Quantity	Value (simulation units)
Surface tension	0.0083
Liquid dynamic viscosity	0.0084
Gas dynamic viscosity	0.00019
Liquid density	1
Gas density	0.0012
Interface width	5
Contact angle	60
Initial velocity	0.1
Drop radius R_d	50
Mobility	0.94
Gravitational constant	0

Table 6.1: Parameters used in the simulations.

found to have a dramatic effect on the impact process.

6.1.1 Simulation approach

The simulations in this chapter were undertaken using the lattice Boltzmann code described in chapter 2. The substrate in the system is a flat surface. Part of the drop volume is replaced with an air bubble whose size and position can be controlled. The impact is then observed and the maximum velocity of any jets created is measured. The velocity of the jet is measured by averaging the velocity of all nodes in the part of the diffuse interface which corresponds to the top of the jet.

The parameters used in these simulations are shown in table 6.1. The volume of liquid is kept constant throughout and is equivalent to the volume of a drop without an air bubble of the radius given in the table. This radius is also used to compute the *We* and *Oh* numbers.

The simulation box was $200 \times 200 \times 200$ nodes in size and as the simulations have two planes of mirror symmetry, reflection boundary conditions were used at the edges of the box.

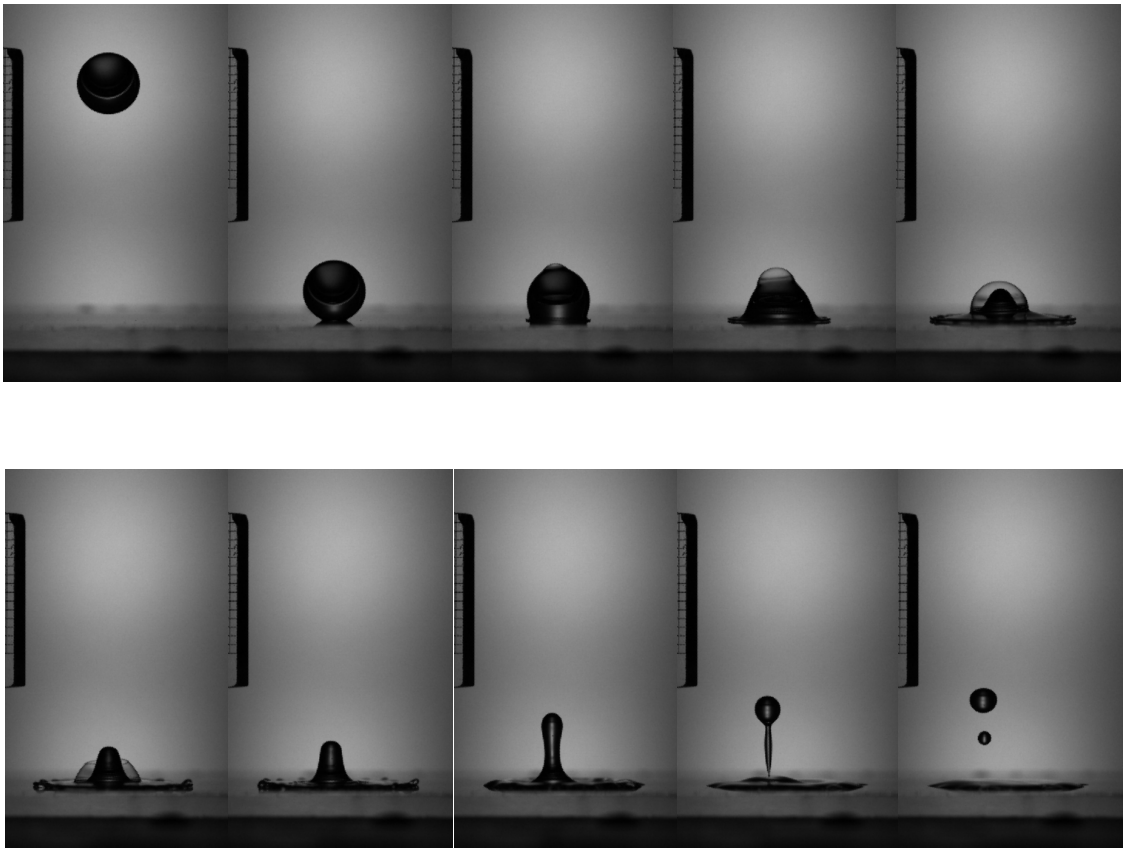

Figure 6.1: Snapshots of a liquid drop with an embedded air bubble colliding with a surface at $We = 134$ and $Oh = 0.047$. Courtesy of Alfonso Castrejon-Pita

6.2 Results

6.2.1 Impacts of a composite drop

Fig. 6.1 shows snapshots of an experiment in which a liquid drop containing a bubble of lower density air impacts upon a flat surface. The composite drop is created by a coaxial nozzle and falls onto the flat surface from a set height. This collision is at $We = 134$ and $Oh = 0.047$. Looking at the first two images it can be seen that the air bubble maintains its position in the drop as it drops onto the surface. As the drop impacts the surface a jet of liquid is formed beneath the bubble which then travels up through the bubble and exits, from the top of the bubble, bursting it as it does so. This jet then eventually splits into two droplets one formed from the head of the jet and the other from its body, which together contain a considerable portion of the starting drop's mass.

Fig. 6.2 shows simulation results of the collision of a drop containing an air

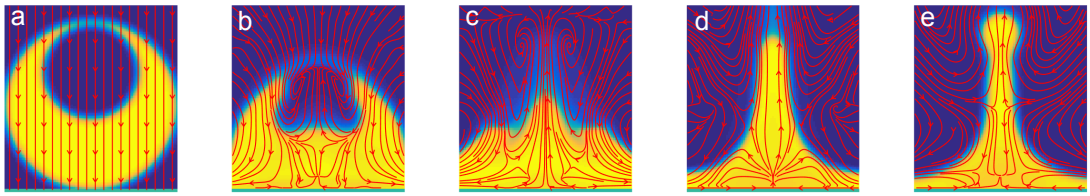

Figure 6.2: Central cuts showing a collision of a composite drop with a ratio of the radius of the air bubble to the liquid drop $R_b/R_d = 0.56$ at $We = 60$ and $Oh = 0.013$. The time is non dimensionalised by the inertial capillary time τ. The red lines show the flow streamlines at each time.

bubble with a flat surface for $We = 60$ and $Oh = 0.013$. The times, normalised by the inertial capillary time, are given below the figure. This displays the same dynamics as the experimental results: A jet is formed beneath the bubble, then travels upwards and exits the drop. The jet then splits into two ejecta droplets, one of which is formed from the head of the jet and the other from its body, at later times (not shown), as in the experiments.

This phenomena can be explained by noting that early on during the collision a high pressure layer is formed near the surface which then propagates upwards. When this pressure wave reaches the lower interface of the embedded air bubble it causes a jet to form. The jet travels upwards as the rest of the drop continues to spread out on the surface. It eventually splits into two ejecta droplets. The rest of the drop then continues the collision but with a noticeably lessened speed and chance of lift-off compared to a similar drop without an air bubble as much of the energy of the collision has been carried away by the jet.

The red lines in fig. 6.2 show the streamlines in the drop during this process. Initially the drop and the bubble are travelling straight down. The drop then impacts the surface. As fig. 6.2b and c show, the edges of the drop begin to spread as usual. However in the centre of the drop a vortex ring is formed as the jet is forced upwards at the same time as the rim is forced outwards. This drives the liquid from the upward reaching arms down and then up towards the centre helping to form the jet.

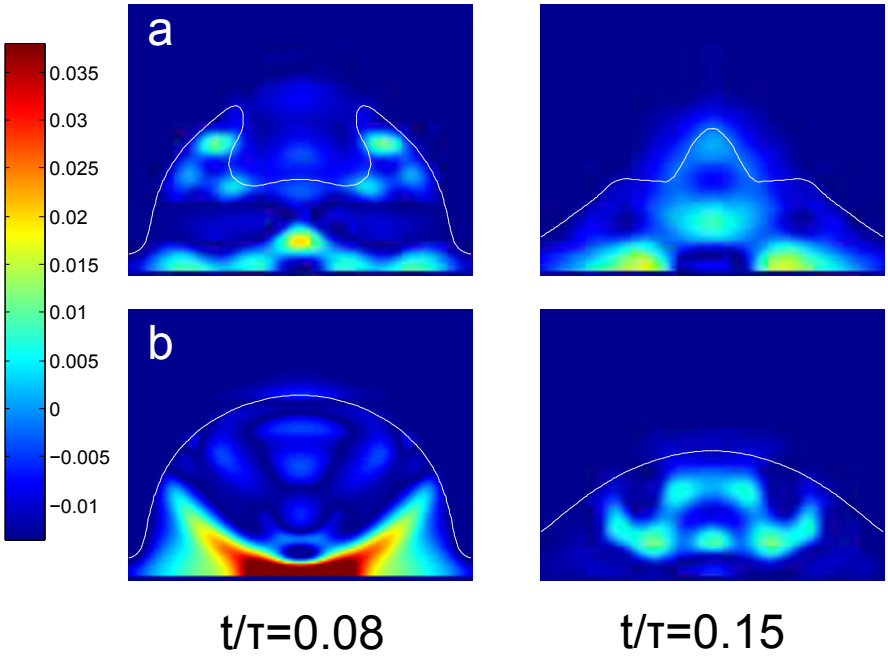

Figure 6.3: A comparison of the pressure at intermediate times for **a**, a drop containing an air bubble and **b**, a drop containing no air bubble. The times correspond to the second and third panels of fig. 6.2. Both cases were at $We = 60$ and $Oh = 0.013$. At a time of t/τ=0.08 a high pressure region near the substrate can be seen in both cases. At t/τ=0.15, in the second image, the high pressure region has pushed out forming an outward spreading rim and, in the case with the air bubble, an upwards moving jet.

6.2.2 Pressure evolution

The top row of fig. 6.3 shows the pressure at two separate shapes of this collision. In the first image, at $t/\tau = 0.08$, a high pressure region can be seen forming adjacent to the substrate. By a time of $t/\tau = 0.15$, in the second image, this high pressure region has started to lead to the formation of an outward spreading rim as well as an upward moving jet.

For comparison the bottom row of fig. 6.3 shows an identical collision but with the air bubble removed. A high pressure layer can be seen next to the substrate. In this case , however, the outwards forcing can more clearly be seen.

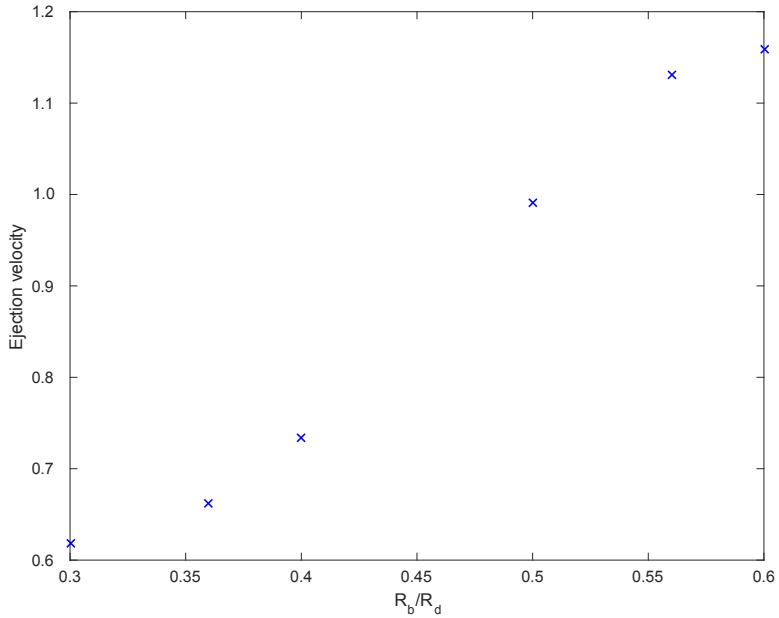

Figure 6.4: Variation in the jet velocity against the ratio of the bubble radius R_b and the drop radius R_d, at $We = 60$ and $Oh = 0.013$. The velocity on the y axis is non-dimensionalised by the initial impact velocity of the composite drop.

6.2.3 Varying bubble size

One parameter which can be varied is the volume of the bubble compared to the volume of the liquid. Several simulations were performed varying the size of the bubble whilst keeping the volume of the liquid drop constant. The upper interface of the bubble was kept a set distance from the top of the drop, so this not only changes the curvature of the air bubble but also the distance between the air bubble and the bottom of the drop.

The maximal jet velocity is used as a measure to study the effect of this change. More precisely this is taken as the maximal velocity reached by the topmost jet interface. Fig. 6.4 shows how the velocity of the jet varies with the size of the bubble. The trend is that the smaller the bubble the slower the ejected jet. Any focusing due to the curvature would be expected to increase as the bubble gets smaller. Therefore it is surmised that it may be the change in the position of the bottom interface of the bubble with respect to the surface that is the cause of this decrease. Another factor to consider however is the extra surface tension energy

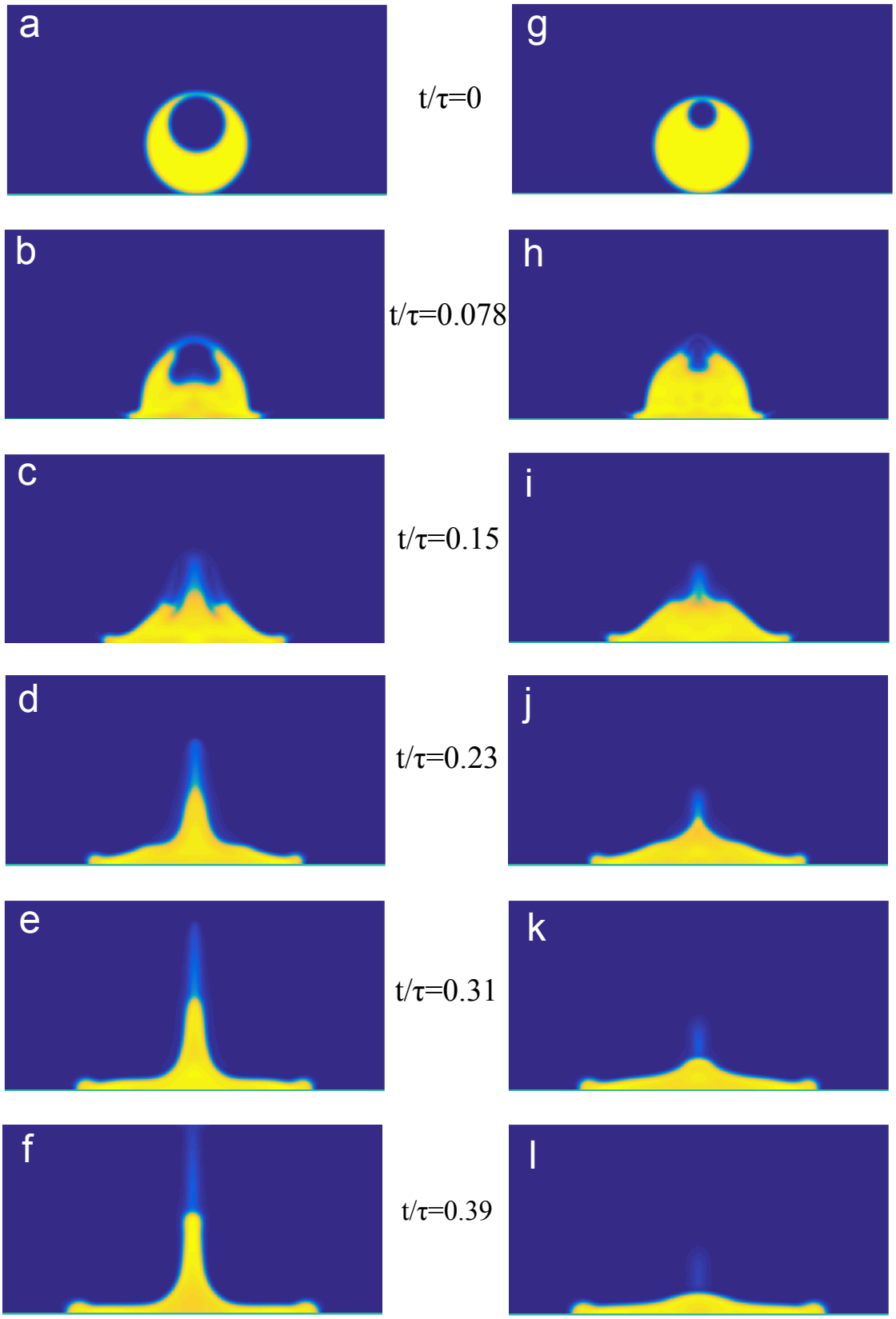

Figure 6.5: A comparison of two different impacts as the size of the air bubble is varied at $We = 60$ and $Oh = 0.013$. The ratios of drop to bubble size are $R_b/R_d = 0.6$ in the left column and $R_b/R_d = 0.3$ in the right column. The time on the y axis is non-dimensionalised by the inertial capillary time $\tau = \sqrt{\frac{\rho R_d^3}{\sigma}}$

which the system starts with when the volume of the air bubble is increased.

Fig. 6.5 shows juxtaposed snapshots corresponding to two extreme values of fig. 6.4, for $R_b/R = 0.3$ on the top row and $R_b/R = 0.6$ on the bottom row. Here is can be seen that as the bubble size is decreased the jet starts to fail to form at all.

6.2.4 Varying the drop position

We ran some simulations to check the effect of changing the bubble position. Fig. 6.6 shows two sets of snapshots for different vertical positions of the centre of the bubble. The top row of snapshots shows a collision in which the offset of the top of the bubble from the top of the drop is $0.14R_b$ and the bottom row shows a collision where the offset is $0.04R_b$. Despite this being a very small difference in the vertical position of the drop there is a large effect on the dynamics.

Firstly the width of the jet is greatly increased. This can be explained by looking more closely at the upwards pointing wings which form on the sides of the drop. In the case where the air bubble is lower within the drop these wings are bigger, and rather than merging with the bulk of the drop and then being driven up into the jet (see fig. 6.2), they instead merge with the jet itself fig. 6.6c-d. This leads to a much thicker jet which reaches a lesser height as the greater inertial mass slows it down.

This is shown in fig. 6.7 where we plot the jet velocity as a function of the distance between the bubble and the top of the drop. It might initially be surmised that this is due to the jet having trouble punching through the thicker layer above it. However looking at fig. 6.6, it is apparent that the top layer tends to rupture before the jet reaches it, and the reason for the slowing is primarily the merging of the wings with the jet. These simulations are however unable to tell us about the effect of changing the bubble position relative to the bottom of the drop as the physics is dominated by the increase in the amount of liquid above the bubble.

6.2.5 Varying the Weber number

The effect of varying the impact speed and therefore the Weber number is also potentially of interest. To study this the drop and bubble size were kept the

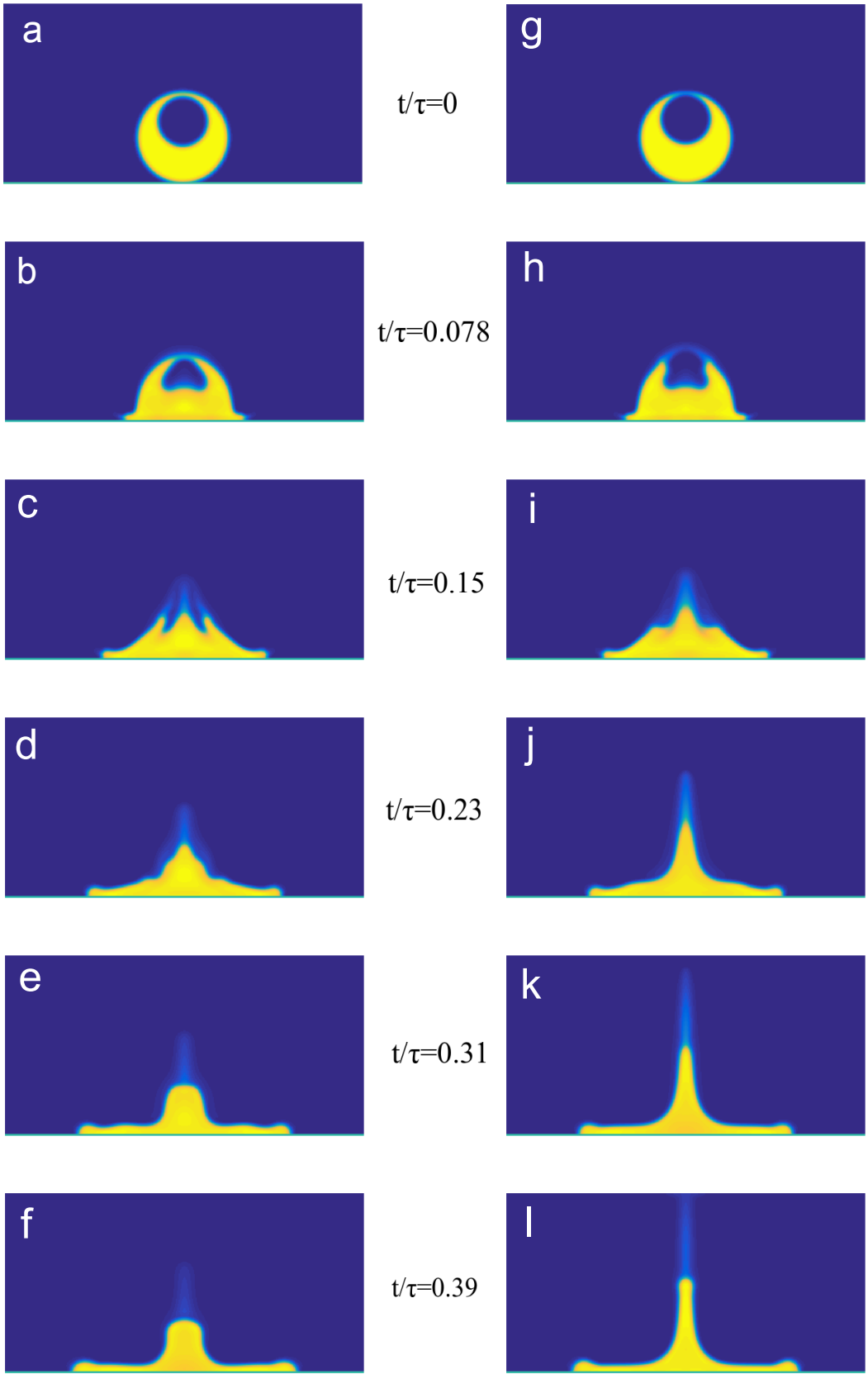

Figure 6.6: A comparison of two different impacts as the position of the air bubble is varied vertically within the drop. Both simulations are at $R_b/R_d = 0.56$, $We = 60$ and $Oh = 0.013$. The left column shows the impact of a composite drop where the air bubble is offset from the top of the drop by $0.14R_b$. The right column shows the impact of a composite drop with an offset of $0.04R_b$.

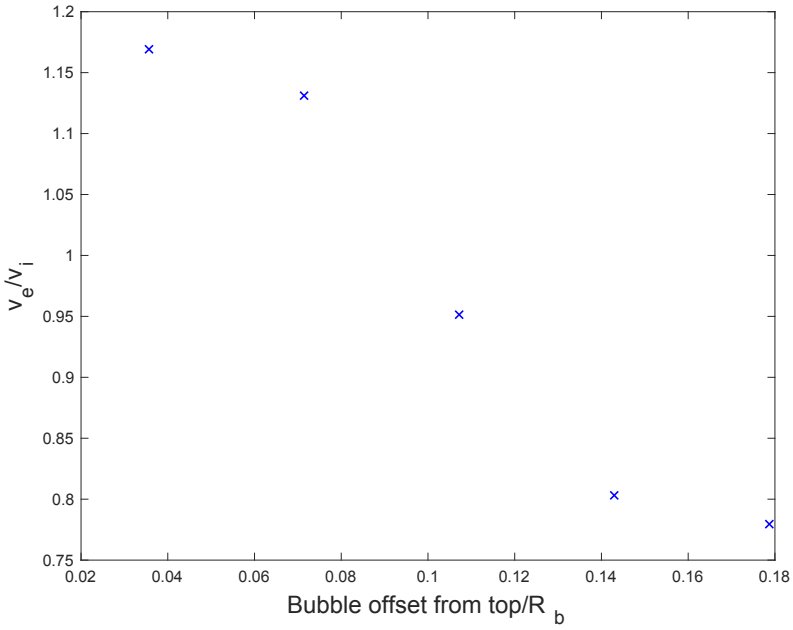

Figure 6.7: Variation in the jet velocity as the vertical position of the bubble within the liquid drop is varied, at $We = 60$ and $Oh = 0.013$. The x axis shows the distance between the top of the bubble and the drop non-dimensionalised by the radius of the air bubble. The y axis shows the jet velocity non-dimensionalised by the initial impact velocity of the composite drop.

same and the initial impact speed was varied. Fig. 6.8 shows how the jet velocity varies with the initial impact velocity. Unsurprisingly the jet velocity increases as the initial impact velocity is increased. With the exception of the lowest velocity simulated the relationship is roughly linear, with the jet velocity increasing in step with the initial impact velocity.

The reason for the lowest impact velocities not following the pattern can be seen by looking at fig. 6.9. This shows an impact for an initial velocity of 0.04 in the top row and an impact with an initial velocity of 0.09, in simulation units, in the bottom row. The top row shows an evolution similar to that for a bubble bursting in a stationary drop which can be seen to be very different to that for larger impact velocities. It therefore appears that for low impact velocities the surface tension starts playing a role rather than the dynamics being inertially driven.

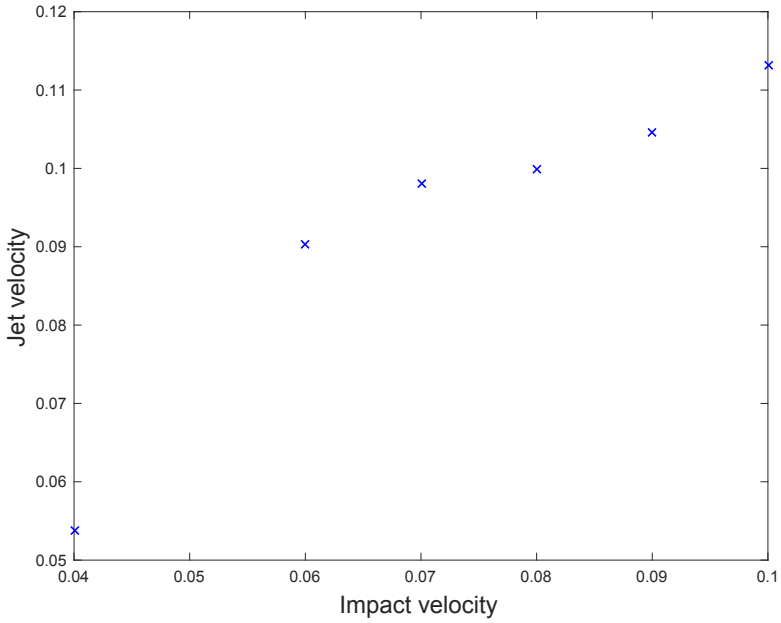

Figure 6.8: Variation in the jet velocity against the initial impact velocity, at $Oh = 0.013$.

6.2.6 Varying the bubble shape

Looking closely at the early images in fig. 6.1 it can be seen that the air bubble does not look completely spherical but instead conforms to the top surface of the liquid drop thus becoming slightly deformed. To study this deviation from a spherical shape air bubbles which were ellipsoidal were considered. To do this the height of the air bubble was kept constant whilst its width was varied. We define the aspect ratio of the bubble as its height relative to its width. The liquid volume was also kept constant so that the Weber number did not change. This set up may also provide some insight into the effect that the curvature of the air bubble has upon the dynamics as the curvature at the bottom of the air bubble will increase as the ellipsoidal shape is narrowed.

Figure 6.10 plots the maximum velocity of the jet as the aspect ratio of the air bubble is varied. The jet velocity increases steeply with aspect ratio until an aspect ratio of 1.1 and then reaches a plateau. There are two possible reasons for the increase. The first of these is that, as the bubble narrows, the curvature at the bottom of the bubble increases leading to a more concentrated pressure and

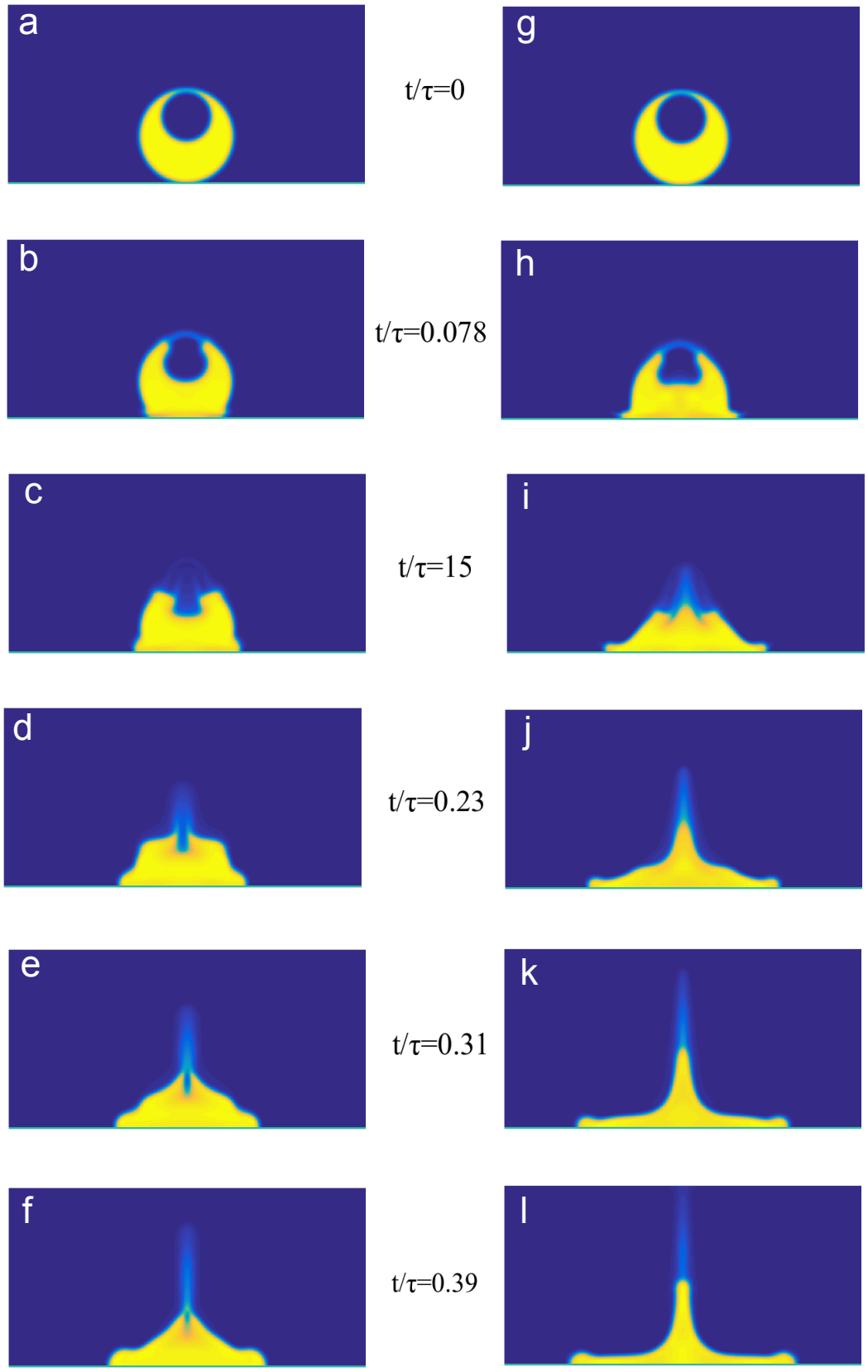

Figure 6.9: A comparison of two different impacts as the impact velocity is varied at $Oh = 0.013$ and $R_b/R_d = 0.56$. The left column shows the impact of a composite drop with an initial velocity of 0.04. The right column shows the impact of a composite drop with an initial impact velocity of 0.09.

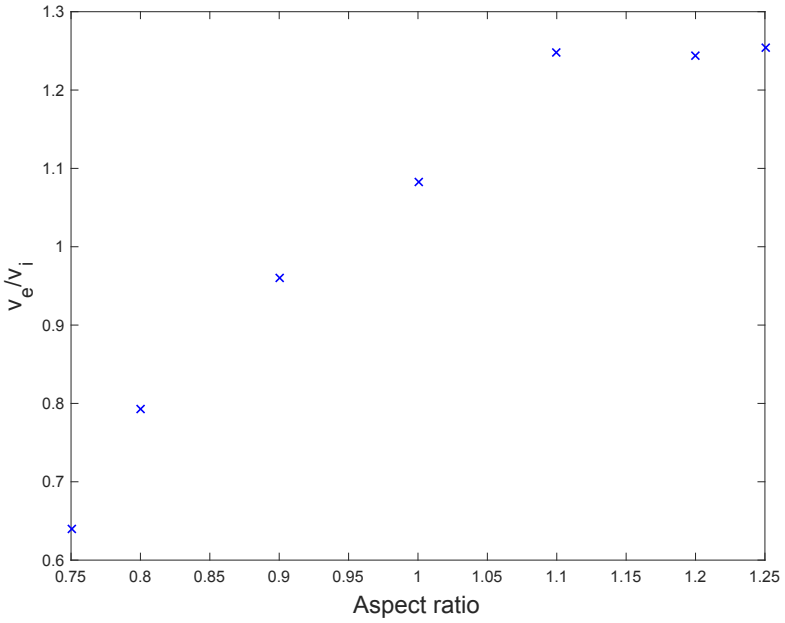

Figure 6.10: Variation in the jet velocity as the aspect ratio of the air bubble is varied, at $We = 60$ and $Oh = 0.013$. The x axis shows the aspect ratio of the air bubble width over height. The y axis shows the jet velocity non-dimensionalised by the initial impact velocity of the composite drop.

therefore a greater velocity. The second is that for larger aspect ratios the base of the bubble is initially closer to the surface. This occurs because in order to conserve liquid volume the radius of the liquid drop decreases slightly.

Three examples of collisions at different aspect ratios are shown in fig. 6.11. The top row shows the widest bubble considered which had an aspect ratio of 0.75, the middle and the bottom rows show the results at either end of the velocity plateau at aspects ratios of 1.1 and 1.25. The most obvious variation between the different simulations is in the width of the jet in the final image of each row. For the wide bubbles the jet is noticeably thicker from the beginning of its formation.

The bottom two rows of images have been included to shed some light on why the plateau forms for high aspect ratios. They show that the width of the jet begins increasing again in this region leading to the stagnation in the velocity. This thickening however does not occur at the moment of the jet's formation but later as the jet is able to pick up liquid from the wings on either side of the air bubble because the bubble is so narrow.

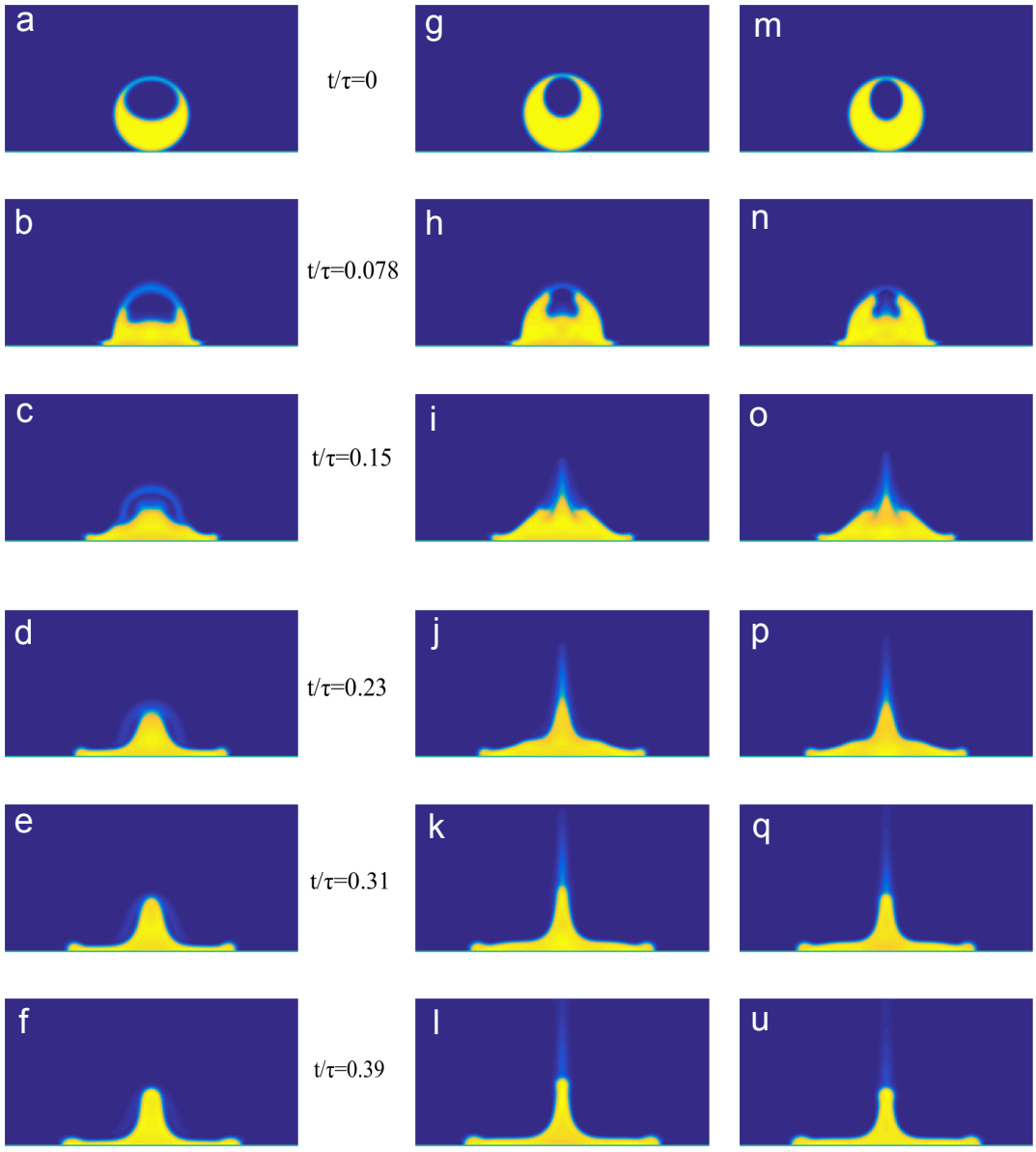

Figure 6.11: A comparison of three different impacts as the aspect ratio of an ellipsoidal air bubble is varied, at We=60 and Oh=0.013. The three columns are for aspect ratios of 0.75, 1.1 and 1.25 from left to right.

6.3 Discussion

A supposedly simple impact of a liquid drop containing an air bubble is studied. This leads to a jet leaving the drop after a time substantially less than the time taken for a drop of the same size to bounce from the surface, and with a significantly increased velocity. When trying to categorise the parameter space in which this system exists, however, it emerges that there are numerous parameters which can be varied which might have a substantial impact on both the qualitative and quantitative aspects of the jet formation. Some of these can be varied independently of the others and therefore have easily measurable effects. As the Weber number is increased by varying the impact velocity it leads to a linear increase in the jet ejection velocity at all but the lowest impact velocities. Varying the distance between the top of the liquid drop and the bubble has a very large retarding effect on the jet velocity and the jet formation quickly breaks down for bubbles which are not right at the top of the drop. This case however will never be reached by experiments as the air bubble will always be at the top of the drop due to gravity.

There are several other factors, for example the distance between the bottom of the drop and the bottom of the bubble, the curvature at the bottom of the bubble and the curvature at the bottom of the drop which it is hard to vary independently in the simulations. For example varying the size of the air bubble whilst keeping the liquid volume constant varies the curvature of the bottom of the bubble and the distance between the bottom of the bubble and the solid surface as well.

Antkowiak et al.(99; 58) looked at the effect of a variable which measured the radius of a bubble trapped at the surface compared to the radius of the cylinder in which the liquid is contained. In this work they found that smaller bubbles led to a faster maximal jet speed, most likely due to the increase in bubble curvature. In our case however we see that, as the bubble size is decreased, the jet velocity also decreases. This discrepancy is likely to be due to an important difference between our geometry and that considered by Antkowiak et al.. In our case the pressure wave formed on impact in the absence of a bubble is not planar, but instead has

a concave upwards shape due to the contact between the bottom surface of the drop and the substrate. Another difference is that the high pressure region caused by the impact of the drop also has another outlet as it forces the drop to spread outwards; a circumstance which is not possible when the liquid is constrained by solid walls. This leads to the distance between the bubble and the solid surface being an important factor, as by the time the pressure wave reaches the top of the drop it has lost much of its energy.

The effect of varying the width of the bubble supports these conclusions, as in this case the distance between the bubble and the surface is kept roughly constant whilst the width of the air bubble is varied. These simulations produce the expected result that as the bubble gets narrower and the curvature increases the jet velocity goes up. Overall the conclusion can be drawn that the greater the distance from the bottom of the bubble to the surface the lower the velocity and, independently of this, the greater the curvature of the bubble the greater the jet velocity.

More work needs to be done however to confirm this hypothesis. As we suspect that the lack of horizontal confinement the drop experiences leads to the pressure fall-off a set of simulations or experiments looking at the bouncing of such drops within holes of varying size may be useful with the expected result being that greater confinement would lead to a greater ejection velocity. Alternatively studying the pressure output from the simulations in more detail during a typical collision may be of use.

It is also worth briefly discussing some of the differences seen between the simulations and experiments. The big difference between the simulation and experimental results lies in the behaviour of the top interface of the bubble. Whilst this interface exists initially it breaks before the jet reaches it. This discrepancy is most likely because the diffuse interface in the simulations cannot maintain such a thin interface as that seen in the experiments. However an advantage of using simulations to study this jet formation as well as experiments is that the simulations can vary several parameters such as the drop size and placement much more easily.

The phenomena studied is the simplest example of the impact of systems

comprising drops and bubbles. There is the potential to look at many more set-ups of increasing complexity, for example varying the drop position horizontally, the number of drops or the shape of the surface upon which the impact takes place.

CHAPTER 7

Discussion

In this thesis several examples droplet of impact are investigated. With the exception of the last chapter they are tied together by the common theme of surface asymmetry. The last chapter looks at the impact of a drop which contains an air bubble. All these cases show bouncing phenomena which vary considerably from the well known collision on a flat surface.

We first considered the impact of drops upon large cylindrically shaped structures. The key point of these structures was that they broke the axisymmetric nature of the impact. In an impact upon a flat surface there is nothing to break the axial symmetry of the drop leading to a fully extended drop which is circular in shape. In the impacts upon cylinders, however, the fully extended drop was elliptical in shape when viewed from above. The elliptical shape then leads to a retraction step in which one axis shrinks more quickly so that the drop lifts off in an elongated shape. This process can be well explained by a rim film model in which the retraction force depends on the shape of the central film.

This may be of interest in the context of contact time reduction, and hence enhanced de-icing and drying. There are, however, several factors which could limit the applicability of these sorts of surfaces. The first and most obvious is that all drops are required to impact upon the cylindrical structure. A possible solution to this is a corrugated surface but this still has the issue that parts of the surface

are merely sloped flat surfaces rather than curves. Another point, which has not been discussed in detail, is that as the drop lifts off in an elongated shape less of the surface tension energy is converted in the rebound leading to a slower upwards velocity.

In chapter 4 the parameter space associated with the impacts on cylindrical surfaces is explored more thoroughly. As the size of the cylinder is reduced there is a crossover to the regime considered in the work by Bird *et al.*(45) where drop impact upon small ridges was studied. This regime could lead to a more reliable reduction in contact time, as covering a surface with numerous small ridges, could to a certain extent remove the effect that the point of impact has upon the bouncing. The simulations are also compared with the work of Guathier *et al.*(52) who looked more closely at the effect that changing the impact velocity has on the impact upon small ridges. In this work they found that, as the impact velocity was varied, the contact time varied in a step like fashion. This step like decrease was, however, not seen at the Weber numbers accessible to the simulations.

In chapters 3 and 4 we discussed the large effect of introducing asymmetry into a collision. To attempt to study the effect of asymmetry in more detail a simple model based on a Lagrangian approach was developed in chapter 5. The biggest drawback of the model is that it assumes that the drop shape can always be described as ellipsoidal, whereas we have previously shown that the drop often forms a rim-film system during the late stages of impact. This means that whilst the model can capture the effects due to the film shape, it does not currently take into account the fact that the majority of the mass during the retraction step is at the edge of the drop.

The model does none the less capture many of the important properties of an impact event. It exactly matches the Rayleigh approach for very small deformations but has the advantage that it can be extended beyond the linear limit. For simple symmetric impacts the contact time initially decreases with increase in impact speeds but soon reaches a constant value as the impact velocity is increased further.

Introducing a momentum asymmetry into the collision leads to a reduction in

contact time as expected. Because of the simplicity of the model the forces involved can be examined in detail and we find that the forces on the shorter axis are greater as predicted. Interestingly, however, the contact time reduction does not continue as the applied asymmetry is increased but instead begins to reach a plateau. This implies that there is a limit to how low the contact time can be pushed by the introduction of asymmetry.

The last chapter looks at something very different from the rest of the thesis. The impacts in this case are symmetric, and upon a flat surface. The point of interest is instead the composition of the drop itself. The inclusion of an air bubble is found to reliably lead to jet formation for fast enough impacts. The position of the air bubble within the drop is a variable of key interest. In experiments, however, the position of the drop cannot be easily controlled. The work on the impact of drops containing air bubbles is currently unfinished. More direct experimental comparisons are still needed as is a more in-depth look at how the pressure varies within the drop.

The work presented in this thesis serves to illustrate what a rich problem droplet impact is. Both the introduction of asymmetry and of embedded bubbles lead to interesting new phenomena. There are several avenues of future work which could be pursued. One is studying the effect of varying the contact angle on the surface in an asymmetric manner where some experimental results are already available(97). Another is improving the analytical model developed in chapter 5 to better take into account variations in the drop's shape. It would also be interesting to extend the lattice Boltzmann model to three phase coexistence or to look at droplet collisions.

References

Bibliography

[1] Worthington, A., 'On the forms assumed by drops of liquids falling vertically on a horizontal plate.' *Proceedings of the Royal Society of London*, **25**, 261, 1876.

[2] Mishchenko, L., Hatton, B., Bahadur, V. et al., 'Design of ice-free nanostructured surfaces based on repulsion of impacting water droplets.' *ACS Nano*, **4**, 7699, 2010.

[3] Singh, M., Haverinen, H.M., Dhagat, P. et al., 'Inkjet printing process and its applications.' *Advanced Materials*, **22**, 673, 2010.

[4] Matthews, G., 'Elestrostatic spraying of pesticides: A review.' *Crop Protection*, **8**, 3, 1989.

[5] Kim, J., 'Spray cooling heat transfer: the state of the art.' *International Journal of Heat and Fluid Flow*, **28**, 753, 2007.

[6] Park, K.C., Chhatre, S.S., Srinivasan, S. et al., 'Fog-harvesting mesh surfaces.' *Bulletin of the American Physical Society*, **57**, 2012.

[7] Yarin, A., 'Drop impact dynamics: splashing, spreading, receding, bouncing.' *Annual Review of Fluid Mechanics*, **38**, 159, 2006.

[8] Young, T., 'An essay on the cohesion of fluids.' *Philosophical Transactions of the Royal Society of London*, **95**, 65, 1805.

[9] Quéré, D., 'Rough ideas on wetting.' *Physica A: Statistical Mechanics and its Applications*, **313**, 32, 2002.

[10] Lafuma, A. and Quéré, D., 'Superhydrophobic states.' *Nature Materials*, **2**, 457, 2003.

[11] Hoorfar, M. and Neumann, A., 'Recent progress in axisymmetric drop shape analysis (adsa).' *Advances in Colloid and Interface Science*, **121**, 25, 2006.

[12] Shirtcliffe, N.J., McHale, G., Atherton, S. et al., 'An introduction to superhydrophobicity.' *Advances in Colloid and Interface Science*, **161**, 124, 2010.

[13] Reyssat, M., Richard, D., Clanet, C. et al., 'Dynamical superhydrophobicity.' *Faraday Discussions*, **146**, 19, 2010.

[14] Rothstein, J.P., 'Slip on superhydrophobic surfaces.' *Annual Review of Fluid Mechanics*, **42**, 89, 2010.

[15] Vinogradova, O.I., 'Slippage of water over hydrophobic surfaces.' *International Journal of Mineral Processing*, **56**, 31, 1999.

[16] Carlborg, C.F. and van der Wijngaart, W., 'Sustained superhydrophobic friction reduction at high liquid pressures and large flows.' *Langmuir*, **27**, 487, 2010.

[17] Barthlott, W. and Neinhuis, C., 'Purity of the sacred lotus, or escape from contamination in biological surfaces.' *Planta*, **202**, 1, 1997.

[18] Marmur, A., 'The lotus effect: superhydrophobicity and metastability.' *Langmuir*, **20**, 3517, 2004.

[19] Quéré, D. and Reyssat, M., 'Non-adhesive lotus and other hydrophobic materials.' *Philosophical Transactions of the Royal Society of London A: Mathematical, Physical and Engineering Sciences*, **366**, 1539, 2008.

[20] Zhai, L., Berg, M.C., Cebeci, F.C. et al., 'Patterned superhydrophobic surfaces: toward a synthetic mimic of the namib desert beetle.' *Nano Letters*, **6**, 1213, 2006.

[21] Cassie, A. and Baxter, S., 'Wettability of porous surfaces.' *Transactions of the Faraday Society*, **40**, 546, 1944.

[22] Wenzel, R.N., 'Resistance of solid surfaces to wetting by water.' *Industrial & Engineering Chemistry*, **28**, 988, 1936.

[23] Ishino, C., Okumura, K., and Quéré, D., 'Wetting transitions on rough surfaces.' *Europhysics Letters*, **68**, 419, 2004.

[24] Patankar, N.A., 'Transition between superhydrophobic states on rough surfaces.' *Langmuir*, **20**, 7097, 2004.

[25] Blow, M., Kusumaatmaja, H., and Yeomans, J., 'Imbibition through an array of triangular? posts.' *Journal of Physics: Condensed Matter*, **21**, 464125, 2009.

[26] Timonen, J. et al., 'Impalement transitions in droplets impacting microstructured superhydrophobic surfaces.' *Europhysics Letters*, **83**, 64002, 2008.

[27] Lee, C., Nam, Y., Lastakowski, H. et al., 'Two types of cassie-to-wenzel wetting transitions on superhydrophobic surfaces during drop impact.' *Soft Matter*, **11**, 4592, 2015.

[28] Bartolo, D., Bouamrirene, F., Verneuil, É. et al., 'Bouncing or sticky droplets: Impalement transitions on superhydrophobic micropatterned surfaces.' *Europhysics Letters*, **74**, 299, 2006.

[29] Liu, B. and Lange, F.F., 'Pressure induced transition between superhydrophobic states: configuration diagrams and effect of surface feature size.' *Journal of Colloid and Interface Science*, **298**, 899, 2006.

[30] Jung, Y.C. and Bhushan, B., 'Dynamic effects induced transition of droplets on biomimetic superhydrophobic surfaces.' *Langmuir*, **25**, 9208, 2009.

[31] Bormashenko, E., Pogreb, R., Whyman, G. et al., 'Vibration-induced cassie-wenzel wetting transition on rough surfaces.' *Applied Physics Letters*, **90**, 201917, 2007.

[32] McHale, G., Aqil, S., Shirtcliffe, N. et al., 'Analysis of droplet evaporation on a superhydrophobic surface.' *Langmuir*, **21**, 11053, 2005.

[33] McHale, G., Shirtcliffe, N., and Newton, M., 'Contact-angle hysteresis on super-hydrophobic surfaces.' *Langmuir*, **20**, 10146, 2004.

[34] Quéré, D., 'Surface chemistry: Fakir droplets.' *Nature materials*, **1**, 14, 2002.

[35] Gibbs, J.W., 'On the equilibrium of heterogeneous substances.' *American Journal of Science*, **96**, 441, 1878.

[36] Rioboo, R., Marengo, M., and Tropea, C., 'Time evolution of liquid drop impact onto solid, dry surfaces.' *Experiments in Fluids*, **33**, 112, 2002.

[37] Eggers, J., Fontelos, M.A., Josserand, C. et al., 'Drop dynamics after impact on a solid wall: theory and simulations.' *Physics of Fluids*, **22**, 062101, 2010.

[38] Bartolo, D., Josserand, C., and Bonn, D., 'Retraction dynamics of aqueous drops upon impact on non-wetting surfaces.' *Journal of Fluid Mechanics*, **545**, 329, 2005.

[39] Taylor, G., 'The dynamics of thin sheets of fluid. iii. disintegration of fluid sheets.' In Proceedings of the Royal Society of London A: Mathematical, Physical and Engineering Sciences, vol. 253, 313–321, The Royal Society, 1959.

[40] Culick, F., 'Comments on a ruptured soap film.' *Journal of applied physics*, **31**, 1128, 1960.

[41] Jung, S., Dorrestijn, M., Raps, D. et al., 'Are superhydrophobic surfaces best for icephobicity?' *Langmuir*, **27**, 3059, 2011.

[42] Savage, N., 'Synthetic coatings: Super surfaces.' *Nature*, **519**, S7, 2015.

[43] Gilet, T. and Bourouiba, L., 'Rain-induced ejection of pathogens from leaves: revisiting the hypothesis of splash-on-film using high-speed visualization.' *Integrative and Comparative Biology*, **54**, 974, 2014.

[44] Richard, D., Clanet, C., and Quéré, D., 'Surface phenomena: Contact time of a bouncing drop.' *Nature*, **417**, 811, 2002.

[45] Bird, J.C., Dhiman, R., Kwon, H.M. et al., 'Reducing the contact time of a bouncing drop.' *Nature*, **503**, 385, 2013.

[46] Liu, Y., Andrew, M., Li, J. et al., 'Symmetry breaking in drop bouncing on curved surfaces.' *Nature Communications*, **6**, 10034, 2015.

[47] Khojasteh, D., Kazerooni, N.M., Salarian, S. et al., 'Droplet impact on superhydrophobic surfaces: A review of recent developments.' *Journal of Industrial and Engineering Chemistry*, **42**, 1, 2016.

[48] Kwon, D.H. and Lee, S.J., 'Impact and wetting behaviors of impinging microdroplets on superhydrophobic textured surfaces.' *Applied Physics Letters*,

100, 171601, 2012.

[49] Chen, L., Xiao, Z., Chan, P.C. et al., 'A comparative study of droplet impact dynamics on a dual-scaled superhydrophobic surface and lotus leaf.' *Applied Surface Science*, **257**, 8857, 2011.

[50] Wang, Z., Lopez, C., Hirsa, A. et al., 'Impact dynamics and rebound of water droplets on superhydrophobic carbon nanotube arrays.' *Applied Physics Letters*, **91**, 023105, 2007.

[51] Jung, Y.C. and Bhushan, B., 'Dynamic effects of bouncing water droplets on superhydrophobic surfaces.' *Langmuir*, **24**, 6262, 2008.

[52] Gauthier, A., Symon, S., Clanet, C. et al., 'Water impacting on superhydrophobic macrotextures.' *Nature Communications*, **6**, 8001, 2015.

[53] Robson, S. and Willmott, G.R., 'Asymmetries in the spread of drops impacting on hydrophobic micropillar arrays.' *Soft Matter*, **12**, 4853, 2016.

[54] de Ruiter, J., Lagraauw, R., van den Ende, D. et al., 'Wettability-independent bouncing on flat surfaces mediated by thin air films.' *Nature Physics*, **11**, 48, 2015.

[55] Eggers, J. and Villermaux, E., 'Physics of liquid jets.' *Reports on Progress in Physics*, **71**, 036601, 2008.

[56] Rayleigh, L., 'On the capillary phenomena of jets.' *Proceedings of the Royal Society of London*, **29**, 71, 1879.

[57] Castrejón-Pita, A.A., Castrejon-Pita, J., and Hutchings, I., 'Breakup of liquid filaments.' *Physical review letters*, **108**, 074506, 2012.

[58] Antkowiak, A., Bremond, N., Duplat, J.M. et al., 'Cavity jets.' *Physics of Fluids*, **19**, 91112, 2007.

[59] Tagawa, Y., Oudalov, N., Visser, C.W. et al., 'Highly focused supersonic microjets.' *Physical Review X*, **2**, 031002, 2012.

[60] Peters, I.R., Tagawa, Y., Oudalov, N. et al., 'Highly focused supersonic microjets: numerical simulations.' *Journal of Fluid Mechanics*, **719**, 587, 2013.

[61] Castrejón-Pita, A., Castrejón-Pita, J., and Martin, G., 'A novel method to

produce small droplets from large nozzles.' *Review of scientific instruments*, **83**, 115105, 2012.

[62] Duchemin, L., Popinet, S., Josserand, C. et al., 'Jet formation in bubbles bursting at a free surface.' *Physics of Fluids*, **14**, 3000, 2002.

[63] Séon, T. and Antkowiak, A., 'Large bubble rupture sparks fast liquid jet.' *Physical Review Letters*, **109**, 014501, 2012.

[64] Ghabache, É., Séon, T., and Antkowiak, A., 'Liquid jet eruption from hollow relaxation.' *Journal of Fluid Mechanics*, **761**, 206, 2014.

[65] Lee, T. and Liu, L., 'Lattice boltzmann simulations of micron-scale drop impact on dry surfaces.' *Journal of Computational Physics*, **229**, 8045, 2010.

[66] Connington, K. and Lee, T., 'Lattice boltzmann simulations of forced wetting transitions of drops on superhydrophobic surfaces.' *Journal of Computational Physics*, **250**, 601, 2013.

[67] Chen, S. and Doolen, G.D., 'Lattice boltzmann method for fluid flows.' *Annual Review of Fluid Mechanics*, **30**, 329, 1998.

[68] Swift, M.R., Osborn, W., and Yeomans, J., 'Lattice boltzmann simulation of nonideal fluids.' *Physical Review Letters*, **75**, 830, 1995.

[69] Yeomans, J., 'Mesoscale simulations: Lattice boltzmann and particle algorithms.' *Physica A: Statistical Mechanics and its Applications*, **369**, 159, 2006.

[70] Huang, K., Statistical Mechanics. Wiley, 1987.

[71] Capuani, F., Pagonabarraga, I., and Frenkel, D., 'Discrete solution of the electrokinetic equations.' *The Journal of Chemical Physics*, **121**, 973, 2004.

[72] Liu, L. and Lee, T., 'Wall free energy based polynomial boundary conditions for non-ideal gas lattice boltzmann equation.' *International Journal of Modern Physics C*, **20**, 1749, 2009.

[73] He, X. and Luo, L.S., 'A priori derivation of the lattice boltzmann equation.' *Physical Review E*, **55**, 6333, 1997.

[74] Liu, Y., Moevius, L., Xu, X. et al., 'Pancake bouncing on superhydrophobic surfaces.' *Nature Physics*, **10**, 515, 2014.

[75] Liu, Y., Whyman, G., Bormashenko, E. et al., 'Controlling drop bouncing using surfaces with gradient features.' *Applied Physics Letters*, **107**, 051604, 2015.

[76] Moevius, L., Liu, Y., Wang, Z. et al., 'Pancake bouncing: simulations and theory and experimental verification.' *Langmuir*, **30**, 13021, 2014.

[77] Chu, K.H., Xiao, R., and Wang, E.N., 'Uni-directional liquid spreading on asymmetric nanostructured surfaces.' *Nature Materials*, **9**, 413, 2010.

[78] Daniel, S., Chaudhury, M.K., and Chen, J.C., 'Fast drop movements resulting from the phase change on a gradient surface.' *Science*, **291**, 633, 2001.

[79] Malvadkar, N.A., Hancock, M.J., Sekeroglu, K. et al., 'An engineered anisotropic nanofilm with unidirectional wetting properties.' *Nature Materials*, **9**, 1023, 2010.

[80] Liu, C., Ju, J., Zheng, Y. et al., 'Asymmetric ratchet effect for directional transport of fog drops on static and dynamic butterfly wings.' *ACS Nano*, **8**, 1321, 2014.

[81] Malouin Jr, B.A., Koratkar, N.A., Hirsa, A.H. et al., 'Directed rebounding of droplets by microscale surface roughness gradients.' *Applied Physics Letters*, **96**, 234103, 2010.

[82] Bird, J.C., Tsai, S.S., and Stone, H.A., 'Inclined to splash: triggering and inhibiting a splash with tangential velocity.' *New Journal of Physics*, **11**, 063017, 2009.

[83] Chen, R. and Wang, H., 'Effects of tangential speed on low-normal-speed liquid drop impact on a non-wettable solid surface.' *Experiments in Fluids*, **39**, 754, 2005.

[84] Zhang, K., Liu, F., Williams, A.J. et al., 'Self-propelled droplet removal from hydrophobic fiber-based coalescers.' *Physical Review Letters*, **115**, 074502, 2015.

[85] Deng, T., Varanasi, K.K., Hsu, M. et al., 'Nonwetting of impinging droplets on textured surfaces.' *Applied Physics Letters*, **94**, 133109, 2009.

[86] Bhushan, B. and Jung, Y.C., 'Wetting, adhesion and friction of superhy-

drophobic and hydrophilic leaves and fabricated micro/nanopatterned surfaces.' *Journal of Physics: Condensed Matter*, **20**, 225010, 2008.

[87] Kolinski, J., Mahadevan, L., and Rubinstein, S., 'Drops can bounce from perfectly hydrophilic surfaces.' *Europhysics Letters*, **108**, 24001, 2014.

[88] Hejazi, V., Sobolev, K., and Nosonovsky, M., 'From superhydrophobicity to icephobicity: forces and interaction analysis.' *Scientific Reports*, **3**, 2194, 2013.

[89] Kinnell, P., 'Raindrop-impact-induced erosion processes and prediction: a review.' *Hydrological Processes*, **19**, 2815, 2005.

[90] Josserand, C. and Thoroddsen, S.T., 'Drop impact on solid surface.' *Annual Review of Fluid Mechanics*, **48**, 365, 2016.

[91] Marengo, M., Antonini, C., Roisman, I.V. et al., 'Drop collisions with simple and complex surfaces.' *Current Opinion in Colloid and Interface Science*, **16**, 292, 2011.

[92] Chen, L., Wu, J., Li, Z. et al., 'Evolution of entrapped air under bouncing droplets on viscoelastic surfaces.' *Colloids and Surfaces A: Physicochemical and Engineering Aspects*, **384**, 726, 2011.

[93] Quéré, D., 'Leidenfrost dynamics.' *Annual Review of Fluid Mechanics*, **45**, 197, 2013.

[94] Biance, A.L., Pirat, C., and Ybert, C., 'Drop fragmentation due to hole formation during leidenfrost impact.' *Physics of Fluids*, **23**, 022104, 2011.

[95] E.M.Lishitz, L.D.L., Course of Theoretical Physics: Fluid Mechanics. Pergamon Press, 1959.

[96] Courty, S., Lagubeau, G., and Tixier, T., 'Oscillating droplets by decomposition on the spherical harmonics basis.' *Physical Review E*, **73**, 045301, 2006.

[97] Song, D., Song, B., Hu, H. et al., 'Selectively splitting a droplet using superhydrophobic stripes on hydrophilic surfaces.' *Physical Chemistry Chemical Physics*, **17**, 13800, 2015.

[98] Michon, G., Surface Area of an Ellipsoid. www.numericana.com.

[99] Antkowiak, A., Bremond, N., Le Dizes, S. et al., 'Short-term dynamics of a

density interface following an impact.' *Journal of Fluid Mechanics*, **577**, 241, 2007.

[100] Bowden, F.P. and McOnie, M.P., 'Cavities and micro munro jets in liquids: Their role in explosion.' *Nature*, **206**, 380, 1965.

[101] Dear, J.P., Field, J.E., and Walton, A.J., 'Gas compression and jet formation in cavities collapsed by a shock wave.' *Nature*, **332**, 505, 1988.